STATE OF THE CLIMATE IN 2022

GLOBAL OCEANS

G. C. Johnson and R. Lumpkin, Eds.

Special Online Supplement to the *Bulletin of the American Meteorological Society* Vol. 104, No. 9, September, 2023

https://doi.org/10.1175/BAMS-D-23-0076.2

Corresponding author: Greg C. Johnson / Gregory.C.Johnson@noaa.gov

STATE OF THE CLIMATE IN 2022
Global Oceans

Editors

Ellen Bartow-Gillies
Jessica Blunden
Tim Boyer

Chapter Editors

Peter Bissolli
Kyle R. Clem
Howard J. Diamond
Matthew L. Druckenmiller
Robert J. H. Dunn
Catherine Ganter
Nadine Gobron
Gregory C. Johnson
Rick Lumpkin
Ademe Mekonnen
John B. Miller
Twila A. Moon
Marilyn N. Raphael
Ahira Sánchez-Lugo
Carl J. Schreck III
Richard L. Thoman
Kate M. Willett
Zhiwei Zhu

Technical Editor

Lukas Noguchi

BAMS Special Editor for Climate

Michael A. Alexander

American Meteorological Society

Cover Credit:
Surf's Up by Gregory C. Johnson. Livestock Marker on Oil Paper

How to cite this document:
Global Oceans is one chapter from the *State of the Climate in 2022* annual report and is available from https://doi.org/10.1175/BAMS-D-23-0076.2. Compiled by NOAA's National Centers for Environmental Information, *State of the Climate in 2022* is based on contributions from scientists from around the world. It provides a detailed update on global climate indicators, notable weather events, and other data collected by environmental monitoring stations and instruments located on land, water, ice, and in space. The full report is available from https://doi.org/10.1175/2023BAMSStateoftheClimate.1.

Citing the complete report:
Blunden, J., T. Boyer, and E. Bartow-Gillies, Eds., 2023: "State of the Climate in 2022". Bull. Amer. Meteor. Soc., 104 (9), Si–S501 https://doi.org/10.1175/2023BAMSStateoftheClimate.1.

Citing this chapter:
Johnson, G. C. and R. Lumpkin, Eds., 2023: Global Oceans [in "State of the Climate in 2022"]. Bull. Amer. Meteor. Soc., 104 (9), S146–S206, https://doi.org/10.1175/BAMS-D-23-0076.2.

Citing a section (example):
Thompson, P. R., M. J. Widlansky, E. Leuliette, D. P. Chambers, W. Sweet, B. D. Hamlington, S. Jevrejeva, M. A. Merrifield, G. T. Mitchum, and R. S. Nerem, 2023: Sea-level variability and change [in "State of the Climate in 2022"]. Bull. Amer. Meteor. Soc., 104 (9), S173–S176, https://doi.org/10.1175/BAMS-D-23-0076.2.

Editor and Author Affiliations (alphabetical by name)

Atkinson, C., Met Office Hadley Center, Exeter, United Kingdom

Biló, Tiago, Cooperative Institute for Marine and Atmospheric Studies, University of Miami, Miami, Florida; NOAA/OAR Atlantic Oceanographic and Meteorological Laboratory, Miami, Florida

Boyer, Tim, NOAA/NESDIS National Centers for Environmental Information, Silver Spring, Maryland

Bringas, Francis, NOAA/OAR Atlantic Oceanographic and Meteorological Laboratory, Miami, Florida

Carter, Brendan R., Cooperative Institute for Climate, Ocean, and Ecosystem Studies, University of Washington, Seattle, Washington; NOAA/OAR Pacific Marine Environmental Laboratory, Seattle, Washington

Cetinić, Ivona, NASA Goddard Space Flight Center, Greenbelt, Maryland; Morgan State University, Baltimore, Maryland

Chambers, Don P., College of Marine Science, University of South Florida, St. Petersburg, Florida

Chan, Duo, Woods Hole Oceanographic Institution, Woods Hole, Massachusetts

Cheng, Lijing, International Center for Climate and Environment Sciences, Institute of Atmospheric Physics, Chinese Academy of Sciences, Beijing, China

Chomiak, Leah, Cooperative Institute for Marine and Atmospheric Studies, University of Miami; NOAA/OAR Atlantic Oceanographic and Meteorological Laboratory, Miami, Florida; Rosenstiel School of Marine, Atmospheric, and Earth Science, University of Miami, Miami, Florida

Cronin, Meghan F., NOAA/OAR Pacific Marine Environmental Laboratory, Seattle, Washington

Dong, Shenfu, NOAA/OAR Atlantic Oceanographic and Meteorological Laboratory, Miami, Florida

Feely, Richard A., NOAA/OAR Pacific Marine Environmental Laboratory, Seattle, Washington

Franz, Bryan A., NASA Goddard Space Flight Center, Greenbelt, Maryland

Gao, Meng, NASA Goddard Space Flight Center, Greenbelt, Maryland; Science Systems and Applications Inc., Lanham, Maryland

Garg, Jay, Science Systems and Applications Inc., Hampton, Virginia

Gilson, John, Scripps Institution of Oceanography, University of California San Diego, La Jolla, California

Goni, Gustavo, NOAA/OAR Atlantic Oceanographic and Meteorological Laboratory, Miami, Florida

Hamlington, Benjamin D., Center for Coastal Physical Oceanography, Old Dominion University, Norfolk, Virginia

Hobbs, W., Australian Antarctic Program Partnership, Institute for Marine and Antarctic Studies; Australian Research Council Centre of Excellence for Climate Extremes, University of Tasmania, Hobart, Tasmania

Hu, Zeng-Zhen, NOAA/NWS National Centers for Environmental Prediction Climate Prediction Center, College Park, Maryland

Huang, Boyin, NOAA/NESDIS National Centers for Environmental Information, Asheville, North Carolina

Ishii, Masayoshi, Department of Atmosphere, Ocean and Earth System Modeling Research, Meteorological Research Institute, Japan Meteorological Agency, Tsukuba, Japan

Jevrejeva, Svetlana, National Oceanography Centre, Liverpool, United Kingdom

Johns, W., Rosenstiel School of Marine, Atmospheric, and Earth Science, University of Miami, Miami, Florida

Johnson, Gregory C., NOAA/OAR Pacific Marine Environmental Laboratory, Seattle, Washington

Landschützer, Peter, Flanders Marine Institute, InnovOcean Campus, Ostend, Belgium

Lankhorst, Matthias, Scripps Institution of Oceanography, University of California San Diego, La Jolla, California

Leuliette, Eric, NOAA/NWS NCWCP Laboratory for Satellite Altimetry, College Park, Maryland

Locarnini, Ricardo, NOAA/NESDIS National Centers for Environmental Information, Silver Spring, Maryland

Lumpkin, Rick, NOAA/OAR Atlantic Oceanographic and Meteorological Laboratory, Miami, Florida

Lyman, John M., Cooperative Institute for Marine and Atmospheric Research, University of Hawaii, Honolulu, Hawaii; NOAA/OAR Pacific Marine Environmental Laboratory, Seattle, Washington

McPhaden, Michael J., NOAA/OAR Pacific Marine Environmental Laboratory, Seattle, Washington

Merrifield, Mark A., Cooperative Institute for Marine and Atmospheric Research, University of Hawaii, Honolulu, Hawaii

Mishonov, Alexey, Earth System Science Interdisciplinary Center/Cooperative Institute for Satellite Earth System Studies Maryland, University of Maryland, College Park, Maryland; NOAA/NESDIS National Centers for Environmental Information, Silver Spring, Maryland

Mitchum, Gary T., College of Marine Science, University of South Florida, St. Petersburg, Florida

Moat, Ben I., National Oceanography Centre, Southampton, United Kingdom

Mrekaj, Ivan, Technical University in Zvolen, Zvolen, Slovakia

Nerem, R. Steven, Colorado Center for Astrodynamics Research, Cooperative Institute for Research in Environmental Sciences, University of Colorado Boulder, Boulder, Colorado

Purkey, Sarah G., Scripps Institution of Oceanography, University of California San Diego, La Jolla, California

Qiu, Bo, Department of Oceanography, University of Hawaii at Manoa, Honolulu, Hawaii

Reagan, James, NOAA/NESDIS National Centers for Environmental Information, Silver Spring, Maryland

Sato, Katsunari, Japan Meteorological Agency, Tokyo, Japan

Schmid, Claudia, NOAA/OAR Atlantic Oceanographic and Meteorological Laboratory, Miami, Florida

Sharp, Jonathan D., Cooperative Institute for Climate, Ocean, and Ecosystem Studies, University of Washington, Seattle, Washington; NOAA/OAR Pacific Marine Environmental Laboratory, Seattle, Washington

Siegel, David A., University of California, Santa Barbara, Santa Barbara, California

Smeed, David A., National Oceanography Centre, Southampton, United Kingdom

Stackhouse Jr., Paul W., NASA Langley Research Center, Hampton, Virginia

Sweet, William, NOAA/NOS Center for Operational Oceanographic Products and Services, Silver Spring, Maryland

Thompson, Philip R., Cooperative Institute for Marine and Atmospheric Research, University of Hawaii, Honolulu, Hawaii

Triñanes, Joaquin A., Laboratory of Systems, Technological Research Institute, Universidad de Santiago de Compostela, Campus Universitario Sur, Santiago de Compostela, Spain; Cooperative Institute for Marine and Atmospheric Studies, Rosenstiel School of Marine and Atmospheric Science, University of Miami, Miami, Florida; NOAA/OAR Atlantic Oceanographic and Meteorological Laboratory, Miami, Florida

Volkov, Denis L., Cooperative Institute for Marine and Atmospheric Studies, University of Miami; NOAA/OAR Atlantic Oceanographic and Meteorological Laboratory, Miami, Florida

Wanninkhof, Rik, NOAA/OAR Atlantic Oceanographic and Meteorological Laboratory, Miami, Florida

Wen, Caihong, NOAA/NWS National Centers for Environmental Prediction Climate Prediction Center, College Park, Maryland

Westberry, Toby K., Oregon State University, Corvallis, Oregon

Widlansky, Matthew J., Cooperative Institute for Marine and Atmospheric Research, University of Hawaii, Honolulu, Hawaii

Editor and Author Affiliations (continued)

Willis, J., Jet Propulsion Laboratory, California Institute of Technology, Pasadena, California

Xie, Ping-Ping, NOAA/NWS National Centers for Environmental Prediction Climate Prediction Center, College Park, Maryland

Yin, Xungang, NOAA/NESDIS National Centers for Environmental Information, Asheville, North Carolina

Zhang, Huai-min, NOAA/NESDIS National Centers for Environmental Information, Asheville, North Carolina

Zhang, Li, NOAA/NWS National Centers for Environmental Prediction Climate Prediction Center, College Park, Maryland; ERT, Laurel, Maryland

Editorial and Production Team

Allen, Jessicca, Graphics Support, Cooperative Institute for Satellite Earth System Studies, North Carolina State University, Asheville, North Carolina

Camper, Amy V., Graphics Support, Innovative Consulting and Management Services, LLC, NOAA/NESDIS National Centers for Environmental Information, Asheville, North Carolina

Haley, Bridgette O., Graphics Support, NOAA/NESDIS National Centers for Environmental Information, Asheville, North Carolina

Hammer, Gregory, Content Team Lead, Communications and Outreach, NOAA/NESDIS National Centers for Environmental Information, Asheville, North Carolina

Love-Brotak, S. Elizabeth, Lead Graphics Production, NOAA/NESDIS National Centers for Environmental Information, Asheville, North Carolina

Ohlmann, Laura, Technical Editor, Innovative Consulting and Management Services, LLC, NOAA/NESDIS National Centers for Environmental Information, Asheville, North Carolina

Noguchi, Lukas, Technical Editor, Innovative Consulting and Management Services, LLC, NOAA/NESDIS National Centers for Environmental Information, Asheville, North Carolina

Riddle, Deborah B., Graphics Support, NOAA/NESDIS National Centers for Environmental Information, Asheville, North Carolina

Veasey, Sara W., Visual Communications Team Lead, Communications and Outreach, NOAA/NESDIS National Centers for Environmental Information, Asheville, North Carolina

3. Table of Contents

Please refer to Chapter 8 (Relevant Datasets and Sources) for a list of all climate variables and datasets used in this chapter for analyses, along with their websites for more information and access to the data.

3. GLOBAL OCEANS

G. C. Johnson and R. Lumpkin, Eds.

a. Overview

—G. C. Johnson and R. Lumpkin

An unusual "triple-dip" La Niña, described in Sidebar 3.1, had continuing, wide-spread ramifications for the state of ocean and climate in 2022. Triple-dip La Niñas are not unprecedented, but until now have always followed an extreme El Niño. Anomalously low sea-surface temperatures (SSTs) in the eastern tropical Pacific persisted from August 2020 through December 2022, with only a brief intermission in May–July 2021. Strengthened easterly trade winds drove anomalously strong westward surface currents and brought cold waters to the surface in the eastern equatorial Pacific while also accumulating anomalously salty and warm waters in the western equatorial Pacific, raising sea level there. These cold upwelled waters resulted in anomalously large fluxes of carbon dioxide from the ocean to the atmosphere and heat from the atmosphere to the ocean, with anomalously high chlorophyll concentrations found around its edges. Fresh sea-surface salinity (SSS) anomalies strengthened off the equator in the Pacific as the Intertropical Convergence Zone (ITCZ) and South Pacific Convergence Zone and associated rainfall shifted poleward.

A negative phase of the Pacific Decadal Oscillation continued in 2022, with warm SST and high ocean heat content values in the center of the North Pacific basin, and colder and lower values around the edges. However, the North Pacific marginal seas, except the eastern Bering Sea, were anomalously warm. A persistent 2020–22 poleward shift in the Kuroshio extension was evident in both ocean heat content and zonal surface current anomalies.

The Indian Ocean dipole (IOD) was negative in 2022, with positive SST anomalies in the east and negative anomalies in the west. As expected with a negative IOD, upper-ocean heat content and sea-surface height were anomalously high in the east and lower (although still above the climatological means) in the west. With warm water in the east came an eastward shift in precipitation, yielding anomalously low SSS there and anomalously high SSS in the west.

In the Atlantic, SST, upper-ocean heat content, and sea level were all above average over much of the basin in 2022, with especially high values off the east coast of North America. The only location with both cold SST and low ocean heat content anomalies was southeast of Greenland, potentially a fingerprint of slowing meridional overturning circulation. Sea-surface salinity values were anomalously high in salty regions and anomalously low around the ITCZ, off the Amazon, and in the subpolar North Atlantic. All of this was similar to 2021 conditions in that basin.

As discussed in Sidebar 3.1, continued La Niña conditions through 2022 kept global annual average SST anomalies below record-high territory, but the last decade of SST is higher than any other in the observation period. In addition, from 2021 to 2022, annual average ocean heat content from 0 to 2000 dbar increased at a rate equivalent to ~1.1 W m^{-2} of energy applied over the ocean surface, and global sea level increased by ~3.3 mm. Both set new record highs. In haiku form:

Surface cooling from,
triple-dip La Niña but,
seas rise, absorb heat.

In addition, the oceans absorbed anthropogenic carbon at a rate of ~3.3 Pg C yr^{-1} in 2022, 23% above the 1990–2020 average. The continued ocean uptake of heat and carbon dioxide delay and reduce atmospheric warming, respectively, but at the cost of sea-level rise, ocean warming and marine heatwaves, ocean acidification, and reduced ocean-dissolved oxygen concentrations, as discussed in Sidebar 3.2.

b. Sea-surface temperatures

—X. Yin, B. Huang, Z.-Z. Hu, D. Chan, and H.-M. Zhang

Sea-surface temperature (SST) changes and their uncertainties in 2022 are assessed over the global and individual ocean basins using three updated SST products: Extended Reconstruction SST version 5 (ERSSTv5; Huang et al. 2017, 2020), U.K. Met Office Hadley Centre SST (HadSST.4.0.1.0; Kennedy et al. 2019), and Daily Optimum Interpolation SST (DOISST v2.1; Huang et al. 2021a). SST anomalies (SSTAs) are calculated relative to their 1991–2020 baseline period climatologies. The magnitudes of SSTAs are compared against SST standard deviations (SD) over 1991–2020.

The year ended with the third La Niña winter in a row (see Sidebar 3.1). This prolonged La Niña resulted in a slowdown in the global ocean warming trend during 2020–22. Specifically, the 2022 global mean ERSSTv5 SSTA relative to a 1991–2020 baseline was 0.18±0.01°C, slightly higher than that of 2021 (0.14±0.01°C), but lower than those of 2019 (0.25±0.02°C) and 2020 (0.23±0.01°C), the years prior to and at the beginning of the triple-dip La Niña. Despite the influence of La Niña, 2022 still ranked as the sixth-hottest year on record since 1854 in terms of global-mean SST, equal with 2018. Here, uncertainty, reported as 95% confidence intervals, is estimated by a Student's t-test using a 500-member ERSSTv5 ensemble with randomly drawn parameter values within reasonable ranges during SST reconstructions (Huang et al. 2015, 2020).

Annually averaged SSTAs in 2022 (Fig. 3.1a) exhibited a pattern typical of La Niña in the Pacific. In the central and eastern tropical Pacific, SSTAs were mostly lower than –0.5°C and between –1.0°C and –1.5°C along the equator, extending from South America westward to the central Pacific. In the South Pacific, east of 170°W between 65°S and 45°S, SSTAs were between –0.2°C and –1.0°C. Between the two colder-than-normal regions and in the western Pacific, SSTs were mostly above normal by over 0.5°C. Except for the areas along the western North American coast, the North Pacific was dominated by positive SSTAs, particularly over the northwest region between 30°N and 50°N, where high SSTAs were observed between +1.0°C and +2.0°C. The Atlantic Ocean was marked by positive SSTAs of between +0.2°C and +1.0°C in the North Atlantic and between +0.2°C and +0.5°C in the tropical and South Atlantic. In the tropical Indian Ocean, an Indian Ocean dipole (IOD; Saji et al. 1999) was formed with SSTAs between –0.2°C and –0.5°C in the west and between +0.2°C and +0.5°C in the east (see section 4f for details). The IOD index has been negative since May 2021 and was the strongest (–1.2°C in July 2022) since the 1920s. SSTAs above +0.5°C were observed in parts of the Arctic Ocean, particularly in the Barents Sea.

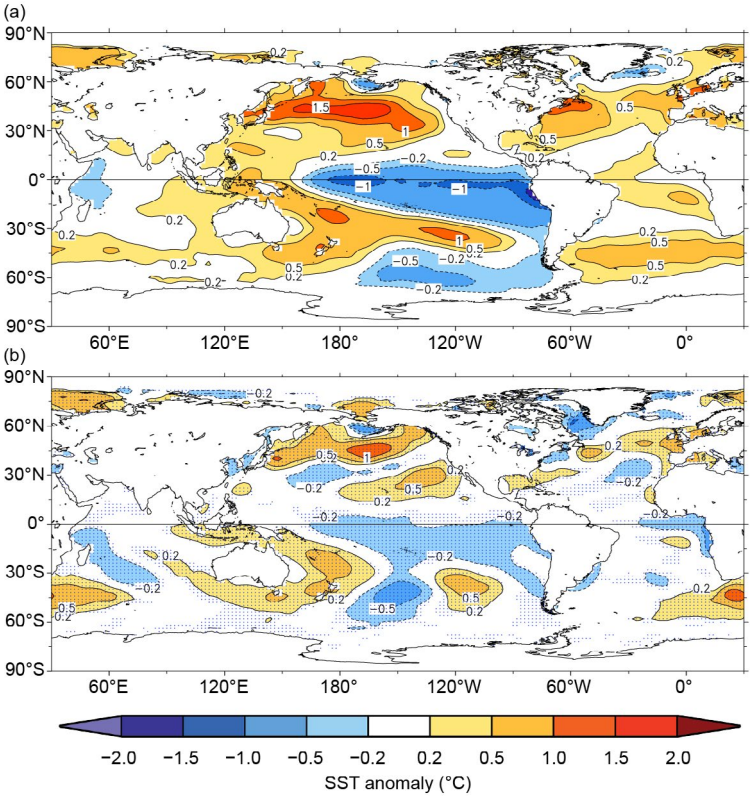

Fig. 3.1. (a) Annually averaged sea-surface temperature anomalies (SSTAs) in 2022 (°C) and (b) difference of annually averaged SSTAs from the previous year (2022 minus 2021; °C). Values are relative to 1991–2020 climatology and the SSTA difference is significant at 95% confidence in stippled areas.

The 2022-minus-2021 SSTAs show mixed localized patterns of increases and decreases (Fig. 3.1b). The lower cold-tongue SSTs and higher SSTs in the western Pacific around Australia indicate the strengthening of La Niña in 2022. Except for the western Pacific between 20°N and 40°N and in the Bering Sea, the North Pacific was mostly warmer in 2022 than 2021. The pronounced warming in the central and western North Pacific, more than +1.5°C around 45°N and 165°W, is consistent with a persistent negative phase of the Pacific Decadal Oscillation (Mantua and Hare 2002). In the Indian Ocean, there was no obvious SST change north of the equator (<0.2°C). Areas north and south of Australia and southeast of southern Africa showed warming of between +0.2°C and +1.0°C. Cooling of up to −0.5°C was seen in the area from the middle of the tropical southern Indian Ocean northwestward across Madagascar to the coast of equatorial East Africa. As a result, a negative IOD event lasting from May to October was observed in 2022.

Overall patterns of seasonal mean SSTAs (Fig. 3.2) are similar to the annual mean pattern (Fig. 3.1) due to the sustained La Niña event. The negative SSTAs in the central-eastern tropical Pacific persisted (–1.0°C to –1.5°C; 1 to 2 SDs below average) in all seasons, particularly in December–February (DJF) and September–November (SON). In the North Pacific, positive SSTAs were first seen in the central-western region across 45°N in DJF and continued getting stronger while expanding rapidly with nearly full coverage of the North Pacific during June–August (JJA) and SON. In the Indian Ocean, the negative IOD pattern peaked in JJA. The seasonal variability of SSTAs in the North Atlantic Ocean was high, with negative anomalies in the subarctic surrounding Greenland during March–May (MAM), but became overall positive during SON, with a center in the western midlatitude North Atlantic Ocean. The midlatitude Atlantic Ocean was warmer than normal throughout the year, with SSTAs largest during SON 2022 in the North Atlantic and DJF 2021/22 in the South Atlantic. SSTAs in the tropical Atlantic were only weakly

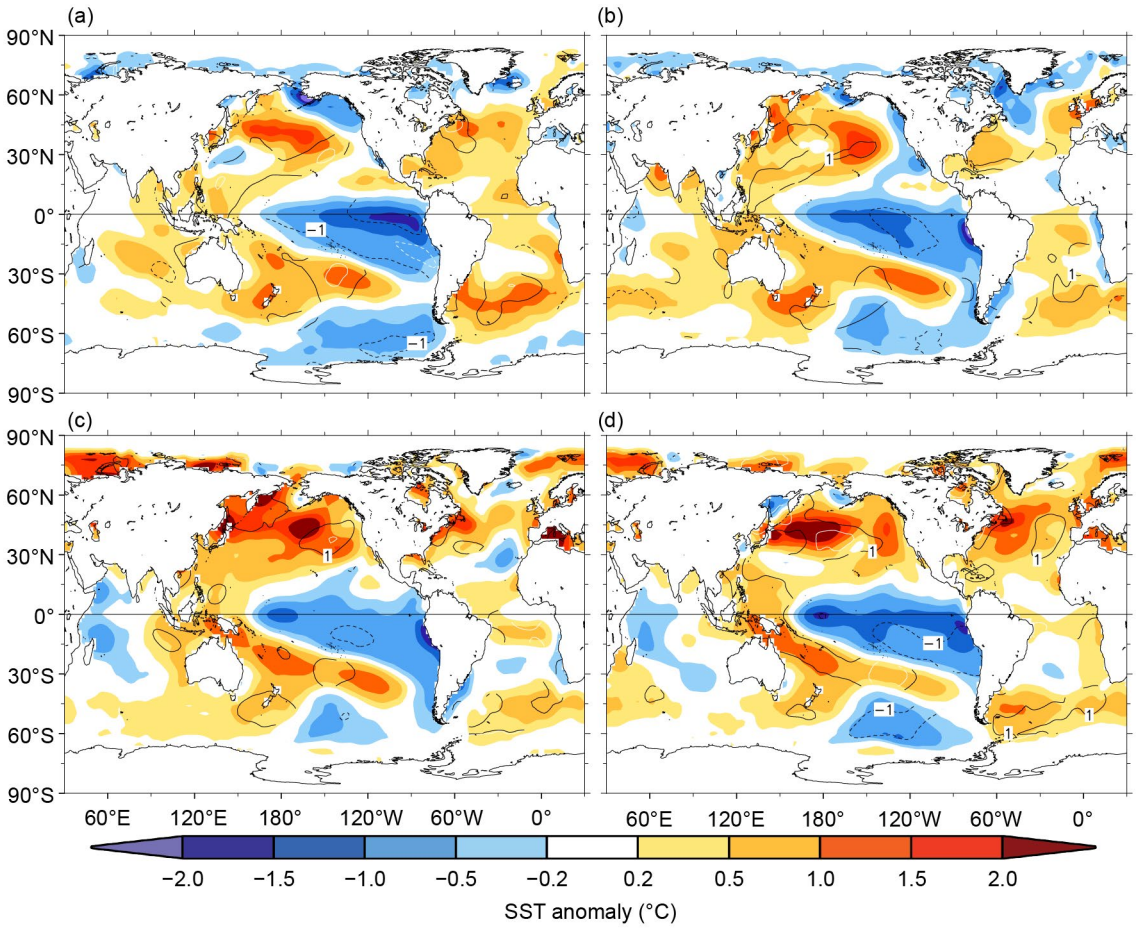

Fig. 3.2. Seasonally averaged sea-surface temperature anomalies (SSTAs) of ERSSTv5 (°C; shading) for (a) Dec 2021–Feb 2022, (b) Mar–May 2022, (c) Jun–Aug 2022, and (d) Sep–Nov 2022. The normalized seasonal mean SSTAs based on the seasonal mean standard deviation (1 SD) over 1991–2020 are indicated by contours of –2 (dashed white), –1 (dashed black), 1 (solid black), and 2 (solid white).

positive, and the Atlantic Niño index (ATL3; Zebiak 1993), which was greater than 0.5°C during May–December 2021, was below 0.5°C except in January and March 2022. SSTAs in the Arctic Ocean were slightly negative (−0.5°C to −0.2°C) in DJF and MAM but mostly positive (+0.5°C to +2.0°C) in JJA and SON.

In 2022, large positive SSTAs resulted in a series of marine heatwaves (Oliver et al. 2017; Perkins-Kirkpatrick et al. 2019; Babcock et al. 2019; Huang et al. 2021b) in various parts of the world. For example, in the Bay of Plenty, New Zealand, the country's longest continuous marine heatwave was recorded (Moana Project 2022; Figs. 3.2a,b). Also, in the summer of 2022, the Mediterranean Sea observed record-setting marine heatwave events, increasing from the previous summer in duration, total surface area impacted, and intensity as per the Mercator Ocean International organization (Fig. 3.2c; see section 2b4 for more details on marine heatwaves).

Global-mean SSTs manifest the acceleration in global warming (Figs. 3.3a,b), with 9 years in the last decade included in the top 10 hottest years on record. Based on ERSSTv5 (Table 3.1; Fig. 3.3), from 1950 to 2022, the linear trend in global-mean SSTA was 0.10±0.01°C decade^{-1}. Regionally, warming was largest in the tropical Indian Ocean (0.14±0.02°C decade^{-1}) and smallest in the North Pacific (0.09±0.04°C decade^{-1}). In recent decades, trends in all areas have increased, and in some areas substantially. From 2000 to 2022, the global mean trend was 0.15±0.06°C decade^{-1}. In the North Pacific, the regional 1950–2022 trend was the smallest but became the largest (0.40±0.12°C decade^{-1}) considering only the recent period from 2000 onward (Fig. 3.3d).

Large variations of North Atlantic annual mean SSTAs are evident at interannual to interdecadal time scales (Li et al. 2020; Fig. 3.3f). The interdecadal component is mainly associated with the Atlantic Multidecadal Variability (AMV; Schlesinger and Ramankutty 1994), also known as the Atlantic Multidecadal Oscillation. Some possible contributors to the AMV include aerosol emissions and variations in the strength of the Atlantic meridional overturning circulation (AMOC; Zhang et al. 2019; Wang and Yang 2017; section 3h). The North Atlantic experienced warm periods from the 1930s to the 1950s and from the late 1990s to the 2010s, and cold periods before 1930 and from the 1960s to the early 1990s (Li et al. 2020). SSTAs in the North Pacific (Fig. 3.3d) decreased from the 1960s to the late 1980s, followed by an increase from the later 1980s to the 2010s.

Table 3.1. Linear trends (°C decade^{-1}) of annually and regionally averaged sea-surface temperature anomalies (SSTAs) from ERSSTv5, HadSST4.0.1.0, and DOISST. The uncertainties at a 95% confidence level are estimated while accounting for the effective degrees of freedom (sampling number) quantified using lag-1 autocorrelation of annual-mean SST time series.

Product	Region	2000–22	1950–2022
HadSST.4.0.1.0	Global	0.17±0.06	0.12±0.02
DOISST	Global	0.19±0.05	N/A
ERSSTv5	Global	0.15±0.06	0.10±0.01
ERSSTv5	Tropical Pacific (30°S–30°N)	0.11±0.16	0.10±0.02
ERSSTv5	North Pacific (30°N–60°N)	0.40±0.12	0.09±0.04
ERSSTv5	Tropical Indian (30°S–30°N)	0.17±0.08	0.14±0.02
ERSSTv5	North Atlantic (30°N–60°N)	0.18±0.09	0.12±0.04
ERSSTv5	Tropical Atlantic (30°S–30°N)	0.14±0.08	0.11±0.02
ERSSTv5	southern oceans (30°S–60°S)	0.13±0.05	0.10±0.02

ERSSTv5 was compared with HadSST.4.0.1.0 and DOISST v2.1. SSTA departures of DOISST and HadSST.4.0.1.0 from ERSSTv5 are largely within 2 SDs (gray shading in Fig. 3.3) except in the 1960s–1970s and before the 1910s. The 2-SD was derived from a 500-member ensemble analysis based on ERSSTv5 (Huang et al. 2020) and centered on SSTAs of ERSSTv5. During both the longer and shorter trend periods (Table 3.1), the warming trend of global SST in HadSST4.0.1.0 was consistent with those of ERSSTv5 but at a higher rate. In the 2000s–2010s, SSTAs were slightly higher in DOISST than in ERSSTv5 in the Southern Ocean, tropical Atlantic, tropical Indian Ocean, and tropical Pacific. As a result, SST trends were slightly larger in DOISST over 2000–22 than in ERSSTv5.

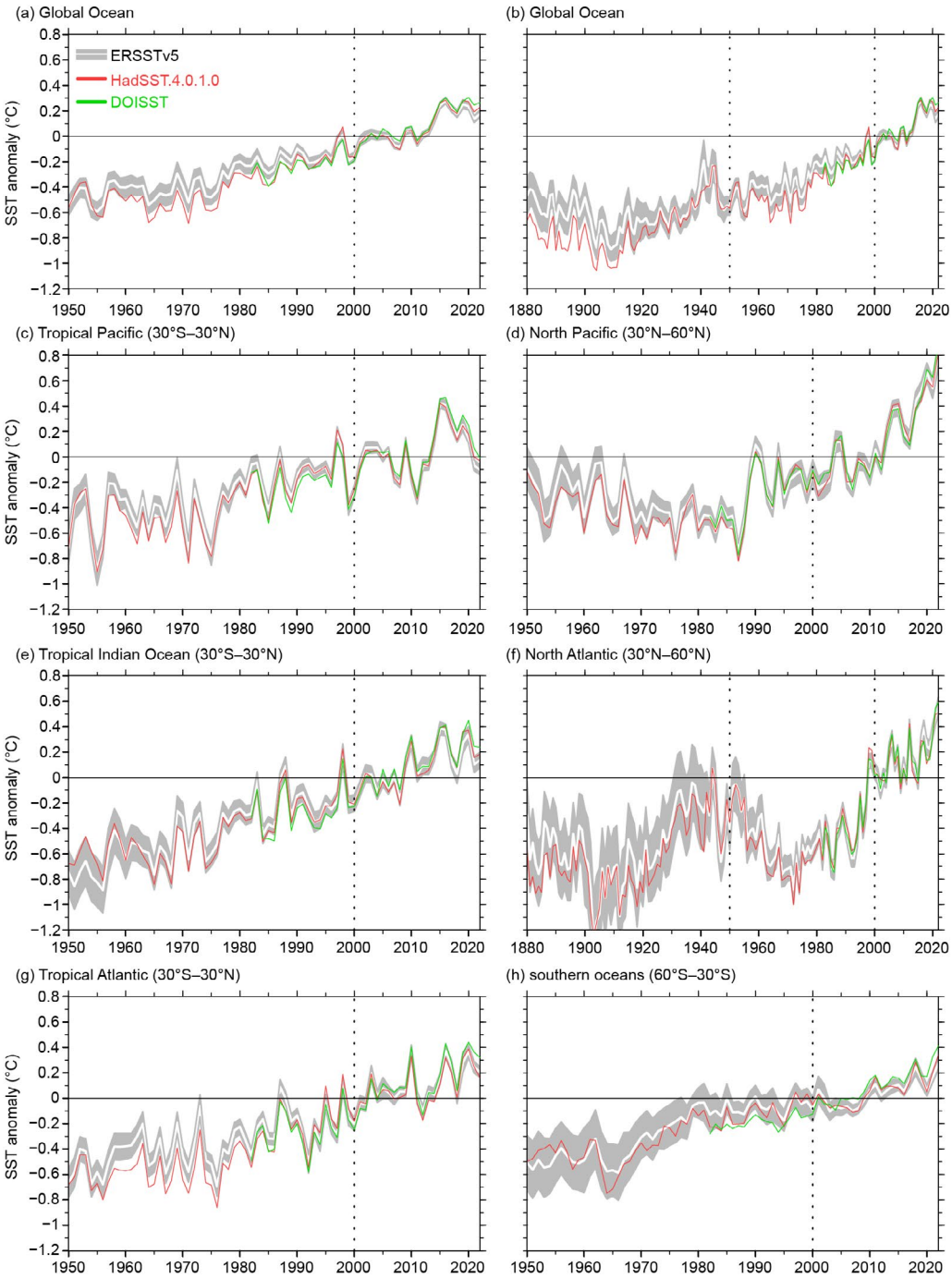

Fig. 3.3. Annually averaged sea-surface temperature anomalies (SSTAs; °C) of ERSSTv5, (solid white) and 2 standard deviations (SDs, gray shading) of ERSSTv5, SSTAs of HadSST.4.0.1.0 (solid red), and SSTAs of DOISST (solid green) in 1950–2022 except for (b) and (f). (a) Global, (b) global in 1880–2022, (c) tropical Pacific, (d) North Pacific, (e) tropical Indian, (f) North Atlantic in 1880–2022, (g) tropical Atlantic, and (h) southern oceans (30°S–60°S). The 2-SD envelope was derived from a 500-member ensemble analysis based on ERSSTv5 and centered to SSTAs of ERSSTv5. The years 2000 and 1950 are indicated by dotted vertical black lines.

Sidebar 3.1: The 2020–22 triple-dip La Niña

—M. J. MCPHADEN

The tropical Pacific experienced a third successive year of unusually cold sea-surface temperatures (SSTs) in 2022, making 2020–22 the first "triple-dip" La Niña of the twenty-first century (Fig. SB3.1a). Three-year La Niña events are rare but not unprecedented; similar events occurred in 1998–2001 and in 1973–76. Compared to single-year El Niño–Southern Oscillation (ENSO) events, such extended periods of anomalous SSTs in the tropical Pacific result in elevated risks from natural hazards because of the prolonged impacts these multi-year events have on patterns of weather variability world-wide. Back-to-back years of excessive rains in Australia, one of the most severe and extended droughts on record for the Horn of Africa, and exceptional drought in portions of the western United States during 2020–22 are just a few examples of how this multi-year La Niña affected the climate system. Moreover, these protracted La Niña conditions have occurred in the context of a warming world, so impacts have not only been felt over consecutive years but have also been compounded by human-caused climate change.

Below-normal SST anomalies first appeared in the eastern and central equatorial Pacific in August 2020 and, except for a brief period in May–July 2021, equatorial SSTs remained below the –0.5°C threshold considered to be an indicator of La Niña (Fig. SB3.1a). As illustrated for October–December 2022 (Figs. SB3.1b,c), associated with these below-normal SSTs is an intensified and westward-shifted Pacific Walker circulation characterized by stronger-than-normal surface trade winds (see Fig. 3.13a), unusually strong westerly winds in the upper troposphere, a westward shift in atmospheric deep convection, and a drying of the central equatorial Pacific. In addition, rain bands of both the Intertropical Convergence Zone in the Northern Hemisphere and the South Pacific Convergence Zone in the Southern Hemisphere were shifted poleward away from the unusually cold equatorial SSTs that favor suppressed convection. Heavy rains and flooding in Australia, Indonesia, and the Philippines and drought conditions in the island states of the central Pacific (see Fig. 3.12a) we direct consequences of these shifts in precipitation, prevalent not just in October–December 2022, but over much of the past three years. Anomalous atmospheric heating that accompanied this large-scale rearrangement in rainfall also drove far-field teleconnections to other parts of the globe (e.g., Taschetto et al. 2020), affecting many of the extreme weather events that were observed outside the tropical Pacific since late 2020.

A leading hypothesis for multi-year La Niñas is that they occur on the rebound from preceding strong El Niños (DiNezio et al. 2017) which, through recharge oscillator dynamics (Jin 1997), drain the equatorial band of upper-ocean heat content leaving a large heat deficit that takes multiple years to recover.

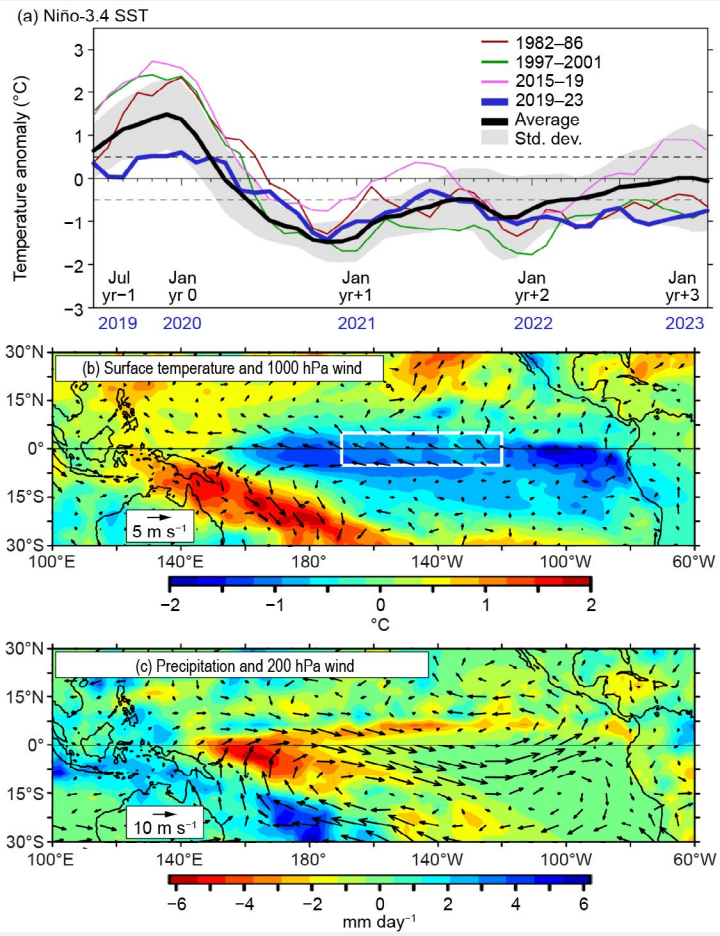

Fig. SB3.1. (a) Monthly mean sea-surface temperature (SST) anomalies from Jul 2019 to Jan 2023 (blue line) in the Niño-3.4 index region (5°S–5°N, 120°W–170°W). Also plotted is the monthly mean Niño-3.4 SST averaged over 10 La Niña events since the 1950s beginning in Jul the year before (Yr –1) the first SST minimum (in Yr 0), extending to the beginning of the third year (Yr +3) following the La Niña onset (black line). Shading indicates ±1 std. dev. The evolution of La Niña following the three strongest El Niños of the last 40 years, namely 1982/83, 1997/98, and 2015/16, is also shown. Dashed horizontal lines indicate the threshold for El Niño (> 0.5°C) and La Niña (< –0.5°C). Niño-3.4 SSTs are from ERSSTv5 (Huang et al. 2017). (b) Surface (1000 hPa) wind (m s^{-1}) and temperature (°C) anomalies for Oct–Dec 2022 with the Niño-3.4 region outlined in white. (c) Precipitation and upper level (200-hPa) wind anomalies for Oct–Dec 2022. Winds are from the NCEP/DOE Reanalysis (Kanamitsu et al. 2002), precipitation is from the Global Precipitation Climatology Project (Huffman et al. 2009), and surface air and sea temperatures are from HadISST (Rayner et al. 2003). All anomalies are relative to a 1991–2020 climatology.

The three strongest El Niños of the past 40 years illustrate this pattern (Fig. SB3.1a). The 1982/83 and 2015/16 El Niños were both followed by La Niñas extending over two years and the 1997/98 event was followed by three successive years of unusually cold tropical Pacific SSTs. Each of these El Niños was associated with a significant discharge of upper-ocean heat content from the equatorial band (McPhaden et al. 2021). However, the current multi-year La Niña does not conform to this scenario. Antecedent conditions in the tropical Pacific in 2019 were characterized by a borderline El Niño (Fig. SB3.1a) that did not lead to a large upper-ocean heat content discharge. What caused this latest three-year La Niña is thus a topic of considerable interest. One hypothesis is that the onset was triggered by a record positive Indian Ocean dipole in late 2019, then boosted in 2021 by unusually warm conditions in the tropical Atlantic involving the strongest Atlantic Niño since the 1970s (Hasan et al. 2022). Other possible explanations include influences from higher latitudes of the North Pacific (Park et al. 2021) or the impact of atmospheric aerosols from the 2019–20 Australian wildfires (Fasullo et al. 2023). Quantifying the relative contributions of these and other possible factors is a priority given the extraordinary socio-economics consequences of this multi-year La Niña.

Global mean surface air temperature (GMST) over the last eight years (2015–22) have been the warmest on record (see section 2b), attesting to the reality of climate change. However, the highest annual temperature in this record occurred in 2016 during a strong El Niño event rather than in 2022 (Fig. SB3.2), even though carbon dioxide concentrations in the atmosphere have risen over 2 parts per million per year during this time. The reason is that year-to-year variations in GMST are strongly influenced by the state of ENSO (Trenberth et al. 2002). During El Niño, unusually high SSTs in the tropical Pacific lead to increased evaporative cooling of the ocean. At the same time, increased cloudiness over the large expanse of usually warm water reduces the amount of sunlight entering the ocean, while cloud condensation in convective regions heats the atmosphere. During La Niña, the opposite happens. Thus, ENSO redistributes heat on a planetary scale, with an anomalously high heat flux from the ocean to the atmosphere during El Niño and an anomalously high heat flux from the atmosphere to the ocean during La Niña. For every 1°C of El Niño warming in the Niño-3.4 region, GMST rises by 0.073±0.024°C (with 95% confidence) with a delay of three months. A 1°C cooling in the Niño-3.4 region during La Niña results in a comparable drop in GMST (Fig. SB3.2). As a consequence, the predominance of unusually cold La Niña conditions since the end of the 2015/16 El Niño temporarily arrested the rise in GMST despite rising greenhouse gas concentrations.

The present situation is analogous to the previous hiatus in global warming in the first decade of the twenty-first century (Fig. SB3.2), which coincided with a period dominated by strong multi-year La Niñas (Fyfe et al. 2016; Hu and Fedorov 2017). That hiatus ended with the 2015/16 El Niño. The triple-dip La Niña dissipated in early 2023, and warm El Niño conditions will eventually return. When that happens, GMST will rise again with the likelihood of new record highs at some point in the near future.

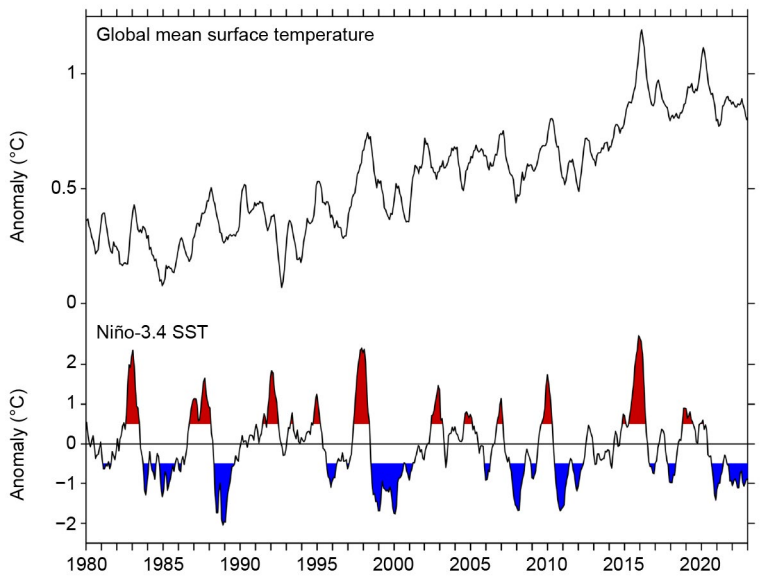

Fig. SB3.2. (top) Monthly averaged global mean surface temperature (GMST; °C) over 1980–2022 relative to the twentieth-century average. (bottom) Monthly sea-surface temperature (SST) anomalies (°C) in the Niño-3.4 region relative to a 1991–2020 climatology. El Niño periods are colored red and La Niña periods blue. Niño-3.4 SSTs are based on ERSSTv5 (Huang et al. 2017) and GMST is based on NOAA/NCEI global surface temperature anomalies (https://www.ncei.noaa.gov/access/monitoring/global-temperature-anomalies/anomalies). Dates shown along the x-axis are centered on tick marks, which are placed at the beginning of calendar years.

c. Ocean heat content

—G. C. Johnson, J. M. Lyman, C. Atkinson, T. Boyer, L. Cheng, J. Gilson, M. Ishii, R. Locarnini, A. Mishonov, S. G. Purkey, J. Reagan, and K. Sato

As a result of increasing atmospheric greenhouse gas concentrations, Earth's climate system has been absorbing more energy than it re-radiates back into space. The ocean stored ~91% of that excess energy from 1971 to 2018 (IPCC 2021). As seawater warms, it expands, and that expansion accounted for ~50% of the global average sea-level rise during that period (IPCC 2021). This warming is surface intensified, but can be seen down to the 2000-dbar sampling limit of core Argo (Wijffels et al. 2016), as well as in the coldest, densest ocean bottom waters that sink around Antarctica (Purkey and Johnson 2010). A warming ocean increases the atmosphere's temperature and capacity to carry moisture, affecting the frequency, intensity, perhaps duration, and rain amounts of atmospheric rivers (e.g., Payne et al. 2020) and cyclones (e.g., Walsh et al. 2016). Despite variations in ocean heat content from variations in ocean currents driven primarily by the wind, statistically significant regional warming trends are emerging over time (Johnson and Lyman 2020). Marine heatwaves have increased in intensity and duration as a result of these warming trends (Oliver et al. 2021). Ocean warming also increases undercutting of glaciers around Greenland (Wood et al. 2021) and melting around Antarctica (Schmidtko et al. 2014).

Maps of annual upper (0-m–700-m) ocean heat content anomaly (OHCA) relative to a 1993–2022 baseline mean (Fig. 3.4) were generated from a combination of in situ ocean temperature data and satellite altimetry data following Willis et al. (2004), but using Argo (Riser et al. 2016) data downloaded from an Argo Global Data Assembly Centre in January 2023 (http://doi.org/10.17882/42182#98916). Near-global average seasonal temperature anomalies versus pressure from Argo data (Roemmich and Gilson 2009, updated) since 2004 (Fig. 3.5) and in situ

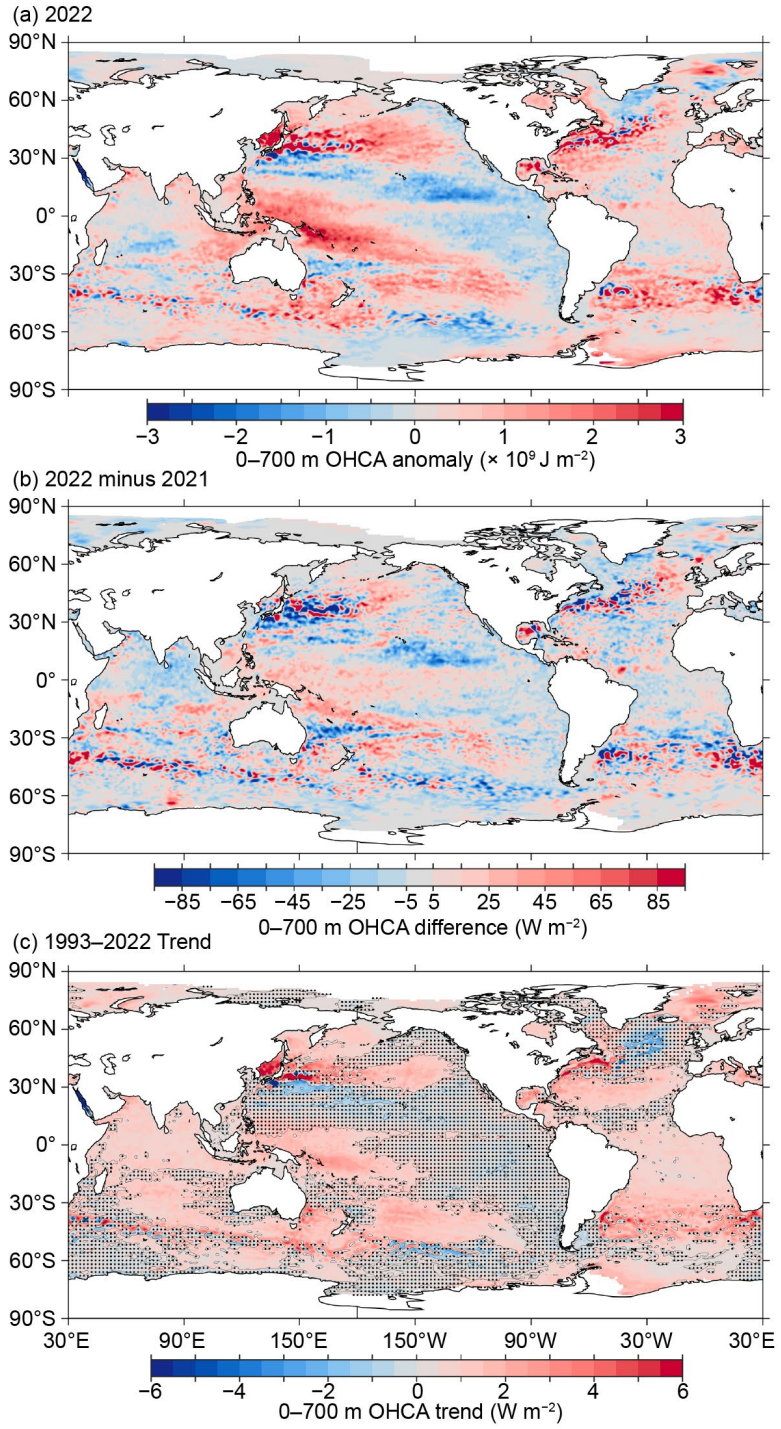

Fig. 3.4. (a) Combined satellite altimeter and in situ ocean temperature data estimate of upper (0 m–700 m) ocean heat content anomaly (OHCA; × 10^9 J m^{-2}) for 2022 analyzed following Willis et al. (2004) but using an Argo monthly climatology and displayed relative to the 1993–2022 baseline. (b) 2022-minus-2021 combined estimates of OHCA expressed as a local surface heat flux equivalent (W m^{-2}). For (a) and (b) comparisons, note that 95 W m^{-2} applied over one year results in a 3 × 10^9 J m^{-2} change of OHCA. (c) Linear trend from 1993 to 2022 of the combined estimates of upper (0 m–700 m) annual OHCA (W m^{-2}). Areas with statistically insignificant trends are stippled.

global estimates of OHCA for three pressure layers (0-m–700-m, 700-m–2000-m, and 2000-m–6000-m) from five different research groups (Fig. 3.6) are also discussed.

La Niña conditions were present for a third year in row, in a rare "triple-dip" event (see Sidebar 3.1 and section 4b for details). They resumed most recently in August 2021 and continued throughout 2022. However, the 2022-minus-2021 difference of upper OHCA (Fig. 3.4b) in the tropical Pacific shows an increase everywhere but in its northeast quadrant, in contrast with the 2021-minus-2020 and 2020-minus-2019 differences, both of which showed more increases in the western tropical Pacific and decreases in the central to eastern equatorial Pacific, more typical of La Niña years. As in the two previous years, 2022 upper-ocean heat content anomalies (Fig. 3.4a) in the equatorial Pacific were negative in the east and positive in the west, associated with anomalously westward currents on the equator (see Fig. 3.18a) driven by strong easterly trade winds (see Fig. 3.13a). Equatorward of the subtropical western boundary current extensions, 2022-minus-2021 differences exhibit zonally elongated low values in both hemispheres. The centers of the North and South Pacific were both anomalously warm in 2022, with colder conditions around the edges, consistent with a continued negative Pacific Decadal Oscillation index in the Northern Hemisphere (section 3b). The cold anomalies just south of the Kuroshio Extension and warm anomalies within that current are associated with a northward shift of that current (see Fig. 3.20), visible as a similarly zonally elongated anomaly dipole in surface current anomalies (see Fig. 3.18a). The Sea of Japan/East Sea, the Sea of Okhotsk, and the Bering Sea were all warmer than their long-term means in 2022.

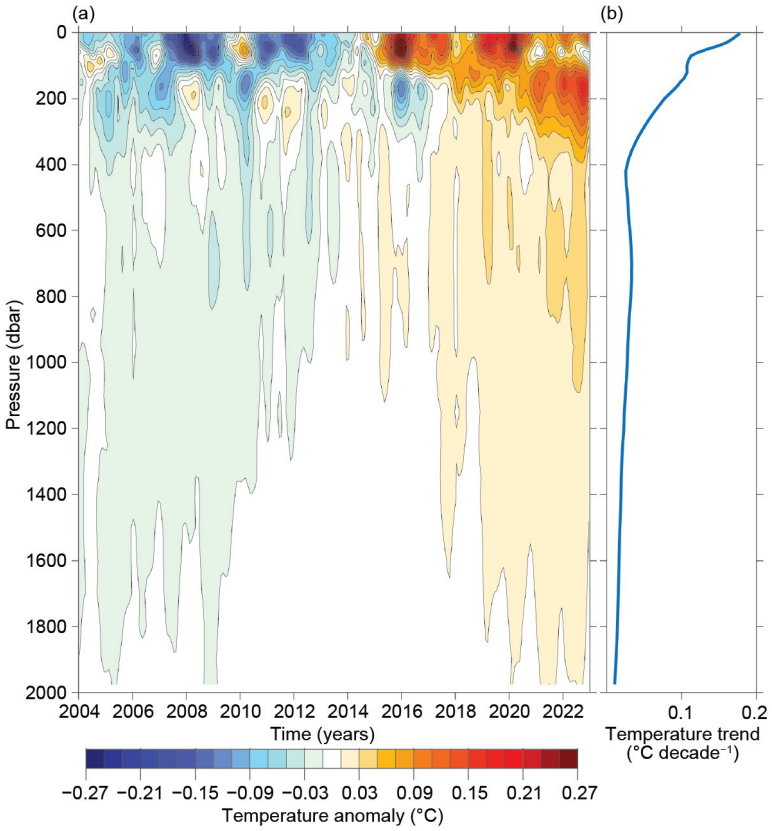

Fig. 3.5. (a) Near-global (65°S–80°N, excluding continental shelves, the Indonesian seas, and the Sea of Okhotsk) average monthly ocean temperature anomalies (°C; updated from Roemmich and Gilson [2009]) relative to record-length average monthly values, smoothed with a five-month Hanning filter and contoured at odd 0.02°C intervals (see color bar) vs. pressure and time. (b) Linear trend of temperature anomalies over time for the length of the record in (a) plotted vs. pressure in °C decade^{-1} (blue line).

In the Indian Ocean, the 2022-minus-2021 difference of upper OHCA (Fig. 3.4b) mostly decreased north of about 5°S and mostly increased south of that latitude. The 2022 OHCA anomalies (Fig. 3.4a) were negative in the center of the tropical South Indian Ocean and especially positive in the east between Australia and Indonesia. This pattern is broadly consistent with a negative phase of the Indian Ocean dipole index during 2022, with warm sea-surface temperature anomalies in the east Indian Ocean, and cold ones in the west (Fig. 3.1a).

The 2022-minus-2021 differences of upper OHCA (Fig. 3.4b) in the Atlantic Ocean were weakly negative in the Labrador Sea and the Irminger Sea, whereas much of the Gulf of Mexico exhibited an increase. Overall, the year-to-year differences in the Atlantic were small or not regionally coherent. Hence the broad pattern of upper OHCA in 2022 (Fig. 3.4a) is similar to that in 2021, with much of the Atlantic Ocean exhibiting upper OHCA above the 1993–2022 average (Fig. 3.4a) with the main exception, as in recent years, being cooler-than-average conditions southeast of Greenland. Anomalies were again especially high in the western North Atlantic and the subtropical South Atlantic in 2022.

As expected, the large-scale statistically significant regional patterns in the 1993–2022 local linear trends of upper OHCA (Fig. 3.4c) were similar to those from 1993 to 2021 (Johnson et al. 2022) and earlier reports. In general, the longer the period over which these trends are estimated, the more of the ocean surface area warms and the less of it cools at statistically significant rates (Johnson and Lyman 2020). In 2022 that tendency stands out in the Bering Sea and the northwest Pacific, where the coverage of statistically significant warming trends noticeably expanded relative to the 2021 results. Warming trends that were statistically significant occupied 55% of the global ocean surface area as of 2022, up from 49% for 1993–2021. Statistically significant cooling trends occupied only 2% of the ocean area, down from 3% for 1993–2021, most prominently southeast of Greenland.

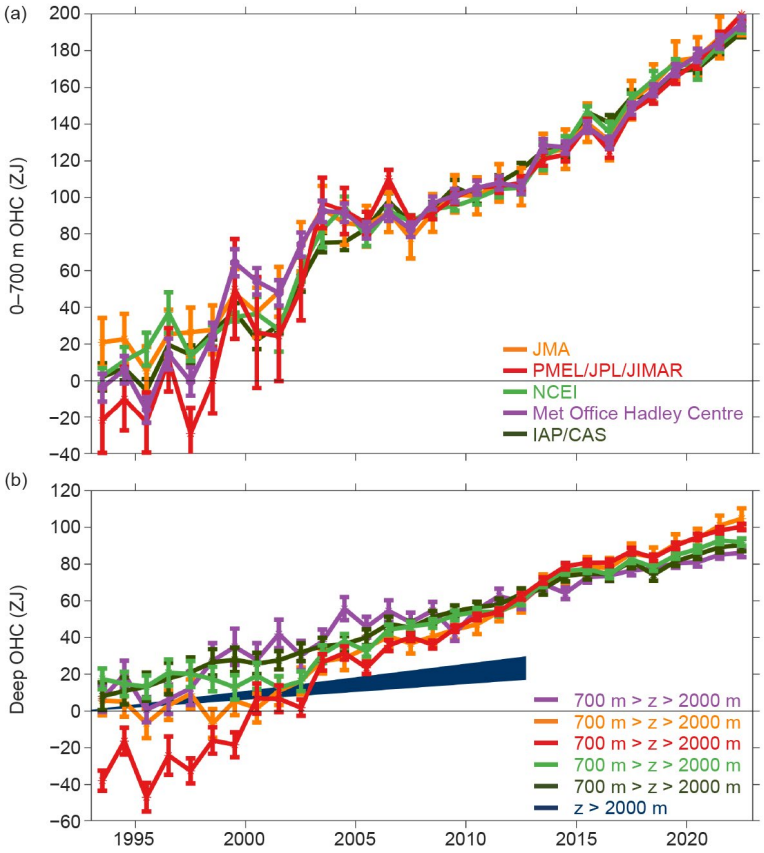

Fig. 3.6. (a) Annual average global integrals of in situ estimates of upper (0 m–700 m) ocean heat content anomaly (OHCA; ZJ; 1 ZJ = 10^{21} J) for 1993–2022 with standard errors of the mean. The MRI/JMA estimate is an update of Ishii et al. (2017). The PMEL/JPL/JIMAR estimate is an update and refinement of Lyman and Johnson (2014). The Met Office Hadley Centre estimate is computed from gridded monthly temperature anomalies following Palmer et al. (2007) and Good et al. (2013). Both the PMEL and Met Office estimates use Cheng et al. (2014) XBT corrections and Gouretski and Cheng (2020) MBT corrections. The NCEI estimate follows Levitus et al. (2012). The IAP/CAP estimate is reported in Cheng et al. (2023). See Johnson et al. (2014) for details on uncertainties, methods, and datasets. For comparison, all estimates have been individually offset (vertically on the plot), first to their individual 2005–22 means (the best sampled time period), and then to their collective 1993 mean. (b) Annual average global integrals of in situ estimates of intermediate (700 m–2000 m) OHCA for 1993–2022 (ZJ) with standard errors of the mean, and a long-term trend with one standard error uncertainty shown from Sep 1992 to Jan 2013 for deep and abyssal (z>2000 m) OHCA following Purkey and Johnson (2010) but updated using all repeat hydrographic section data available from https://cchdo.ucsd.edu/ as of Jan 2023.

Near-global average seasonal temperature anomalies (Fig. 3.5a) show the signature of La Niña (see Sidebar 3.1), which results in a reduction of warm anomalies from the surface to 100 dbar and an increase in warm anomalies from 100 dbar to 400 dbar and were most pronounced in the boreal winter. This pattern arises as strong easterly trade winds bring the cold waters below the equatorial thermocline to the surface in the eastern equatorial Pacific and create a large deep pool of warm waters in the western equatorial Pacific. A similar pattern can be seen in the 2007/08, 2010/11, and 2011/12 boreal winters. El Niño years (e.g., 2009/10, 2015/16, and 2018/19) have warmer near-surface and colder sub-surface waters, as expected given the deepening of the equatorial thermocline in the east, its shoaling in the west, and the spread of warm waters across much of the near-surface equatorial Pacific. Overlaid on this global signature of the El Niño–Southern Oscillation is an overall warming trend (Fig. 3.5b), strongest near the surface but evident all the way to the 2000-dbar sampling limit of Core Argo.

As noted in previous reports, the analysis is extended back in time from the Argo period to 1993 and expanded to examine greater depths, using sparser, more heterogeneous historical data collected mostly from ships (e.g., Abraham et al. 2013). Shallow expendable bathythermograph coverage may allow reasonable estimates of globally integrated OHCA in the upper 0-m–300-m or even 0-m–450-m back to the late 1960s, but it may be prudent to limit global 0-m–700-m estimates to the early 1990s and later (Lyman and Johnson 2014), as is done here.

The results for the 700-m–2000-m layer, which is quite sparsely sampled prior to the start of the Argo era (circa 2005–06), should be interpreted with caution before those years.

The different estimates of annual globally integrated upper OHCA (Fig. 3.6a) all reveal a large increase since 1993, with all of the five analyses reporting 2022 as a record high. Four out of five of the globally integrated 700-m–2000-m OHCA annual analyses (Fig. 3.6b) also report 2022 as a record high, and the long-term warming trend in this layer is also clear. The water column from 0 m to 700 m and 700 m to 2000 m gained 11.0 (±1.7) ZJ and 1.4 (±1.7) ZJ, respectively (means and standard deviations given) from 2021 to 2022. Causes of differences among estimates are discussed in Johnson et al. (2015).

The estimated linear rates of heat gain for each of the five global integral estimates of upper OHCA from 1993 through 2022 (Fig. 3.6a) range from 0.38 (±0.05) W m^{-2} to 0.44 (±0.10) W m^{-2} applied over the surface area of Earth (Table 3.2) rather than the surface area of the ocean, to better compare to the top-of-the-atmosphere energy imbalance (e.g., Loeb et al. 2021). These results are not much different from those in previous reports, although with an increasing record length, trend uncertainties tend to decrease and differences among analyses tend to diminish. Linear trends from the 700-m–2000-m layer over the same time period range from 0.17 (±0.03) W m^{-2} to 0.32 (±0.04) W m^{-2}. Trends in the upper 0-m–700-m layer all agree within their 5%–95% confidence intervals. However, as noted in previous reports, the trends in the 700-m–2000-m layer, which is quite sparsely sampled prior to the start of the Argo era, do not all overlap within their uncertainties. Different methods for dealing with under-sampled regions likely cause this disagreement. Using repeat hydrographic section data collected from 1981 through 2022 to update the estimate of Purkey and Johnson (2010) for 2000 m–6000 m, the linear trend is 0.07 (±0.03) W m^{-2} from September 1992 to January 2013 (these dates are global average times of first and last sampling of the sections). Summing the three layers (despite their slightly different time periods as given above), the full-depth ocean heat gain rate applied to Earth's entire surface ranges from 0.64 W m^{-2} to 0.83 W m^{-2}.

Table 3.2. Trends of ocean heat content increase (in W m^{-2} applied over the 5.1 × 10^{14} m^2 surface area of Earth) from six different research groups over three depth ranges (see Fig. 3.6 for details). For the upper (0 m–700 m) and intermediate (700 m–2000 m) depth ranges, estimates cover 1993–2022, with 5%–95% uncertainties based on the residuals taking their temporal correlation into account when estimating degrees of freedom (Von Storch and Zwiers 1999). The 2000 m–6000 m depth range estimate, an update of Purkey and Johnson (2010), uses data from 1981 to 2022, having a global average start and end date of Sep 1992 to Jan 2013, also with 5%–95% uncertainty.

Research Group	0 m–700 m Global ocean heat content trends (W m^{-2})	700 m–2000 m Global ocean heat content trends (W m^{-2})	2000 m–6000 m Global ocean heat content trends (W m^{-2})
MRI/JMA	0.38±0.05	0.24±0.04	—
PMEL/JPL/JIMAR	0.44±0.10	0.32±0.04	—
NCEI	0.39±0.05	0.19±0.04	—
Met Office Hadley Centre	0.40±0.07	0.17±0.03	—
IAP/CAS	0.41±0.03	0.18±0.01	—
Purkey and Johnson	—	—	0.07±0.03

d. Salinity

—G. C. Johnson, J. Reagan, J. M. Lyman, T. Boyer, C. Schmid, and R. Locarnini

1. INTRODUCTION

Variations in ocean salinity and temperature set the density of the ocean, and thus the vertical stratification which impacts the depth to which the ocean communicates directly with the atmosphere. Lateral density variations are linked to ocean currents via the thermal wind relation. At high latitudes, where temperatures are cold and often have a small range, salinity is often the dominant factor in setting the vertical density structure. Salinity variations, created by advection, precipitation/evaporation, river runoff, and ice melt or freezing (Ren et al. 2011; Yu 2011) can influence ocean–atmosphere exchanges of heat and dissolved gases (including influencing marine heatwaves, ocean carbon dioxide uptake, tropical cyclones, and deep or bottom water formation), the exchange of nutrients or oxygen between the surface mixed layer and denser waters below, and so on.

Global average practical salinity is about 34.7. Surface values are below 28.0 or above 37.4 for only 1% of the ocean surface area each. In general, regions where evaporation dominates (such as the subtropics) have higher salinity values and where precipitation is dominant (the Intertropical Convergence Zone [ITCZ] and high latitudes), it is fresher (e.g., Wüst 1936; Schmitt 1995). Multi-decadal trends in ocean salinity have been used to show increases in the hydrological cycle (e.g., Durack et al. 2012; Skliris et al. 2014; Skliris 2016). Springtime sea-surface salinity values in the subtropical North Atlantic Ocean have even shown skill in predicting summer-monsoon rainfall in the African Sahel (Li et al. 2016).

To investigate interannual changes of subsurface salinity, all available salinity profile data are quality controlled following Boyer et al. (2018) and then used to derive 1° monthly mean gridded salinity anomalies relative to a long-term monthly mean for the years 1955–2017 (World Ocean Atlas 2018; Zweng et al. 2018) at standard depths from the surface to 2000 m. In recent years, the largest source of salinity profiles is the profiling floats of the Argo program (Riser et al. 2016). These data are a mix of real-time (preliminary) and delayed-mode (scientific quality controlled) observations. Hence, the estimates presented here may be subject to instrument biases such as a positive salinity drift identified in a subset of Argo Conductivity-Temperature-Depth, and will change after all data are subjected to scientific quality control. The sea-surface salinity (SSS) analysis relies on Argo data downloaded in January 2023, with annual anomaly maps relative to a seasonal climatology generated following Johnson and Lyman (2012) as well as monthly maps of bulk (as opposed to skin) SSS data from the Blended Analysis of Surface Salinity (BASS; Xie et al. 2014). BASS blends in situ SSS data with data from the *Aquarius* (Le Vine et al. 2014; mission ended in June 2015), Soil Moisture and Ocean Salinity (SMOS; Font et al. 2013), and the Soil Moisture Active Passive (SMAP; Fore et al. 2016) satellite missions. Despite the larger uncertainties of satellite data relative to Argo data, their higher spatial and temporal sampling allows higher spatial and temporal resolution maps than are possible using in situ data alone at present. All salinity values used in this section are reported as observed, on the dimensionless Practical Salinity Scale-78 (Fofonoff and Lewis 1979).

2. SEA-SURFACE SALINITY

G. C. Johnson and J. M. Lyman

As noted in previous reports (e.g., Johnson et al. 2020), since salinity has no direct feedback to the atmosphere, large-scale SSS anomalies can be quite persistent. (In contrast, sea-surface temperature anomalies are often damped by air–sea heat exchange.) Salty anomalies along and just south of the equator in the western and central Pacific, respectively, strengthened in 2022 (Figs. 3.7ab), for the third consecutive year. This pattern, owing to anomalous westward surface currents advecting relatively salty water westward along with shifts in precipitation, has built up over the past three years during the triple-dip La Niña (Sidebar 3.1). The relatively fresh feature in the western South Pacific near 20°S also built in strength from 2021 to 2022, at least partially owing to a poleward shift in the South Pacific ITCZ with La Niña. In the North Pacific, the center

of the basin was mostly anomalously salty in 2022, and the periphery was generally anomalously fresh. South of 30°S, the Pacific was primarily salty in 2022.

SSS in the Atlantic freshened from 2021 to 2022 off most of the east coast of North, Central, and South America (Fig. 3.7b). As a result, in 2022, SSS was anomalously fresh around the Caribbean, possibly owing to a record flood of the Amazon River in 2021 (e.g., Espinoza et al. 2022), but remained anomalously salty off the east coast of North America from the Gulf of Mexico to Labrador. Other fresh regions in the Atlantic in 2022 include the Irminger Sea, the ITCZ, and portions of the Atlantic Southern Ocean sector. The regions around the subtropical salinity maximum were anomalously salty in both the North and South Atlantic, as for many other recent years.

Freshening in the southeastern tropical Indian Ocean and salinification in much of the north and west continued from 2021 to 2022 (Fig. 3.7b), as it did from 2020 to 2021, again consistent with a negative Indian Ocean dipole (IOD) index for much of 2022, associated with a drying in the west and increased precipitation in the east (see Figs. 3.12a,b), as discussed in last year's report. The ocean offshore of much of India was also anomalously fresh in 2022, with the western freshening persisting from 2021 and the eastern freshening building from 2021 (Figs. 3.7a,b).

As the atmosphere warms, it can hold more moisture, enabling an increased hydrological cycle over the ocean (Held and Soden 2006; Durack and Wijffels 2010). Since upper-ocean salinity values can function as a sort of evaporation pan and rain gauge wrapped into one, the expected pattern from this change is "salty gets saltier and fresh gets fresher," and has been evident in *State of the Climate* reports since 2006, the first year of the salinity section. In 2022 this pattern held (Fig. 3.7a), with salty SSS anomalies in at least a portion of all of the subtropical salinity maxima and fresh SSS anomalies in the subpolar North Pacific and part of the subpolar North Atlantic, as well as the ITCZs of the Pacific and Atlantic. The 2005–22 SSS trends (Fig. 3.7c) reflect this pattern to some extent as well, with statistically significant (unstippled areas) freshening trends evident in the eastern subpolar North Pacific and

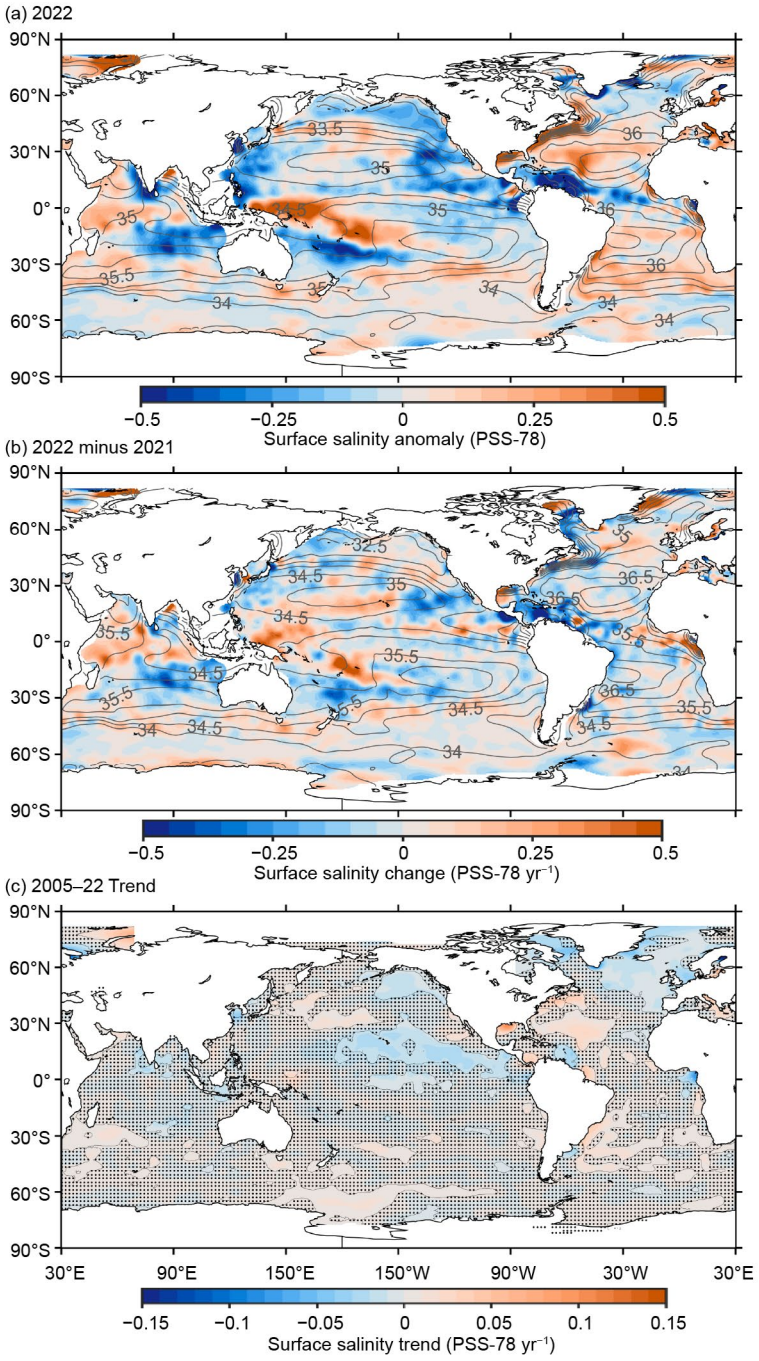

Fig. 3.7. (a) Map of the 2022 annual sea-surface salinity anomaly (colors, Practical Salinity Scale-78 [PSS-78]) with respect to monthly climatological 1955–2012 salinity fields from WOA13v2 (yearly average; gray contours at 0.5 intervals, PSS-78). (b) Difference of 2022 and 2021 sea-surface salinity maps (colors, PSS-78 yr^{-1}). White ocean areas are too data-poor (retaining <80% of a large-scale signal) to map. (c) Map of local linear trends estimated from annual sea-surface salinity anomalies for 2005–22 (colors, PSS-78 yr^{-1}). Areas with statistically insignificant trends at 5%–95% confidence are stippled. All maps are made using Argo data.

North Atlantic, the Pacific ITCZ, and the Gulf of Guinea, as well as statistically significant salty trends in parts of the subtropics in all basins.

In 2022, the seasonal BASS (Xie et al. 2014) SSS anomalies (Fig. 3.8) show the progressions of many of the features in the annual anomaly map using Argo data alone (Fig. 3.7a), and with higher spatial resolution, albeit with less accuracy. The anomalously fresh conditions in the Caribbean Seas build between December–February and March–May. The build-up of anomalously salty water in the western equatorial Pacific over the year is also clear in these maps, as is the development of the fresh anomaly discussed above just to the south of it. A zonally elongated anomalously salty band just south of an anomalously fresh band, with the transition at around 9°N, extends across much of the Pacific, and is especially apparent in September–November 2022. These are associated with a poleward shift of the ITCZ owing to the La Niña (see Sidebar 3.1 and Fig. 3.12a) and/or an intensified and northward-shifted North Equatorial Countercurrent indicated by eastward surface current anomalies of 8 cm s^{-1} to 10 cm s^{-1} at 6°N–8.5°N, 90W°–175°W (see Fig. 3.18a).

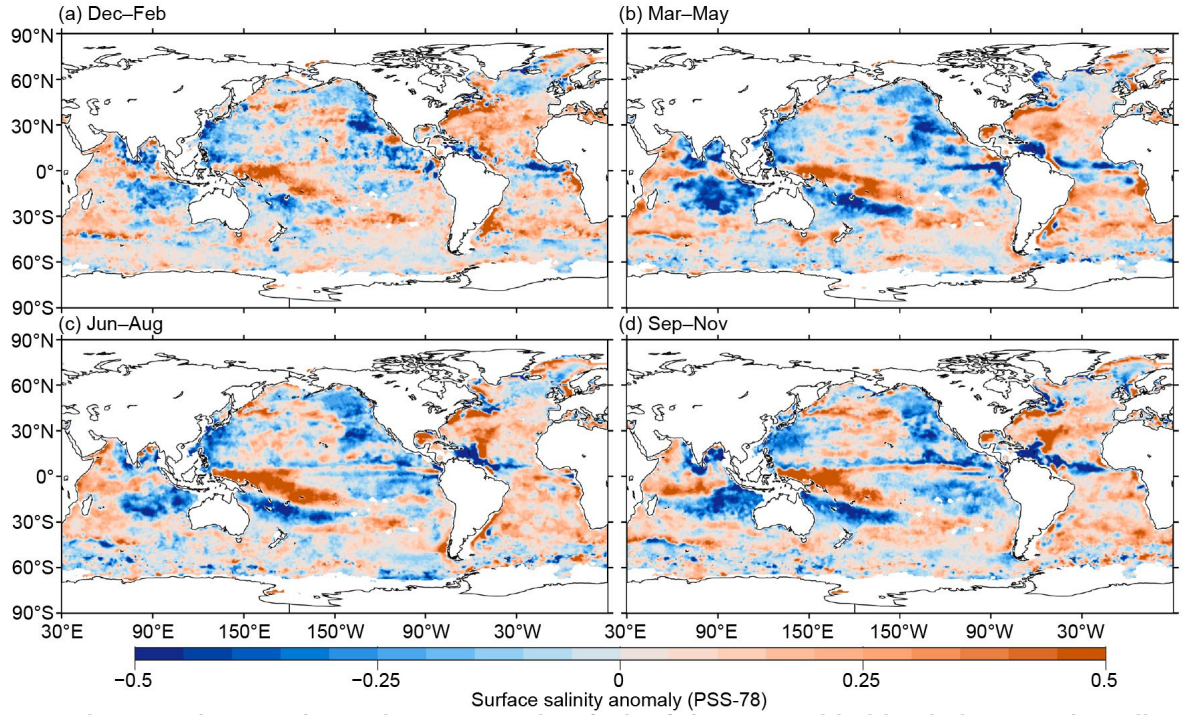

Fig. 3.8. Seasonal maps of sea-surface salinity anomalies (colors) from monthly blended maps of satellite and in situ salinity data (BASS; Xie et al. 2014) relative to monthly climatological 1955–2012 salinity fields from WOA13v2 for (a) Dec 2021–Feb 2022, (b) Mar–May 2022, (c) Jun–Aug 2022, and (d) Sep–Nov 2022.

3. SUBSURFACE SALINITY

J. Reagan, T. Boyer, C. Schmid, and R. Locarnini

Salinity is a conservative tracer and therefore is expected to retain much of its surface signature as it flows into the ocean's interior. Sinking into the ocean's interior primarily occurs through subduction (downward flow along constant density surfaces) and convection (deep vertical mixing; Talley 2002). Thus, in the absence of mixing, subsurface salinity anomalies will retain their surface footprint as they flow deeper into the ocean, which can ultimately impact ocean dynamics through changes in density.

The year 2022 was the third consecutive year the Atlantic basin exhibited only positive salinity anomalies from 0 m to 1000 m (Fig. 3.9a). The largest (>0.07) basin-averaged salinity anomalies in 2022 were constrained to depths between 75 m and 100 m with slightly smaller positive anomalies (~0.05) at the surface. Similar to 2020 and 2021, the 2022 monthly salinity anomalies below 100 m weakened with depth, reaching ~0.01 near 700 m. However, unlike in previous years back to 2016, there was no clear deepening of the Atlantic salinity anomalies in 2022 (Fig. 3.9a). This pattern is even more evident when examining the 2021 to 2022 Atlantic basin salinity changes

(Fig. 3.9b) and the 2021 to 2022 changes in zonally averaged salinity (Fig. 3.9c). Between 2021 and 2022, the upper 100 m freshened (maximum ~−0.015 at 50 m; Fig. 3.9b) which is primarily associated with 0-m to 100-m freshening centered at 10°N, 40°N, and 60°N (Figs. 3.9c and 3.7b). This near-surface freshening is consistent with the freshening from 2020 to 2021 (Fig. 3.9b in Reagan et al. 2022); however, unlike the salinification that had occurred from 100 m to 1000 m between 2020 and 2021, there was slight freshening from 100 m to 600 m (maximum of ~−0.002 at 300 m) between 2021 and 2022 (Fig. 3.9b).

In 2022, the structure of the 0-m to 1000-m Pacific basin-averaged salinity anomaly continued resembling the pattern that has existed since mid-2014, with near-surface fresh anomalies (upper 100 m) followed by a 100-m to 200-m thick salty subsurface anomaly layer followed by weak (<|0.01|) anomalies below (Fig. 3.9d). Fresh near-surface anomalies (<−0.03) that were common during the latter half of the 2010s have been absent since early 2020. The 2021 to 2022 salinification in the upper 30 m marked the fourth straight year in which salinity increased in this layer of the Pacific (Fig. 3.9e; Fig. 3.9e in Reagan et al. 2020, 2021, 2022). There is also salinification from 150 m to 250 m (maximum of ~0.005 at 200 m) and weak freshening from 300 m to 700 m (maximum of ~−0.002 at 400 m) from 2021 to 2022 in the Pacific (Fig. 3.9e). The upper 150 m significant zonally averaged salinity changes from 2021 to 2022 from 30°S to 30°N reflect the changes in precipitation patterns (Fig. 3.12b) and zonal geostrophic flow anomalies (Figs. 3.18a,b) as the Pacific reentered a La Niña in August of 2021 and remained there throughout 2022 (Fig. 3.9f; see Sidebar 3.1).

The 2022 0-m to 1000-m monthly Indian basin-averaged salinity anomalies were a continuation of the anomaly structure exhibited in both 2020 and 2021 (Fig. 3.9g; Reagan et al. 2021, 2022). The salinification that took place from 2020 to 2021 in the upper ~100 m (Fig. 3.9h in

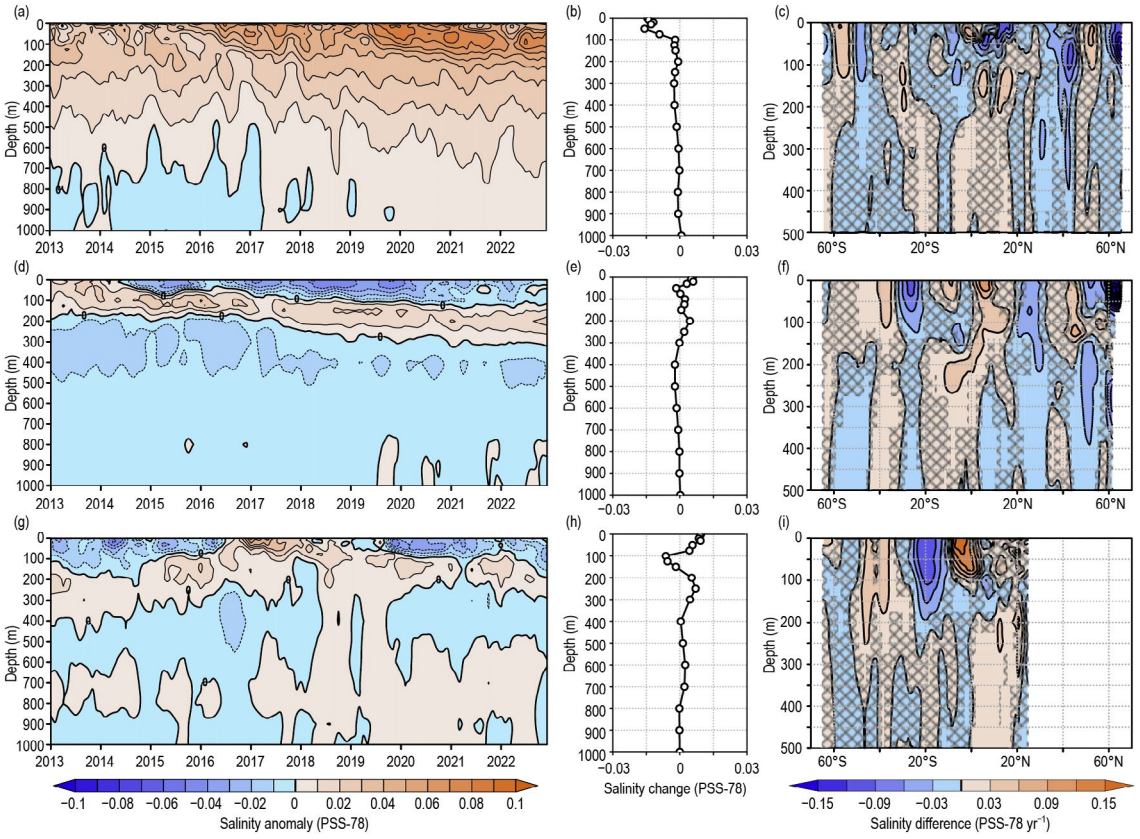

Fig. 3.9. Average monthly salinity anomalies from 0 m to 1000 m for 2013–22 for the (a) Atlantic, (d) Pacific, and (g) Indian basins. Change in salinity from 2021 to 2022 for the (b) Atlantic, (e) Pacific, and (h) Indian basins. Change in the 0 m to 500 m zonal-average salinity from 2021 to 2022 in the (c) Atlantic, (f) Pacific, and (i) Indian basins with areas of statistically insignificant change, defined as < ±1 std. dev. and calculated from all year-to-year changes between 2005 and 2022, stippled in dark gray. Data were smoothed using a three-month running mean. Anomalies are relative to the long-term (1955–2017) WOA18 monthly salinity climatology (Zweng et al. 2018).

Reagan et al. 2022) continued in 2022 (Fig. 3.9h) in the form of weakening fresh anomalies in the near-surface (upper 100 m, maximum of ~0.01 at 10 m). While the fresh anomalies weakened from 2021 to 2022, they also deepened, leading to freshening between 80 m and 160 m (maximum of ~−0.0075 at 100 m). The 2021 to 2022 significant zonally averaged salinity anomaly changes were primarily confined to the upper 200 m (Fig. 3.9i), with freshening centered at 20°S (maximum ~−0.09 at 50 m) and the salinification centered at 5°S (maximum ~0.15 at 10 m), a reflection of the persistent La Niña and the 2022 negative Indian Ocean dipole precipitation patterns (Fig. 3.12b). There was also significant salinification (~0.03) from 2021 to 2022 centered at 40°S and extending from the surface to 250 m (Fig. 3.9i).

Despite the Atlantic experiencing near-surface freshening for the past two years (Fig. 3.9b; Fig. 3.9b in Reagan et al. 2022) and slight subsurface freshening from 2021 to 2022 (Fig. 3.9b), the 2005–22 significant zonally averaged salinity trends (Fig. 3.10a) remained similar to the 2005–21 trends (Fig. 3.10a in Reagan et al. 2022) with salinification south of 45°N and freshening toward the Arctic. The 2005–22 Pacific significant zonally averaged salinity trends (Fig 3.10b) remained largely unchanged when compared to 2005–21 (Fig. 3.10b in Reagan et al. 2022). However, the La Niña-related near-equatorial near-surface salinification from 2021 to 2022 (Fig. 3.9f) reduced the significance of the 2005–22 freshening in this region. Finally, the 2005–22 Indian basin significant zonally averaged trends (Fig. 3.10c) strongly resemble those from 2005–21 (Fig. 3.10c in Reagan et al. 2022), despite the strong changes observed in the upper 200 m between 2021 and 2022 (Fig. 3.9i) associated with precipitation patterns from La Niña and negative IOD phases.

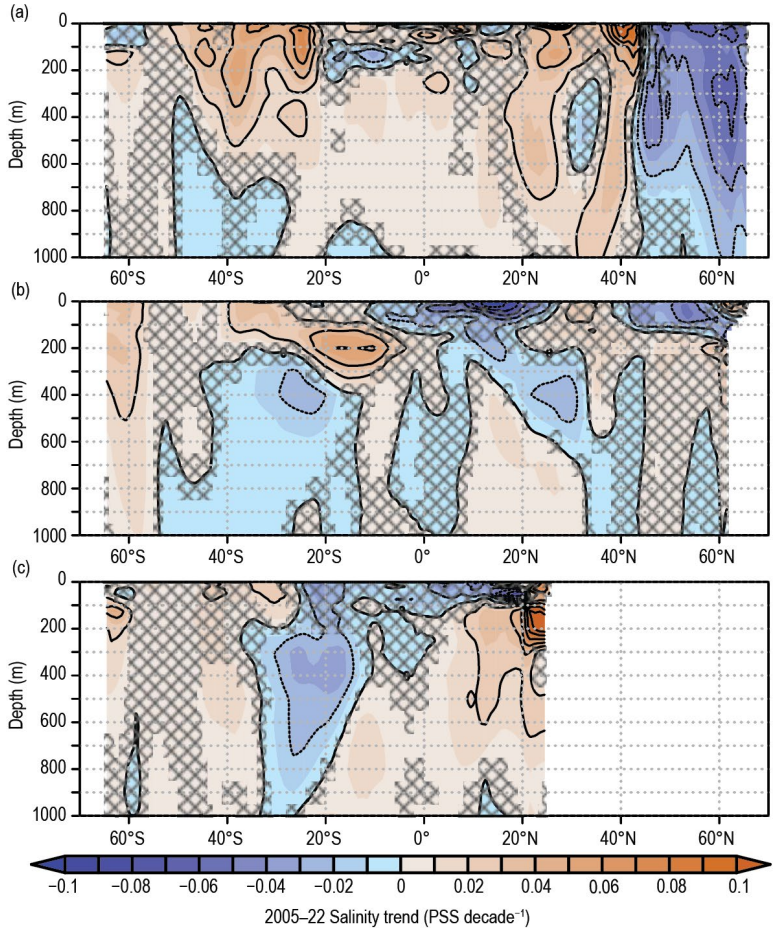

Fig. 3.10. The linear trend of zonally averaged salinity from 2005 to 2022 over the upper 1000 m for the (a) Atlantic, (b) Pacific, and (c) Indian basins. The salinity trend is per decade and computed using least squares regression. Areas that are stippled in dark gray are not significant at the 95% confidence interval.

e. Global ocean heat, freshwater, and momentum fluxes

—C. Wen, P. W. Stackhouse, Jr., J. Garg, P.-P. Xie, L. Zhang, and M. F. Cronin

Surface fluxes (i.e., heat, freshwater, and momentum fluxes) play a crucial role in keeping the energy and water cycles of the atmosphere–ocean coupled system in balance against external forcing from the Sun. Most of the shortwave radiation (SW) absorbed by the ocean's surface is vented into the atmosphere via net longwave radiation (LW) emitted by the ocean surface, turbulent heat loss by evaporation (latent heat flux, or LH), and by conduction (sensible heat flux, or SH) associated with air–sea temperature differences. The remaining heat acts to change the temperature of the near-surface water column and/or is transported away by the ocean's wind-driven circulation and mixed into the deeper ocean. Evaporation, which is associated with both a turbulent LH and moisture flux, connects the energy and water cycles. Evaporation minus precipitation (and in some regions runoff and ice melt or freezing) determines the local surface freshwater flux. Air–sea fluxes act as forces on both the ocean and atmosphere. Identifying air–sea flux anomalies is essential for understanding observed changes in surface water masses and in ocean circulation and its transport of heat and freshwater.

Here we examine surface heat fluxes, freshwater fluxes, and wind stress anomalies in 2022 and their differences from the previous year. The net surface heat flux, Q_{net}, is the sum of four terms: SW + LW + LH + SH. Monthly surface net SW and LW fluxes are from Clouds and the Earth's Radiant Energy Systems (CERES) Surface Energy Balanced and Filled (EBAF) Edition 4.2 (Kato et al. 2018) and the Fast Longwave And Shortwave Radiative Fluxes (FLASHFlux) version 4A product (Stackhouse et al. 2006; FLASHFlux fluxes from 2022 are radiometrically scaled to Surface EBAF Ed4.2). LH and SH are from European Centre for Medium-Range Weather Forecasts Reanalysis version 5 (ERA5; Hersbach et al. 2020). The net surface freshwater flux into the ocean (neglecting runoff from land and ice melting or formation) is simplified as Precipitation (P) minus Evaporation (E), or the $P–E$ flux. Monthly precipitation is from the Global Precipitation Climatology Project (GPCP) version 2.3 products (Adler et al. 2018). Monthly evaporation is from ERA5. Wind stress τ is also from ERA5. Ekman velocity is derived from τ following the equation $W_{EK} = 1/\rho\nabla\times(\tau/f)$, where ρ is the water density and f the Coriolis parameter.

1. SURFACE HEAT FLUXES

Global surface net heat-flux annual mean anomalies for 2022 relative to a 2001–15 climatology (Fig. 3.11a) showed strongest positive net heat fluxes (indicating a warming effect on the ocean surface) in the far western tropical South Pacific, the cold tongue in the tropical southeastern Pacific, and in the northeastern Pacific. In the eastern Pacific just north of the equator, a narrow band of negative net heat flux (dominated by turbulent heat fluxes cooling the ocean and warming the atmosphere) was associated with the northward movement of the Intertropical Convergence Zone (ITCZ), which can be seen in a northward shift of 2022 $P–E$ anomalies (Fig. 3.12a). The magnitudes of maximum positive and negative net heat-flux anomalies exceed 25 W m^{-2}. The distribution of net heat-flux anomalies is associated with the ongoing La Niña in 2022. In the far western tropical Pacific, over the Maritime Continent, enhanced convection/precipitation caused less SW into the ocean, giving rise to the negative 2022 net heat-flux anomaly in this region. For the area near the Coral Sea and central Pacific, SH+LH anomalies (not shown) were the primary factor contributing to the net heat-flux anomalies. The locations with positive net heat-flux anomalies coincided with locations with reduced wind anomalies, and those with negative heat-flux anomalies were associated with increased wind anomalies (Fig. 3.13), consistent with the larger turbulent flux anomalies relative to the radiative flux anomalies in these regions. In regions where winds were moderate and less variable, LH+SH heat release into the atmosphere decreased with decreasing sea-surface temperature (SST) and vice versa. During the 2022 La Niña, SST anomalies (see Fig. 3.1a) in the southeastern Pacific were below –1°C, giving rise to less LH+SH release compared to normal years. In the tropical Indian Ocean, the negative IOD pattern in 2022 was associated with negative net heat-flux anomalies in the southeastern Indian Ocean and positive net heat- flux anomalies in the northwestern Indian Ocean.

In the North Pacific, the 2022 net heat flux anomaly distribution displayed a positive phase Pacific Decadal Oscillation-like pattern (Mantua and Hare 2002), with negative net heat-flux anomalies dominating the western-central Pacific between 25°N and 50°N, surrounded by positive anomalies. In the North Pacific, 2022 SST anomalies (see Fig. 3.1) in regions with positive net heat-flux anomalies were below average and vice versa. The anti-phase relationship between Q_{net} and SST anomalies suggests that surface heat flux acted as a damping of the local SST anomalies there. This anti-phase relationship did not apply to the North Atlantic Ocean in 2022. Negative Q_{net} anomalies were present near the Labrador Sea, with positive Q_{net} anomalies found south of 40°N. The negative ocean net heat-flux anomalies were associated with marked enhanced surface wind anomalies and vice versa (Figs. 3.11a and 3.13a). A similar dipole pattern of SST anomaly, albeit centered on ~50°N, was also observed in the North Atlantic (see Fig. 3.1).

The 2022-minus-2021 Q_{net} difference map (Fig 3.11b) has a similar spatial structure to the 2022 anomaly map in most regions. 2022 was the third year of a triple-dip La Niña event (see Sidebar 3.1), and La Niña intensity slightly strengthened in 2022 relative to 2021, with stronger SST cooling (~0.2°C cooler; see Fig. 3.1a) and trade winds in the central-eastern tropical Pacific (Fig. 3.13b). The magnitude and pattern of LH+SH 2022-minus-2021 differences were close to those of Q_{net} differences. A pronounced dipole pattern in the subpolar North Atlantic (40°N–70°N) suggests that the LH+SH change was the primary factor contributing to Q_{net} 2022-minus-2021 differences. The SW+LW differences had similar sign to LH+SH differences in most regions although the amplitude of the former was smaller.

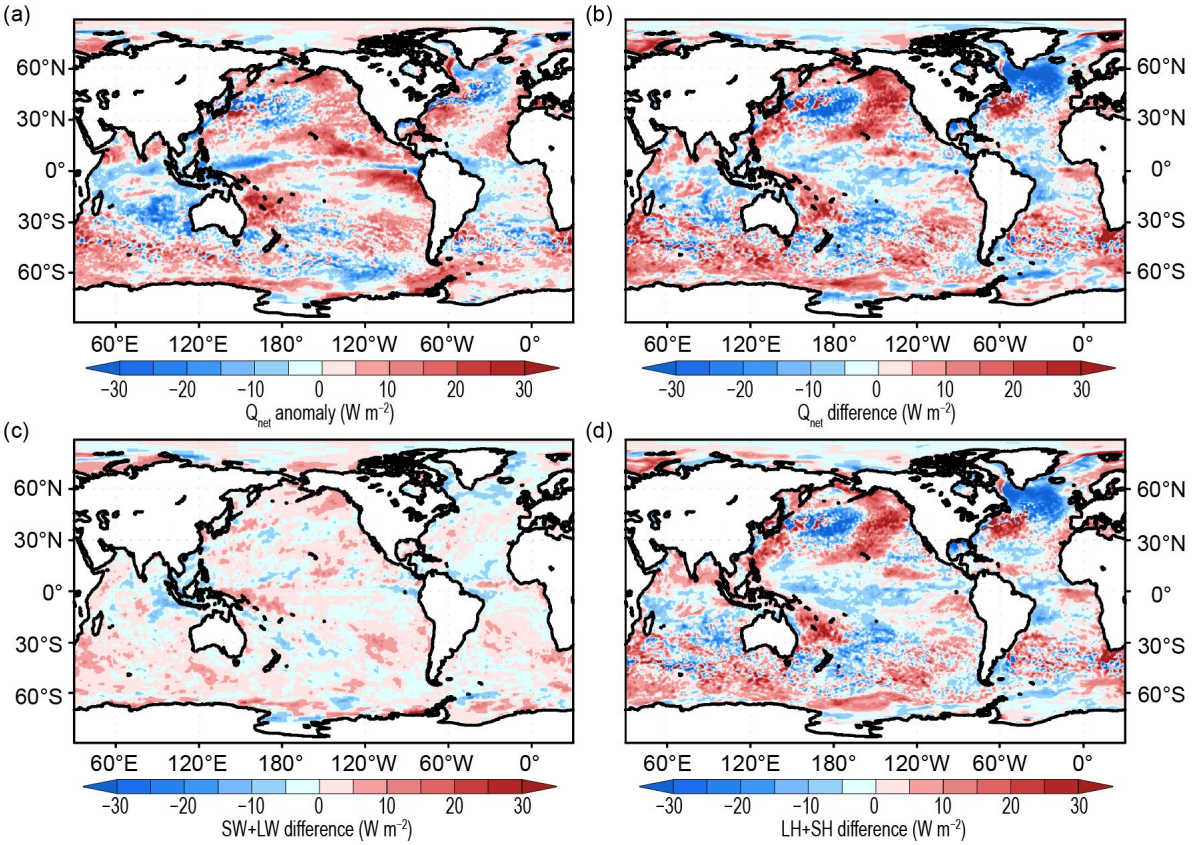

Fig. 3.11. (a) Surface heat flux (Q_{net}) anomalies for 2022 relative to the 2001–15 climatology. Positive values denote ocean heat gain. (b) 2022-minus-2021 difference for Q_{net}, (c) net surface radiation shortwave + longwave (SW+LW), and (d) turbulent heat fluxes latent heat + sensible heat (LH+SH), respectively. Positive tendencies denote more ocean heat gain in 2022 than in 2021. All units are in W m^{-2}. LH+SH is from ERA5, and SW+LW is from the NASA FLASHFlux version 4A adjusted to CERES Surface EBAF Ed4.2. Net radiative fluxes defined as the difference between the incoming and outgoing radiation (positive indicates radiative flux into the ocean).

2. SURFACE FRESHWATER FLUXES

As expected, *P–E* anomalies in 2022 (Fig. 3.12a) exhibit a large-scale distribution generally reminiscent of sea-surface salinity anomalies (see Fig. 3.7a). The largest *P–E* anomalies in 2022 were found in the tropics. Strong positive (>60 cm yr^{-1}) *P–E* anomalies (a freshening effect on the ocean surface) were located west of the Maritime Continent that acts as a border between the Pacific and Indian Oceans and over the Coral Sea, while large negative *P–E* anomalies (indicating a salinification effect on the ocean surface) spread over much of the equatorial Pacific and southern tropical Pacific regions. The largest *P–E* anomaly exceeded 60 cm yr^{-1}. The pattern is consistent with the La Niña-associated SST anomaly distribution (see Fig. 3.2), where above-normal SST in the western Pacific and below-normal SST in the central-eastern Pacific cause the centers of east–west-oriented Walker circulation to shift westward (see Sidebar 3.1). For the Indian Ocean, in addition to the La Niña impact, the negative Indian dipole mode event enhanced the dipole pattern with a positive 2022 *P–E* anomaly over the eastern Indian Ocean and a negative anomaly over the western Indian Ocean. In the tropical Atlantic Ocean, a positive *P–E* anomaly dominated the Atlantic ITCZ, which is often observed during La Niña years.

The 2022-minus-2021 *P–E* difference (Fig. 3.12b) is similar to the 2022 anomaly (Fig. 3.12a) in the Pacific and Indian Oceans. This is consistent with SST differences (see Fig. 3.1b) and surface-wind stress differences (Fig. 3.13b), where stronger east–west SST gradients led to a stronger Walker circulation and stronger convection in the western Pacific. For the Atlantic Ocean, negative *P–E* differences are observed north of the equator and are not found in the *P–E* anomaly map for 2022. This is because an extremely strong Atlantic Niño occurred in 2021 (Crespo et al. 2022) while 2022 was a normal year. Similar to its counterpart in the Pacific, strong warming in the eastern Atlantic Ocean tends to enhance precipitation near the Gulf of Guinea (Vallès-Casanova et al. 2020). Overall, the *P–E* differences are determined primarily by *P* changes (Fig. 3.12d) and secondarily by *E* (Fig.3.12c). Note the centers of SW+LW differences (Fig .3.11c) have a high negative correlation with *P* differences, where areas with increased SW+LW coincide with areas of reduced precipitation.

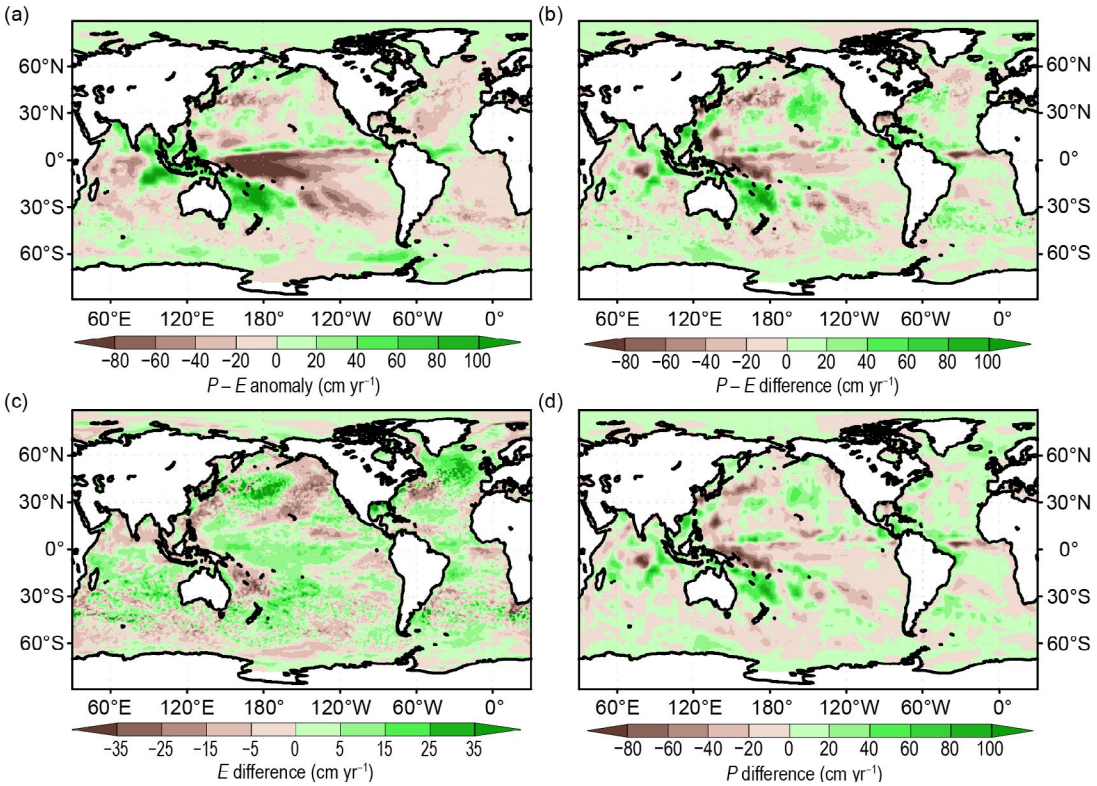

Fig. 3.12. (a) Surface freshwater precipitation minus evaporation (*P–E*) flux anomalies (cm yr^{-1}) for 2022 relative to the 1988–2015 climatology. Positive values denote ocean freshwater gain. (b)–(d) 2022-minus-2021 differences for (b) *P–E*, (c) evaporation (*E*), and (d) precipitation (*P*). Positive values denote ocean freshwater gain, and negative values denote ocean freshwater loss. *P* is from the GPCP version 2.3 product, and *E* is from ERA5.

3. WIND STRESS

The 2022 wind-stress anomalies (Fig. 3.13a) exceeded 0.02 N m^{-2} in the mid-high latitudes and over the central tropical Pacific Ocean. In the Southern Hemisphere, strong positive anomalies exceeding 0.04 N m^{-2} were observed over the Antarctic Circumpolar Current (ACC) region between 50°N and 60°N, where the westerly winds were strengthened. Enhanced easterly trade winds were present over the central equatorial Pacific, a canonical La Niña signature. Wind enhancement was also observed in the north subpolar Atlantic (50°N–70°N). Significant wind changes from 2021 to 2022 (>0.02 N m^{-2}; Fig. 3.13b) were mainly in the mid-high latitudes. Anticyclone-like changes were present in the North Pacific, with westerly winds strengthened near the Kuroshio and weakened northwesterly winds along the west coast of North America. In the North Atlantic, easterly winds strengthened substantially south of Greenland, with wind stress changes exceeding 0.04 N m^{-2}.

Surface winds not only influence the ocean by modulating heat fluxes, but also by redistributing water masses via wind-driven currents. The spatial variations of winds and meridional gradient of the Coriolis parameter lead to divergence and convergence of the Ekman transport, which results in a vertical velocity W_{EK} at the base of Ekman layer, denoted as Ekman pumping (downwelling, downward direction) and Ekman suction (upwelling, upward direction). The 2022 W_{EK} anomalies (Fig. 3.13c) were large and negative (<–12 cm day^{-1}) in the western Pacific and in a narrow band north of the equator. A narrow band of positive anomalies (upwelling) was present near the central and eastern equatorial region of the Pacific, a typical La Niña pattern. Strong positive anomalies (>12 cm day^{-1}) were also present in the northeastern Indian Ocean. The 2022-minus-2021 W_{EK} differences suggest enhanced downwelling in the western equatorial Pacific, consistent with the strengthening warming in the western Pacific.

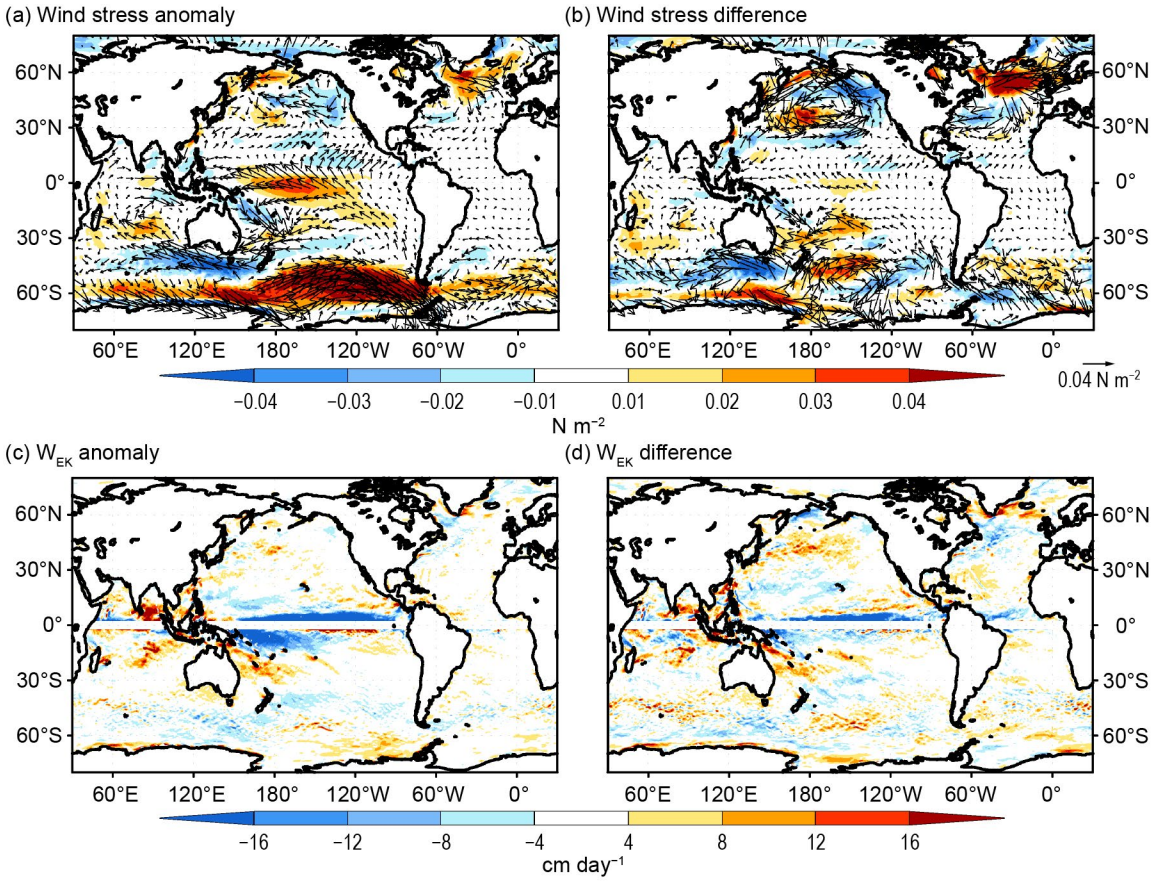

Fig. 3.13. (a) Wind stress magnitude (shaded) and vector anomalies (N m^{-2}) for 2022 relative to a 1988–2015 climatology. (b) 2022-minus-2021 differences in wind stress (N m^{-2}). (c) Ekman vertical velocity (W_{EK}; cm day^{-1}) anomalies for 2022 relative to a 1988–2015 climatology. Positive (negative) values denote upwelling (downwelling). (d) 2022-minus-2021 differences of W_{EK} (cm day^{-1}). Wind stress fields are from ERA5.

4. LONG-TERM PERSPECTIVE

A long-term perspective on the change of ocean surface fluxes is examined in the context of annual-mean series of Q_{net}, *P*–*E*, and wind-stress magnitude anomalies averaged over the global ocean (Figs. 3.14a–c). The Q_{net} time series commenced in 2001, when CERES EBAF4.2 surface radiation products became available. Q_{net} anomalies are relative to the 2001–15 climatology. Both *P*–*E* and wind-stress time series start from 1988 when Special Sensor Microwave/Imager satellite retrievals are available. Annual mean anomalies are relative to 1988–2015 climatology.

While accurately determining the order 1 W m^{-2} net energy flux entering the ocean from global ocean average Qnet would be very challenging, the time series does exhibit decadal fluctuations. The Q_{net} anomaly decreased from +1.5 W m^{-2} in 2001 to –2 W m^{-2} in 2010 and then gradually increased to the peak value of +2.8 W m^{-2} in 2019. Q_{net} displayed a decreasing trend during the 2020–22 triple-dip La Niña event. The *P*–*E* time series displayed a clear downward trend during 1988–2022. The global average *P*–*E* anomaly was above normal prior to 1998 and generally below normal thereafter. During 2015–22, *P*–*E* variations were closely related to El Niño–Southern Oscillation conditions. The global *P*–*E* anomaly was close to zero during 2015 and then decreased during the double-dip 2016/17 La Niña. After the *P*–*E* rebounded to zero in the 2019 El Niño year, *P*–*E* continued to decrease during the triple-dip La Niña and reached the historical low in 2022 (~5.4 cm yr^{-1}). Wind stress was strongest during the 1998 La Niña. Wind stress anomalies remained above average after 2010, consistent with more frequent La Niñas in the last decade.

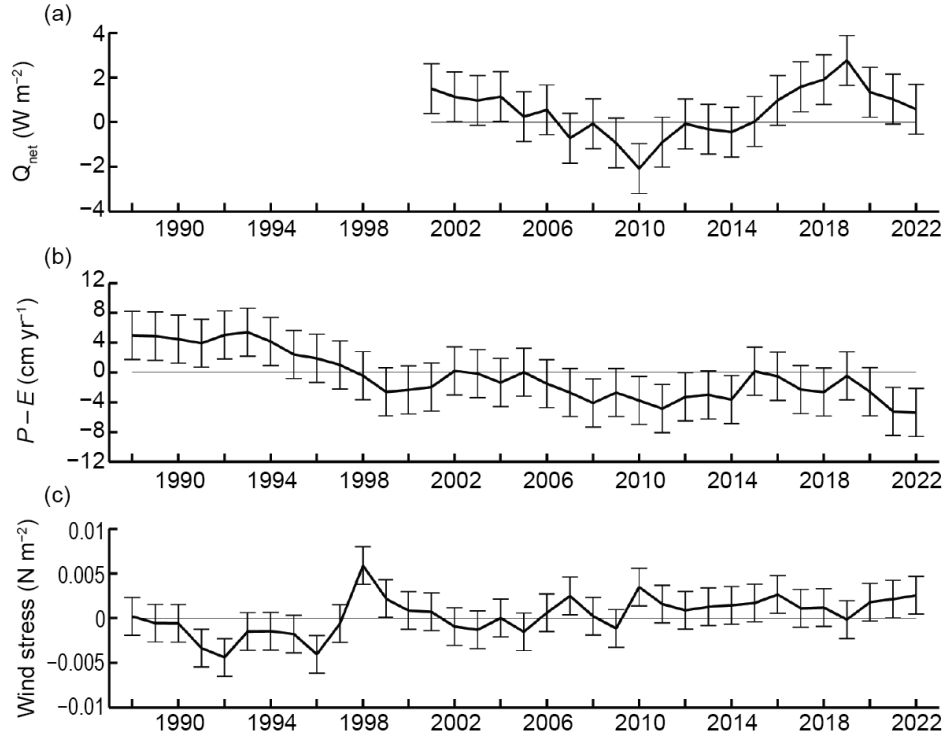

Fig. 3.14. Annual-mean time series of global average of ocean-only (a) net surface heat flux (Q_{net}; W m^{-2}) from a combination of CERES EBAF4.2 shortwave radiation + longwave radiation (SW + LW) and ERA5 latent heat flux + sensible heat flux (LH+SH). The 2022 Q_{net} is based on FLASHFlux SW+LW as adjusted to EBAF and ERA5 LH+SH. (b) Net freshwater flux anomaly precipitation minus evaporation (*P*–*E*; cm yr^{-1}) from a combination of *P* and ERA5 *E*. (c) Wind stress magnitude anomalies (N m^{-2}) from ERA5. Error bars denote 1 std. dev. of annual-mean variability.

f. Sea-level variability and change

—P. R. Thompson, M. J. Widlansky, E. Leuliette, D. P. Chambers, W. Sweet, B. D. Hamlington, S. Jevrejeva, M. A. Merrifield, G. T. Mitchum, and R. S. Nerem

Annual average global mean sea level (GMSL) from satellite altimetry (1993–present) reached a new high in 2022, rising to 101.2 mm above 1993 (Fig. 3.15a). This marks the 11th consecutive year (and 27th out of the last 29) that GMSL increased relative to the previous year, reflecting an ongoing multi-decadal trend of 3.4±0.4 mm yr^{-1} in GMSL during the satellite altimetry era (Fig. 3.15a). A quadratic fit with corrections for the eruption of Mount Pinatubo (Fasullo et al. 2016) and El Niño–Southern Oscillation effects (Hamlington et al. 2020) yields a climate-driven trend of 3.0±0.4 mm yr^{-1} and acceleration of 0.081±0.025 mm yr^{-2} (updated from Nerem et al. 2018).

Independent observing systems measure the contributions to GMSL rise from increasing ocean mass, primarily due to melting of glaciers and ice sheets (see sections 5f, 6d, 6e), and decreasing ocean density, primarily due to ocean warming (section 3c). Data from Argo profiling floats analyzed by Scripps Institution of Oceanography (SIO; Roemmich and Gilson 2009) show a global mean steric (i.e., density-related) sea-level trend of 1.3±0.2 mm yr^{-1} during 2005–22 (Fig. 3.15a). Global ocean mass (excluding regions within 300 km of land) produced by the NASA Jet Propulsion Laboratory using mass concentration anomalies from the Gravity Recovery and Climate Experiment (GRACE) and GRACE Follow-On (GRACE-FO) missions show a global mean ocean-mass trend of 2.1±0.4 mm yr^{-1} during 2005–22 (Fig. 3.15a). The sum of these trend contributions, 3.4±0.4 mm yr^{-1}, agrees within uncertainties with the GMSL trend of 3.9±0.4 mm yr^{-1} measured by satellite altimetry since 2005 (Leuliette and Willis 2011; Chambers et al. 2017). Consistency among trends from these independent observing systems is a significant achievement and increases confidence in estimates of Earth's energy imbalance (e.g., Hakuba et al. 2021; Marti et al. 2022).

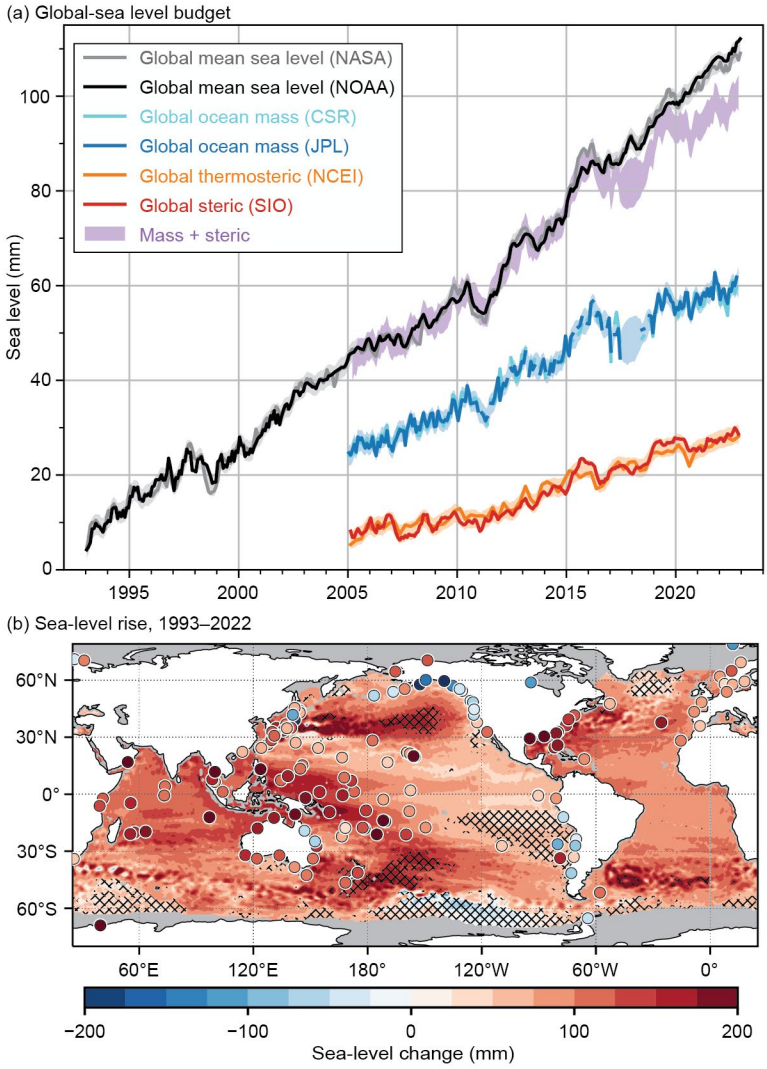

Fig. 3.15. (a) Global mean sea level (GMSL; mm) observed by satellite altimeters (1993–2022) from the NOAA Laboratory for Satellite Altimetry (black) and NASA Sea Level Change Program (gray). Monthly global ocean mass (2005–22) from GRACE and GRACE-FO calculated from mass concentrations produced by NASA JPL (blue) and University of Texas Center for Space Research (CSR, cyan). GRACE and GRACE-FO data within 300 km of land were excluded in both ocean mass time series. Monthly global mean steric sea level (2004–22) from SIO Argo data (red). Monthly global mean thermosteric sea level from NCEI Argo and hydrographic data (orange). Monthly global ocean mass plus steric (purple). Shading around all data sources represents a 95% confidence range based on Gaussian process regressions onto each pair of time series. (b) Total local sea-level change (mm) during 1993–2022 as measured by satellite altimetry (contours) and tide gauges (circles). Hatching indicates local changes that differ from the change in GMSL by more than 1 std. dev. Altimetry data used to generate the trend map were obtained from the NASA MEaSUREs Gridded Sea Surface Height Anomalies Version 2205. Tide-gauge observations were obtained from the University of Hawaii Sea Level Center Fast Delivery database.

Annually averaged GMSL from satellite altimetry increased 3.3±0.7 mm from 2021 to 2022, exceeding the sum of year-over-year increases in global mean steric sea level from Argo, 1.9±0.4 mm, and global mean ocean mass from GRACE-FO, 0.2±0.7 mm. The sum of global steric and mass increases, 2.1±1.0 mm, is less than the observed increase in GMSL from altimetry, but the two do agree within standard error uncertainties. A portion of the discrepancy may be due to incomplete annual updates to the global steric and mass time series, which at the time of writing were updated through November and October 2022, respectively. The increase in GMSL from satellite altimetry through October 2022 was 2.73±0.6 mm, which reduces the discrepancy between year-over-year increases in the budget terms by almost half.

Sea-level budget misclosure is larger since 2016 (Fig. 3.15a; Chen et al. 2020). This misclosure does not seem likely to be owing to one cause. Uncertainties in the global mass budget (e.g., leakage near land, geocenter, and glacial isostatic adjustment) do warrant investigation (Chen et al. 2020). Error sources in the altimeter measurements, such as the wet tropospheric correction, may also contribute (Barnoud et al. 2021). Drift in Argo salinity measurements (Roemmich et al. 2019) can artificially suppress increasing global mean steric sea level, but quality-control procedures applied in the SIO data product used here mitigate that impact (Barnoud et al. 2021). The SIO time series of steric sea level compares favorably with a time series of global mean thermosteric sea level from the NOAA National Centers for Environmental Information (Fig. 3.15a). Undersampling of the ocean by Argo, especially around the Malay Archipelago between Asia and Australia (von Schuckmann et al. 2014), could also lead to underestimates of global mean steric rise.

Spatial structure in sea-level changes over the 30-year altimeter record (Fig. 3.15b) is due to a combination of natural fluctuations in coupled modes of atmosphere–ocean variability (Han et al. 2017) and the oceanic response to anthropogenic radiative forcing (Fasullo and Nerem 2018). As the altimetry record grows in length, the impact of natural fluctuations on regional sea-level trends decreases. Presently, only a small fraction of the global ocean has experienced sea-level trends that differ from the global mean trend by more than one standard deviation (hatched areas, Fig. 3.15b). Reduced sea-level trends in the tropical eastern Pacific reflect the impact of multidecadal variability in the strength of Pacific trade winds (e.g., Merrifield 2011), while enhanced sea-level change in the high latitude South Pacific can be attributed to regional warming (Llovel and Terray 2016; Volkov et al. 2017). Sea-level change relative to land (i.e., the quantity measured by tide gauges; circles, Fig. 3.15b) is most relevant for societal impacts and can differ substantially from satellite-derived changes in tectonically active regions (e.g., Japan) and areas strongly affected by glacial isostatic adjustment (e.g., Alaska; Fig. 3.15b).

Annual sea-level anomalies during 2022 were positive nearly everywhere (Fig. 3.16a), mostly because of the long-term trend of rising sea levels (Fig. 3.15b). In the tropics, the highest sea-level anomalies were in the western Pacific and the eastern Indian Ocean (exceeding 15 cm above normal in some locations), whereas the lowest anomalies were in the northeastern Pacific (about 5 cm below normal). In the midlatitudes of both hemispheres (i.e., between the 30°–60° latitudes), sea-level anomalies also exceeded 15 cm in places, especially in the extension regions of the Kuroshio and Gulf Stream Currents. Upwelling mesoscale eddy activity in the midlatitudes contributed to small-scale areas of negative sea-level anomalies (e.g., east of Japan and in the North Atlantic).

Prolonged La Niña conditions that developed during mid-2020 re-intensified during 2021, and continued throughout all of 2022 (see Sidebar 3.1 and section 4b) explain the mostly consistent sea-level pattern in the equatorial Pacific during the past three years (Fig. 3.16b). In 2022, a noticeable change from 2021 was in the tropical southwestern Pacific where sea-level anomalies increased by about 10 cm (a similar change also occurred in the southeastern part of the tropical Indian Ocean). In this so-called South Pacific Convergence Zone region (Brown et al. 2020), the largest expanse of sea-level anomalies exceeded 15 cm above normal. The largest regions of

decreasing sea levels during 2022 compared to 2021 were in the tropical North Pacific and the North Indian Oceans. Sea levels around Hawaii decreased about 5 cm and were near normal for the year (i.e., locally, the year-to-year change mostly cancelled the long-term sea-level rise trend). In the Atlantic, 2022-minus-2021 differences were mostly positive along the U.S. East Coast, in the Gulf of Mexico, throughout the Caribbean Sea, and just north of the equator (most of these changes were less than 10 cm). In the midlatitudes, year-to-year sea-level changes were typically larger, especially in the regions most affected by mesoscale oceanic eddies.

In 2022, the triple-dip La Niña (see Sidebar 3.1) is associated with the continuation of above-normal sea levels in the western half of the equatorial Pacific. Long-term sea-level rise partially masks a negative sea-level anomaly in the eastern Pacific otherwise expected during La Niña. During 2022, only minor inter-seasonal changes are evident in the comparison of December 2021–February 2022 (DJF) and September–November 2022 (SON) anomalies (Figs. 3.16c,d). In the Indian Ocean, the sea-level pattern showed evidence of the Dipole Mode Index becoming more negative during 2022 (i.e., sea-level anomalies decreasing in the west and increasing in the east; see section 4f). Some of the highest regional sea-level anomalies during 2022 occurred in the Bay of Bengal as well as near western Australia, where in both places satellite-observed seasonal anomalies exceeded 15 cm above normal during SON. In the northwestern Atlantic Ocean, seasonal sea-level anomalies were consistently above normal during 2022, with only minor differences comparing DJF and SON near the U.S. East Coast.

Ongoing trends, year-to-year variability, and seasonal changes in sea level impact coastal communities by increasing the magnitude and frequency of positive sea-level extremes that contribute to flooding and erosion. Minor impacts tend to emerge when local water levels exceed the 99th percentile of daily sea-level maxima (Sweet et al. 2014). Using 1993–2022 as the analysis epoch (consistent with the altimetry baseline), daily sea-level maxima that exceed the 99th percentile—hereafter extreme sea-level events—occurred more frequently in recent years compared to previous decades. Across 119 tide-gauge locations with sufficient data volume and quality for analysis, the median number of extreme sea-level events per year and location

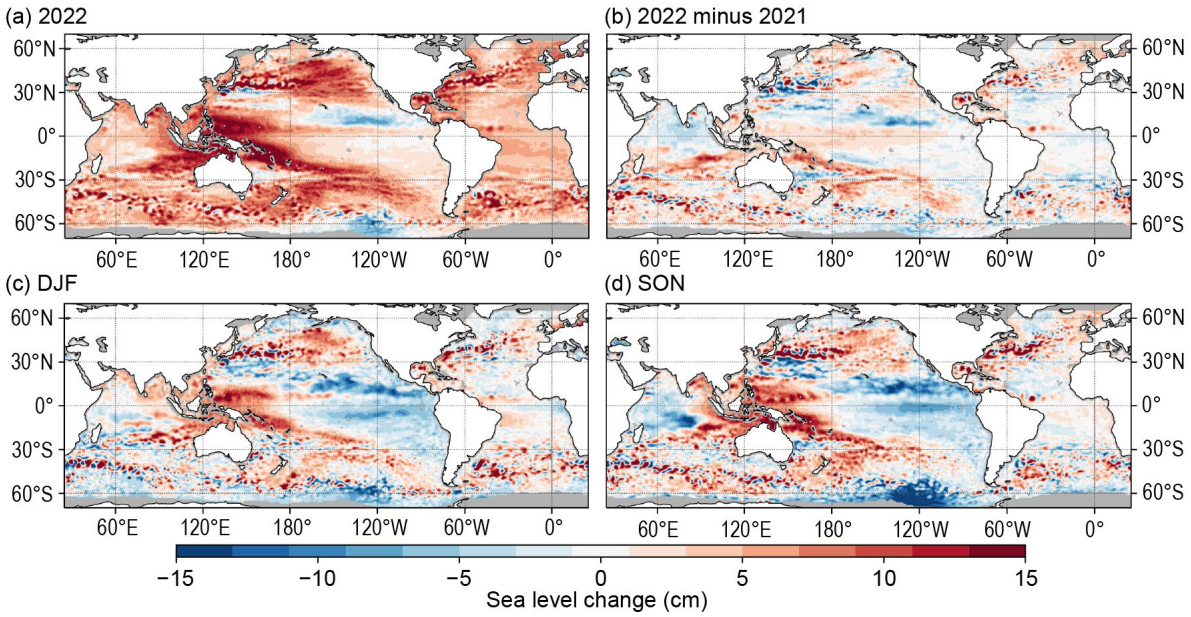

Fig. 3.16. (a) Annual average sea-level anomaly during 2022 relative to average sea level at each location during 1993–2022. (b) Average 2022-minus-2021 sea-level anomaly. (c) Average sea-level anomaly during DJF 2021/22 relative to the 1993–2022 DJF average. (d) Same as (c), but for SON. Units are given in cm. Global mean sea level was subtracted from panels (c),(d) to emphasize regional, non-secular change. Altimetry data were obtained from the NASA MEaSUREs Gridded Sea Surface Height Anomalies Version 2205.

increased from one during 1993–97 to six during 2018–22 (not shown). The 90th percentile of events per year and location increased from 6 during 1993–97 to 15 during 2018–22 (not shown).

Twenty-nine of the 119 locations experienced more than 10 extreme sea-level events during 2022, concentrated in the southwestern Pacific and along western boundary currents in the Northern Hemisphere (Fig. 3.17a) where annual sea-level anomalies were largest (Figs. 3.16a, 3.17b). The greatest numbers of events occurred in the Solomon Islands (51) and Papua New Guinea (37), which experienced high sea-level anomalies related to ongoing La Niña conditions (Fig. 3.16a). The elevated numbers of events in the North Atlantic western boundary current system reflect elevated coastal sea levels due to the combined effects of warm ocean heat content anomalies (see Fig. 3.4a) and weaker-than-average geostrophic currents during the latter third of the year (see Fig. 3.22b) when the seasonal cycles in ocean temperature and tidal amplitude peak. Just 8 locations experienced increases of more than 10 extreme events from 2021 to 2022 (Fig. 3.17c), reflecting the generally moderate year-over-year differences in annual mean sea level across the global ocean (Figs. 3.16b, 3.17d). Ten locations experienced at least 10 fewer extreme events per year in 2022 compared to 2021, concentrated in the Pacific and Indian Oceans (Fig. 3.17c) in areas where annual mean sea level during 2022 was either mostly unchanged or lower compared to the prior year (Figs. 3.16b, 3.17d).

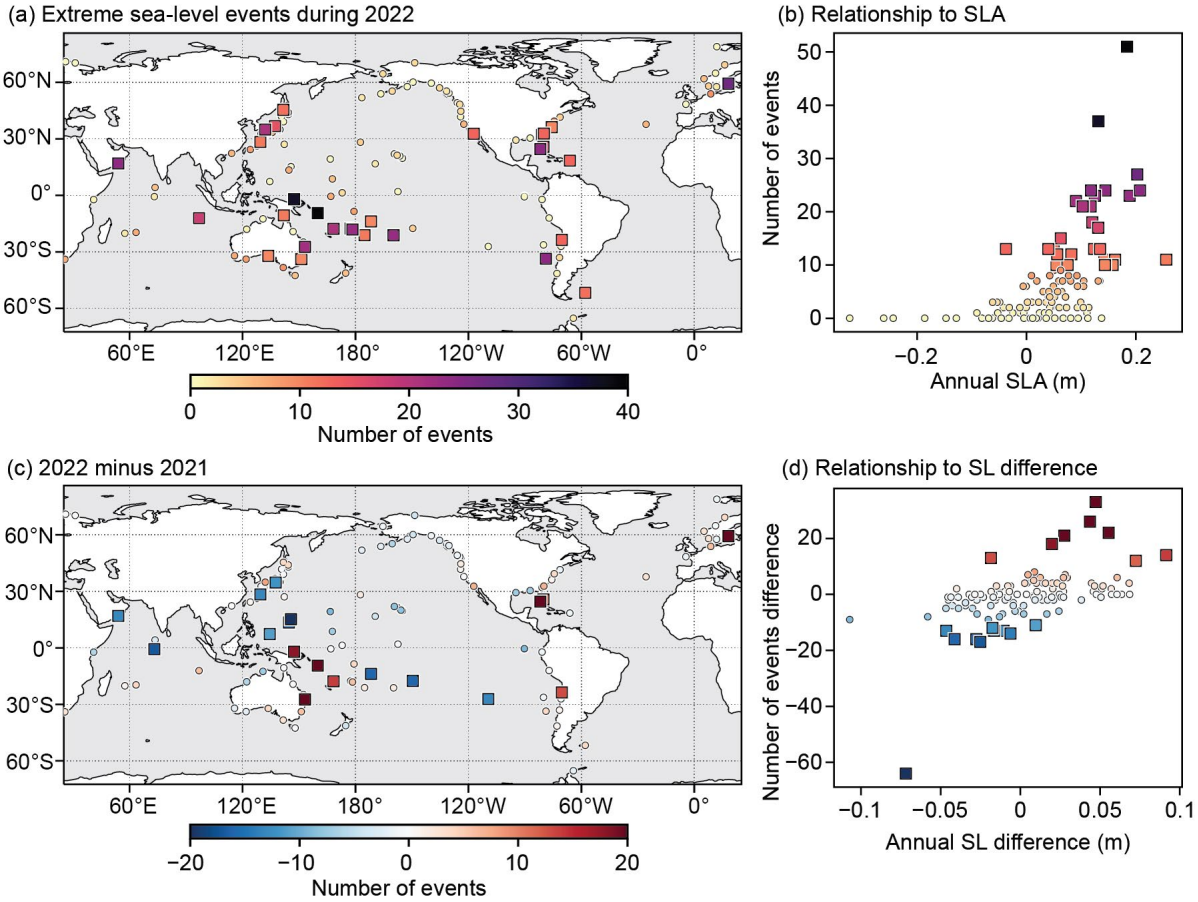

Fig. 3.17. (a) Number of extreme sea-level (SL) events from tide gauges during 2022. (b) Counts in (a) as a function of annual sea-level anomaly (SLA) during 2022. Square markers in (a) and (b) highlight locations with more than 10 extreme events. (c) Change in number of extreme SL events from 2021 to 2022. (d) Counts in (c) as a function of the change in annual SL from 2021 to 2022. Square markers in (c) and (d) highlight locations where the magnitudes of changes in counts of extreme events were greater than 10. Counts of extreme SL events were calculated from hourly tide gauge observations obtained from the University of Hawaii Sea Level Center Fast Delivery database. Only records with at least 80% completeness during 1993–2022 and 80% completeness during both 2021 and 2022, individually, were analyzed.

g. Surface currents

—R. Lumpkin, F. Bringas, G. Goni, and B. Qiu

This section describes variations of ocean surface currents, transports, and associated features, such as rings. Surface currents are obtained from in situ and satellite observations. Transports are derived from a combination of sea-surface height anomaly (from altimetry) and climatological hydrography. See Lumpkin et al. (2012) for details of these calculations. Zonal surface-current anomalies are calculated with respect to a 1993–2020 climatology and are discussed below for individual ocean basins.

1. PACIFIC OCEAN

In 2022, zonal currents in the equatorial Pacific (Fig. 3.18a) exhibited annual mean westward current anomalies of 10 cm s^{-1} on the equator from 140°E–115°W, with the strongest anomalies of 20 cm s^{-1} at 150°E–170°E, associated with the persistent La Niña conditions throughout the year (see Sidebar 3.1 and Fig. 4 of Lumpkin and Johnson 2013) and strengthened trade winds in the western half of the basin (Fig. 3.13a). Eastward anomalies of 8 cm s^{-1} to 10 cm s^{-1} were present at 6°N–8.5°N, 90°W–175°W, consistent with an intensification and slight northward shift of the eastward North Equatorial Countercurrent (NECC) from its climatological peak of 30 cm s^{-1} at 6.5°N to 40 cm s^{-1} at 7°N and with eastward wind anomalies in this region (Fig. 3.18a).

In 2021/22, the annual-average latitude of the Kuroshio Extension in the region 141°E–153°E, 32°N–38°N was shifted north of its long-term (1993–2022) location of 35.4°N, to 36.8°N (2021) and 36.6°N (2022), as seen by alternating eastward/westward anomalies in Fig. 3.18a that persisted

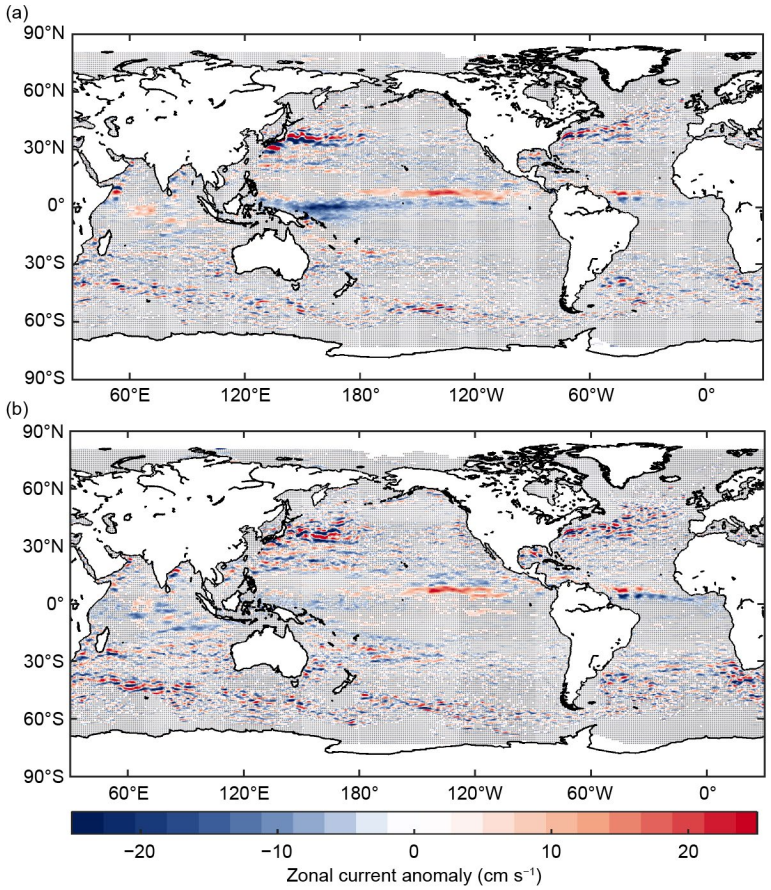

Fig. 3.18. Annually averaged geostrophic zonal current anomalies (cm s^{-1}) for (a) 2022 and (b) 2022 minus 2021 derived from a synthesis of drifters, altimetry, and winds. Values are stippled where they are not significantly different from zero.

through the year (Fig. 3.19) and also in a band of increased ocean heat content anomaly (see Fig. 3.4a). This 2021/22 shift was the largest northward shift in the 1993–2022 record (Fig. 3.20c) and corresponded with a two-year increase in averaged eddy kinetic energy (EKE) of 0.03 $m^2 s^{-2}$ above the long-term average of 0.12 $m^2 s^{-2}$ (Fig 3.20d); this pattern is inconsistent with

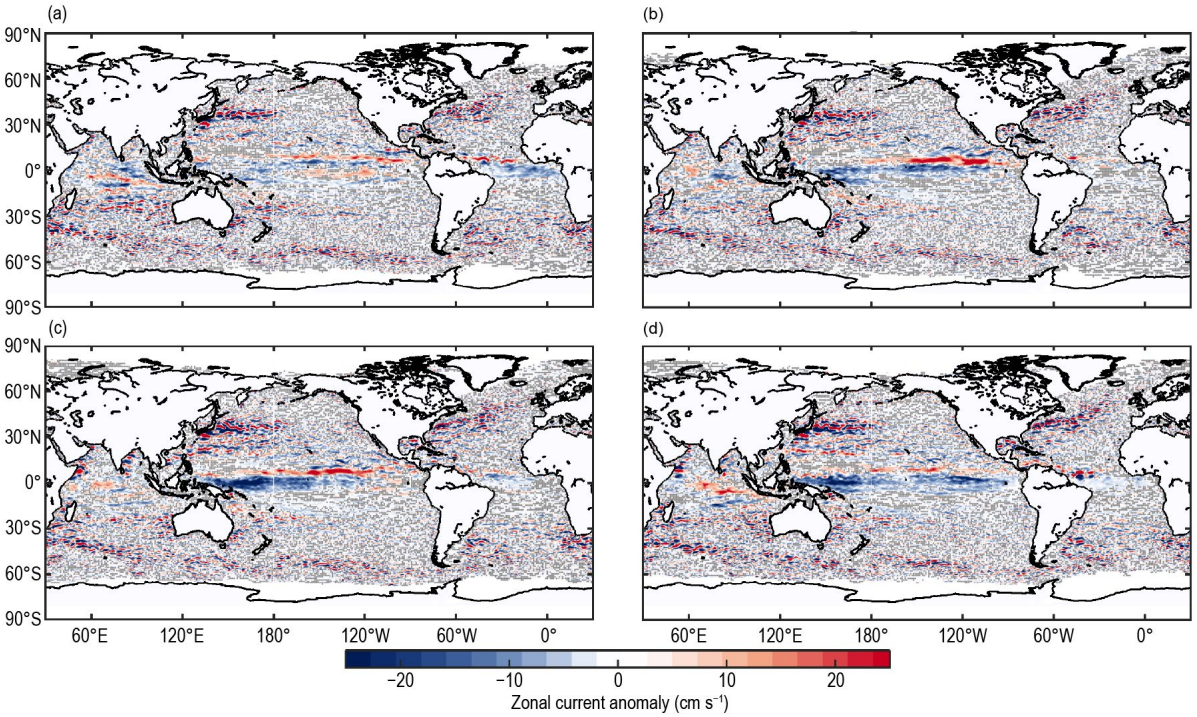

Fig. 3.19. Seasonally averaged zonal geostrophic anomalies (cm s^{-1}) with respect to seasonal climatology for (a) Dec 2021–Feb 2022, (b) Mar–May 2022, (c) Jun–Aug 2022, and (d) Sep–Nov 2022. Values are stippled where they are not significantly different from zero.

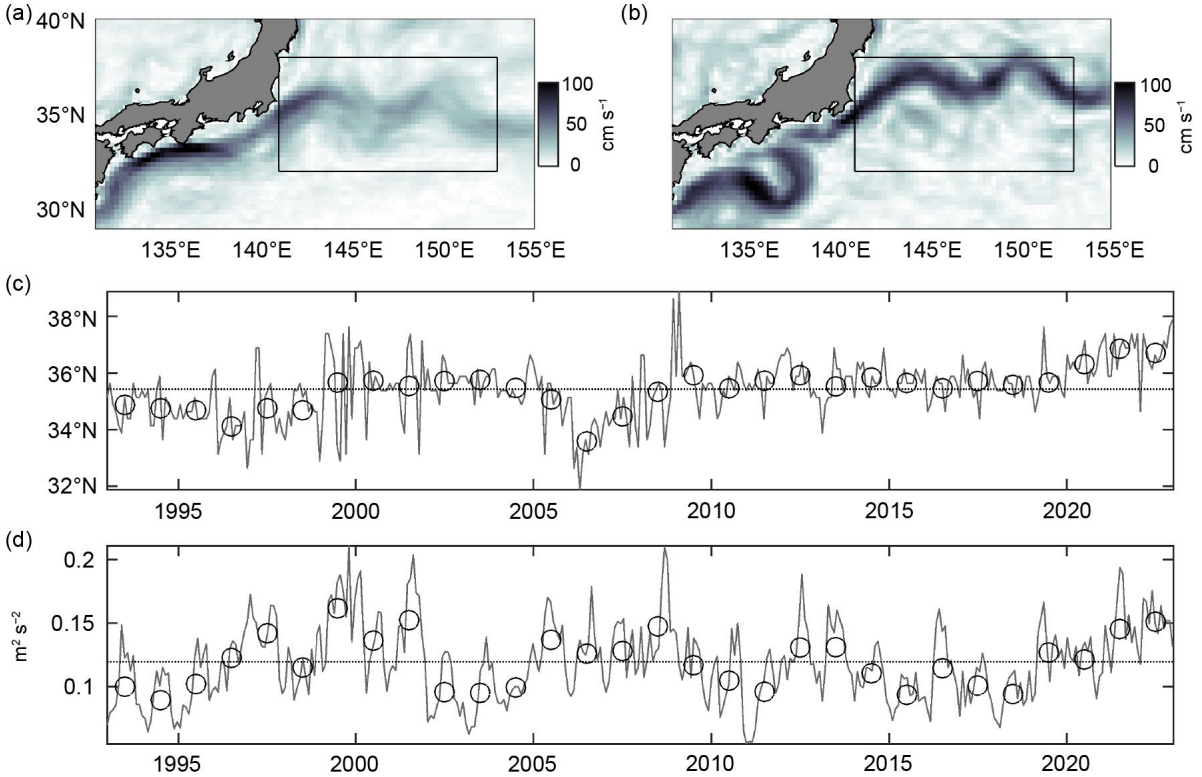

Fig. 3.20. (a) Climatological geostrophic surface current speed (cm s^{-1}) from Mulet et al. (2021) in the Kuroshio Current region (box) and surrounding regions. (b) 2022 mean geostrophic currents (cm s^{-1}) after Mulet et al. (2021) and Copernicus near-real-time altimetry. (c) Latitude of maximum zonal currents (U) averaged in the Kuroshio Current region. (d) Mean eddy kinetic energy (EKE; $m^2 s^{-2}$) in the Kuroshio Current region. Annual means are indicated by circles and overall time means by the dashed lines in (c) and (d).

decadal shifts between increased/decreased EKE and a southward/northward shift of the Kuroshio Extension because of the influence of a Kuroshio meander off the southern coast of Japan (Qiu et al. 2020). This meander is clearly seen in the 2022 altimetry data (Fig. 3.20b) and has been present since 2017, the longest known persistence of a Kuroshio large meander, consistent with wind anomalies associated with positive Pacific Decadal Oscillation forcing in the subtropical western North Pacific (Qiu and Chen 2021). A long-term northward trend in the Kuroshio extension is consistent with the poleward expansion of the Hadley cell seen in coupled climate models (Yang et al. 2020).

Because the equatorial westward anomalies have persisted since 2021, the 2022-minus-2021 difference map (Fig. 3.18b) does not exhibit these anomalies, but highlights the intensification of the eastward Pacific NECC that appeared in 2022.

Equatorial zonal current anomalies were close to zero in December–February (Fig. 3.19a), with weak (5 cm s^{-1}–6 cm s^{-1}) eastward anomalies at 1°S–3°S in the central and eastern basin consistent with a weakening of the westward South Equatorial Current (SEC). Eastward anomalies of ~10 cm s^{-1} at 8°N–9°N indicated a strengthening and northward shift of the NECC at the beginning of the year. By March–May (Fig. 3.19b) the NECC intensified, with eastward anomalies of 15 cm s^{-1}–20 cm s^{-1} at 5°N–7°N in the eastern half of the basin. Westward anomalies of 10 cm s^{-1} also developed at 0°–2°N across the Pacific and strengthened to ~25 cm s^{-1} in June–August at 140°E–175°W (Fig. 3.19c), where climatological equatorial currents are eastward at 4 cm s^{-1} to 5 cm s^{-1}. The NECC intensification persisted through these months. In September–November (Fig. 3.19d), both anomaly patterns weakened, with equatorial anomalies near zero in the central basin and exceeding 20 cm s^{-1} only in the eastern basin (~150°E–175°E) and a narrow band of 10 cm s^{-1}–18 cm s^{-1} eastward anomalies at 0°–4°N, 105°W–130°W.

2. INDIAN OCEAN

Annually averaged zonal currents in the Indian Ocean were close to their 1993–2020 climatological averages, with weak (1 cm s^{-1}–3 cm s^{-1}) eastward anomalies at 1°S–9°S across most of the basin (Fig. 3.18a). Because eastward anomalies in this latitude range were slightly stronger in 2021, the 2022-minus-2021 difference map (Fig. 3.18b) exhibits weak negative (westward) anomalies of ~–5 cm s^{-1} across the basin. Relatively strong (15 cm s^{-1}–20 cm s^{-1}) negative/positive anomalies immediately offshore Somalia indicate an anomalous southward contraction of the Great Whirl, a circulation feature most prominent in June–August during the Southwest Monsoon (Beal et al. 2013). The eastward currents at the northern edge of the Whirl have a climatological annual mean of ~42 cm s^{-1} at 10°N, but shifted to 8.5°N–9°N and weakened to 33 cm s^{-1} in 2022. These anomalies were not present in December–May (Figs. 3.19a,b); they appeared in June–August (Fig. 3.19c) and strengthened to ±30 cm s^{-1}–40 cm s^{-1} in September–November (Fig. 3.19d).

3. ATLANTIC OCEAN

Annual mean zonal currents in the western tropical Atlantic Ocean in 2022 exhibited eastward anomalies of 10 cm s^{-1} at 7°N–8°N and westward anomalies of 5 cm s^{-1}–10 cm s^{-1} at 2°N–5°N, consistent with a 5 cm s^{-1} strengthening and ~0.75° northward shift of the eastward Atlantic NECC and an ~8 cm s^{-1} strengthening of the westward northern core of the SEC (see Lumpkin and Garzoli 2005). These changes are consistent with the change in wind stress from 2021 to 2022 associated with the end of the 2021 Atlantic Niño (see Fig. 3.13b) and may have played a role in the evolution of strong fresh anomalies in the western tropical Atlantic seen in Fig. 3.8. The 2022-minus-2021 map (Fig. 3.18b) contains stronger (–10 cm s^{-1} to –20 cm s^{-1}) differences along the equator, reflecting the strong eastward currents in 2021 associated with the exceptionally strong 2021 Atlantic Niño (Crespo et al. 2022). The 2022 NECC anomalies were present at ~10 cm s^{-1} in December–February (Fig. 3.19a) and weakened significantly (to ~5 cm s^{-1}) in March–August (Figs. 3.19b,c). In September–November the eastward NECC anomalies reappeared, reaching 20 cm

s^{-1} at 7°N, along with the first appearance of the westward SEC anomalies of >10 cm s^{-1}, peaking at 4°N off the east coast of Brazil.

The variability of key Atlantic Ocean currents is continuously monitored in near realtime using a combination of in situ and satellite altimetry (https://www.aoml.noaa.gov/phod/altimetry/cvar). In the South Atlantic, the number of rings shed by the Agulhas Current remained similar to the average annual number of shedding events during the 1993–2021 record. The annual transport of the Agulhas Current, an indicator of Indian-Atlantic Ocean interbasin water exchange, was 50.8 Sv (1 Sv=10^6 m^3 s^{-1}) in a cross section at ~28°E and between 34°S and 40°S, and during the last five years has remained within 1 standard deviation of the long-term mean of 50.9±2.8 Sv. In the southwestern Atlantic, the location of the Brazil-Malvinas Confluence has demonstrated a southward trend since 1993 at decadal time scales (Lumpkin and Garzoli 2011; Goni et al. 2011). During 2022, the Confluence was located at 37.4°S, slightly to the north of the long- term mean of 37.76±0.61°S and a northward shift of 1.2°S compared to 2021 (see https://www.aoml.noaa.gov/phod/altimetry/cvar/mal/BM_ts.php). In the North Atlantic, the North Brazil Current (NBC) and associated rings serve as interhemispheric conduits for water masses and heat from the South Atlantic into the North Atlantic (Goni and Johns 2003). A portion of these waters enter the Caribbean Sea carrying low-salinity Amazon River waters (Ffield 2007), known for creating barrier layer conditions that are often associated with hurricane intensification (e.g., Balaguru et al. 2012; Domingues et al. 2015).

During 2022, freshwater contributions from the Amazon and Orinoco River systems covered most of the eastern and central Caribbean Sea for most of the year, creating negative sea-surface salinity anomalies (Fig. 3.7a) perhaps related to the record Amazon basin flood of mid-2021 (Espinoza et al. 2022). The northwestward flow of the NBC in 2022 was 7.8 Sv, similar to its long-term mean of 7.10±0.76 Sv. However, the retroflected flow increased by more than 2 standard deviations from the long-term mean of 14.9±1.8 Sv, the largest observed annual mean retroflected transport. This is consistent with the increased 2022 NECC strength as the NECC is fed by this retroflection. To the north, the Yucatan Current (YC) and Florida Current (FC) exhibited anomalies of +0.29 Sv and –1.6 Sv, respectively, compared to their 1993–2021 means of 27.76±0.90 Sv and 31.0±1.2 Sv. The YC transport was 1.43 Sv above its 2021 annual average while the FC transport decreased 1.1 Sv, with 2022 exhibiting the lowest FC annual average transport since 2000 (Fig. 3.22b). The lower-than-usual FC transport is tied to higher coastal sea level and "sunny day" flooding events along the southeast coast of the United States (Ezer and Atkinson 2014; Domingues et al. 2016; Volkov et al. 2020). Further studies addressing the delayed NBC to FC connection may help develop early warnings for such flooding events.

h. Meridional overturning circulation and heat transport in the Atlantic Ocean

—D. L. Volkov, D. A. Smeed, M. Lankhorst, S. Dong, B. I. Moat, J. Willis, W. Hobbs, T. Biló, W. Johns, and L. Chomiak

The Atlantic meridional overturning circulation (MOC) and heat transport (MHT) have been observed (Fig. 3.21) at several trans-basin and western boundary moored arrays (e.g., Frajka-Williams et al. 2019; Berx et al. 2021; Hummels et al. 2022), as well as by synthesizing in situ and satellite altimetry measurements at several latitudes (Hobbs and Willis 2012; Sanchez-Franks et al. 2021; Dong et al. 2021; Kersalé et al. 2021). Here we provide updates on the MOC and MHT estimates from the Rapid Climate Change/MOC and Heatflux Array/Western Boundary Time Series (RAPID-MOCHA-WBTS) moored array at 26.5°N and from the synthetic approach at 41°N and at several latitudes in the South Atlantic. While updates for the Overturning in the Subpolar North Atlantic Program and the South Atlantic MOC Basin-wide Array at 34.5°S are pending, we report on recent advances in observing the variability of flows comprising the lower limb of the North Atlantic MOC, including the Meridional Overturning Variability Experiment (MOVE, 16°N).

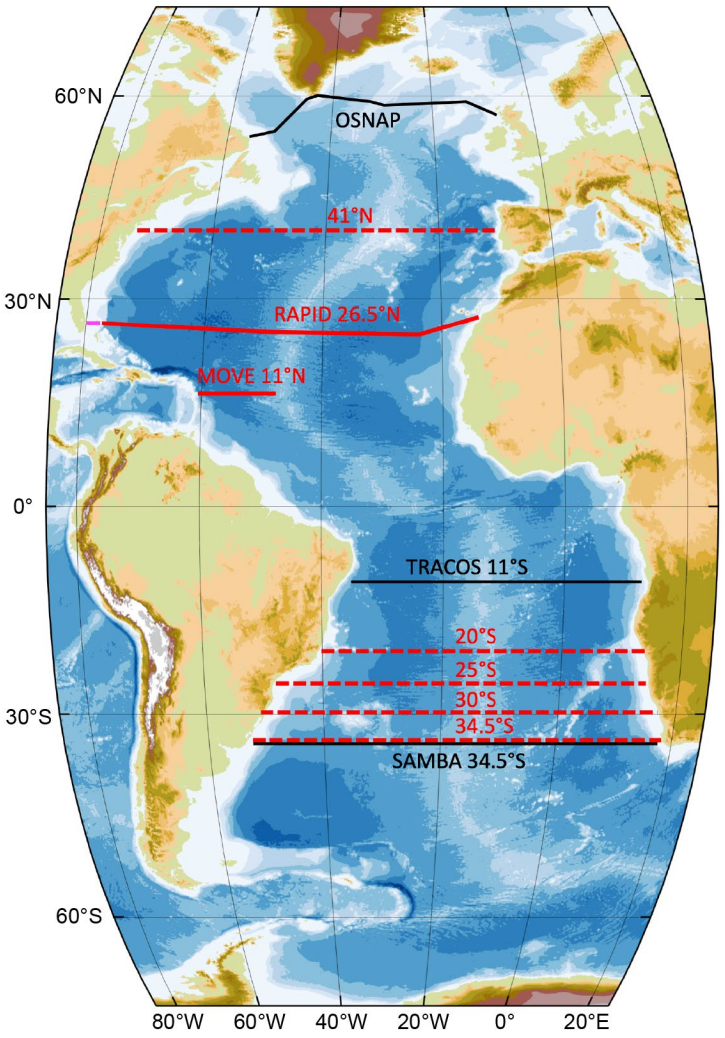

Fig. 3.21. (a) The Atlantic meridional overturning circulation (AMOC) observing system: moored arrays (solid red and black lines) and sections across which the MOC and meridional heat transport are estimated by synthesizing in situ measurements (Argo, XBT) with satellite altimetry data (dashed red lines). The red lines show the sections that have updates covered in this report, while the black lines show the sections for which updates are pending.

The RAPID moored array has provided MOC and MHT estimates at 26.5°N since April 2004 (Moat et al. 2020; Johns et al. 2011). The upper-limb (northward) MOC transport at 26.5°N is represented as the sum of 1) the Florida Current transport obtained by submarine cable measurements between Florida and the Bahamas, 2) the upper-midocean transport east of the Bahamas and above the streamfunction maximum at 1100 m, and 3) the near-surface meridional Ekman transport estimated using European Centre for Medium-Range Weather Forecasts Reanalysis version 5 zonal wind stress (e.g., McCarthy et al. 2015). The MOC and MHT time series for RAPID were recently extended to 20 December 2020 (Moat et al. 2022; Fig. 3.22). The annual mean MOC in 2020 was 17.0 Sv, close to the 2004–20 mean value of 16.9 Sv, but significantly stronger than 15.2 Sv in 2019, given the ±0.9 Sv uncertainty of annual transport estimates (McCarthy et al. 2015). The 2019 annual mean MOC was as low as in 2012; only 2009 and 2010 had lower annual means (14.6 and 14.9 Sv). The low 2019 value was mainly due to a reduction of the transport through the Florida Strait (Fig. 3.22b). This is in contrast with the previous lows, which were caused by changes in the Ekman and upper midocean transports (Figs. 3.22c,d). It has been reported that interannual variability of the MOC transport at 26.5°N is primarily due to isopycnal displacements on the western boundary, reflected in the upper-midocean transport changes (Frajka-Williams et al. 2016). However, since

about 2014, interannual variability of the MOC has been dominated by variations of the Florida Current transport (Figs. 3.22a,b; Dong et al. 2022). The reasons for this change are still unknown.

Synthetic MOC and MHT time series are evaluated at several latitudes in both the North and the South Atlantic (Fig. 3.23). Monthly estimates at 41°N (Fig. 3.23a), based on satellite altimetry and Argo measurements, were reproduced from Willis (2010) and Hobbs and Willis (2012) and extended through October 2022. Each individual estimate represents a three-month average with an uncertainty of ±2.3 Sv for the MOC and ±0.23 PW for the MHT. The mean MOC and MHT are 12.0 Sv and 0.44 PW, respectively. The MOC transport at 41°N was 13.2 Sv in January–October 2022 and 10.6 Sv in 2021, with both values not statistically different from the mean within uncertainty. The MHT in 2022 was 0.57 PW, statistically significantly greater than the time mean and the MHT of 0.39 PW in 2021. As the quality control of Argo and altimeter data is always ongoing, improvements in the estimate implemented since the *State of the Climate in 2021* report (Volkov et al. 2022) resulted in a small increase in the MOC transport equivalent to about 1 Sv from about 2019. While this change is smaller than the year-to-year uncertainty in the estimate at 41°N, it does reduce the small negative trend in the MOC since the record began in 2002, as reported last year (Volkov et al. 2022). Hence no significant trend exists in the MOC and MHT at 41°N over the past two decades.

In the South Atlantic, synthetic MOC and MHT estimates are routinely produced for 20°S, 25°S, 30°S, and 35°S (Figs. 3.23b–e) using a suite of hydrographic data (Argo, Expendable

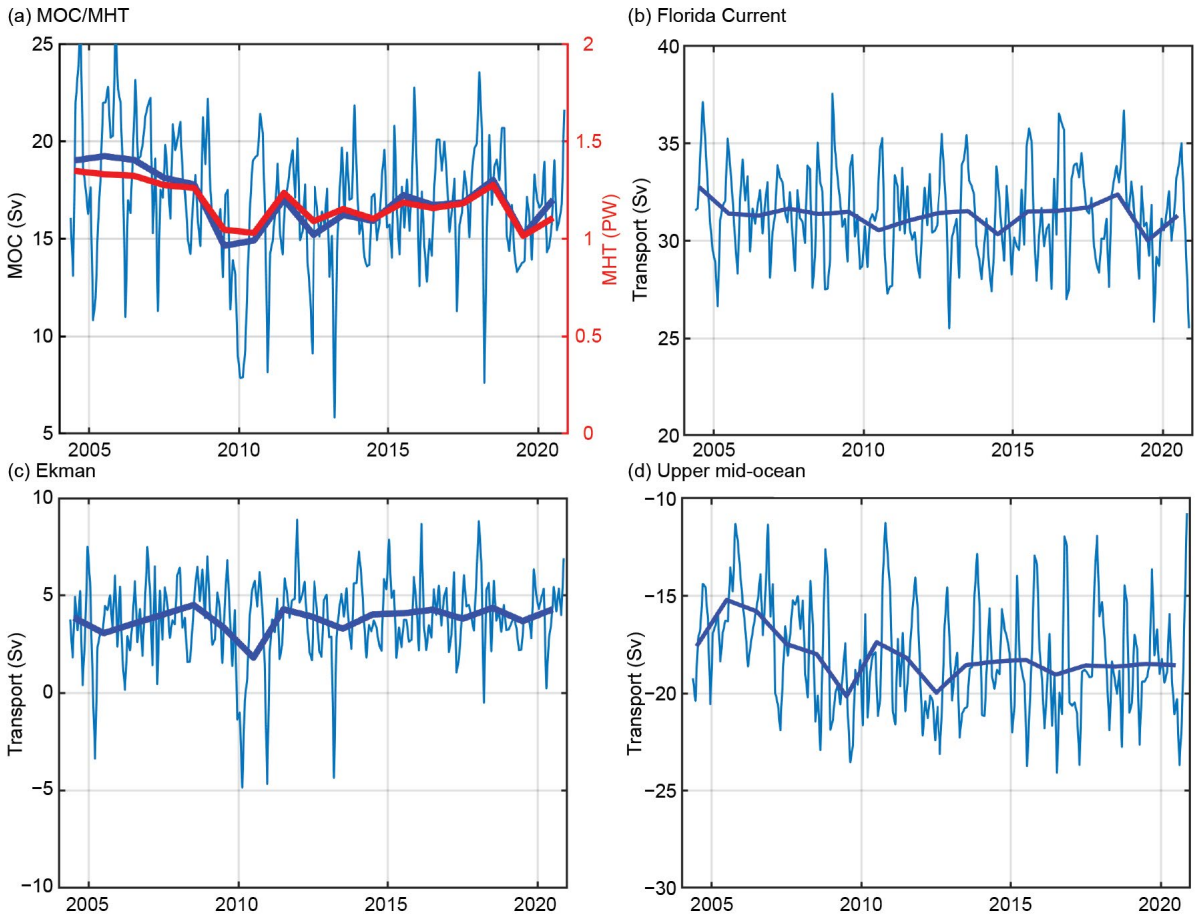

Fig. 3.22. The monthly (thin blue lines) and annual (thick lines) averages of the Atlantic meridional overturning circulation (MOC; Sv) and its components at 26.5°N: (a) the upper-limb (blue) MOC and (red) meridional heat transport (MHT; PW), (b) the Florida Current transport (Sv), (c) the near-surface Ekman transport (Sv), (d) the upper mid-ocean transport (between the Bahamas and Africa and above 1100 m; Sv). Positive/negative values mean northward/southward transports.

Bathythermographs [XBT], and Conductivity-Temperature-Depth [CTD]) and satellite altimetry (Dong et al. 2021). In 2022, the MOC and MHT estimates at 20°S, 25°S, and 30°S (16.2, 19.8, and 18.3 Sv) were nearly the same as those in 2021 (16.1, 19.5, and 18.8 Sv). At 34.5°S, both the MOC and MHT in 2022 (18.7 Sv and 0.62 PW) were lower than in 2021 by 1.1 Sv and 0.10 PW, respectively, but these differences are not statistically significant. The long-term trends in the MOC and MHT remain the same as those reported in Volkov et al. (2022). Meaningful positive trends in both the MOC and the MHT are observed at 25°S and 34.5°S only. While the MOC shows significant negative trends at 20°S and 30°S (both -0.03 ± 0.02 Sv yr^{-1}), the corresponding trends in the MHT are statistically insignificant. These trends in the MOC and MHT are mostly dominated by the geostrophic component.

In the North Atlantic, the MOC lower limb is dominated by southward flow of North Atlantic Deep Water (NADW) formed in the subpolar North Atlantic. The sum of the upper (1100 m–3000 m) and lower (3000 m–5000 m) NADW transports at 26.5N° (Fig. 3.24a), with a time-mean of –17.8 Sv, compensates for the northward transport in the MOC upper limb (Fig. 3.22a) and about 1 Sv of northward flowing Antarctic Bottom Water. The majority of the southward NADW transport is carried within the Deep Western Boundary Current (DWBC) along the eastern continental margins of the Americas. The DWBC transport measured by current meter-equipped moorings at the western end of the RAPID array since 2004 shows a time mean of –31.0±1.0 Sv, a standard deviation of about 19 Sv (for 12-hourly data), and a statistically insignificant weakening trend of 0.27 Sv yr^{-1} (Fig. 3.24a; adapted from Biló and Johns 2020). Because the moorings observe the fixed region where the DWBC's velocity core is typically found, the strong oscillations of the transport and the absence of correlation between the DWBC transport and the zonally integrated NADW flow are mainly due to the DWBC's vigorous meandering activity at time scales ranging from several weeks to a few years. Because of this strong variability, a longer time series is required to determine if the weakening trend in the DWBC transport is robust.

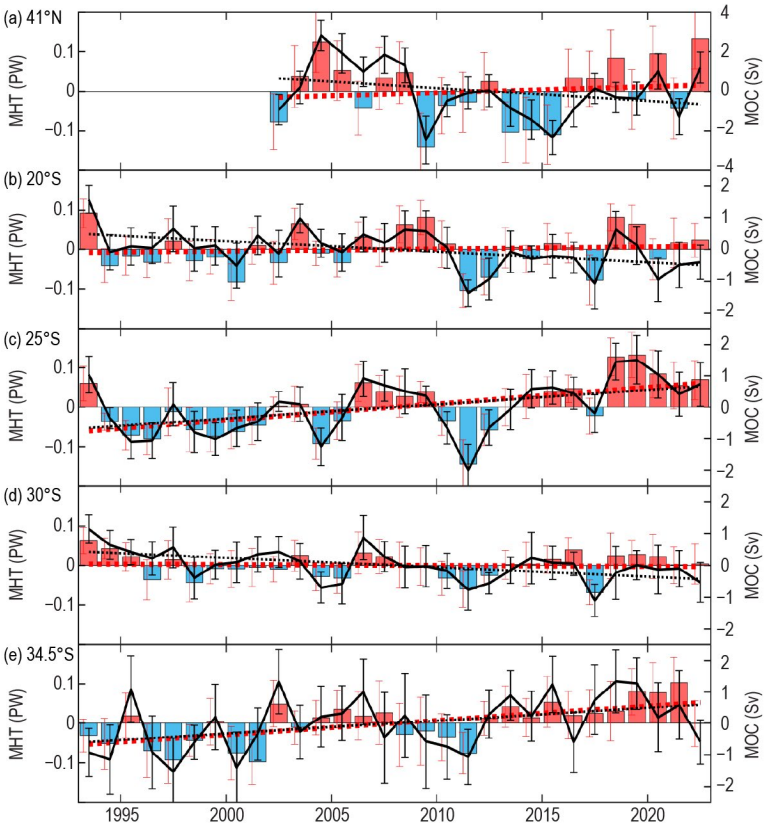

Fig. 3.23. Meridional heat transport (MHT; PW, colored bars) and the meridional overturning circulation (MOC; Sv, black curves) anomalies with respect to the record means obtained by combining satellite altimetry and in situ data at (a) 41°N, (b) 20°S, (c) 25°S, (d) 30°S, and (e) 34.5°S. The vertical error bars show standard errors (red) for MHT and (black) for MOC. The record-mean MHT and MOC values are: 0.44 PW and 12.0 Sv at 41°N, 0.62 PW and 16.6 Sv at 20°S, 0.66 PW and 19.1 Sv at 25°S, 0.62 PW and 18.9 Sv at 30°S, 0.62 PW and 19.3 Sv at 34.5°S.

Farther south, the MOVE array in the western tropical North Atlantic (Fig. 3.21) has been observing the NADW flow at 16°N since 2000 (Kanzow et al. 2006). Salinity data were reprocessed in 2022, which somewhat altered the MOVE time series (Fig. 3.24b). The time series shows a relatively strong southward flow of 17 Sv–18 Sv in the early 2000s, which weakened to about 15 Sv in 2005 and 2012 and increased again to near 18 Sv in 2019. The observed MOVE transport tendencies are consistent with those obtained from satellite gravimetry (Koelling et al. 2020). There is some consistency between the decadal changes of the southward flow at 16°N and

26.5°N, namely the overall weakening in the 2000s and strengthening in the 2010s (Figs. 3.24a,b). Recent model results have also demonstrated agreement between the centennial trends at the RAPID and MOVE sites (Danabasoglu et al. 2021), which suggest that the consistency between the two observational estimates may improve as the time series become longer.

Meridional coherence of NADW is expected due to the export of subpolar-originated deep waters to lower latitudes. Although a proper assessment of the lower NADW southward spreading patterns is still lacking, several studies have traced the advection of the upper NADW's primary component—Labrador Sea Water (LSW; e.g., van Sebille et al. 2011; Le Bras et al. 2017; Chomiak et al. 2022). Chomiak et al. (2022) investigated the advective spread of two unique LSW classes formed in 1987–94 ($LSW_{1987\text{-}94}$) and in 2000–03 ($LSW_{2000\text{-}03}$), from the Labrador Sea to 26.5°N via hydrographic arrays transecting the DWBC. The deeper and denser $LSW_{1987\text{-}94}$ class took approximately 10 years to reach the subtropics, while the lighter and shallower $LSW_{2000\text{-}03}$ class took 10–15 years. Both LSW classes were also observed to arrive within the Atlantic interior prior to or at the same time as observed farther south along the DWBC. This result, along with other recent studies (e.g., Bower et al. 2019; Biló and Johns 2019; Koelling et al. 2020; Lozier et al. 2022), suggests the importance of interior advective pathways, which have the potential to delay the communication of subpolar water masses to the subtropics.

In conclusion, multi-year monitoring of the MOC has greatly advanced our knowledge of large-scale ocean circulation variability at various timescales. With the existing MOC observing system, we are just starting to detect decadal-scale signals relevant for climate variability. While some climate models project a decline in the MOC toward the end of the twenty-first century in response to anthropogenic forcing (e.g., Cheng et al. 2013; Schleussner et al. 2014), it cannot yet be supported by the relatively short observational records. Continued MOC observations are thus necessary for detecting and mechanistic understanding of climate-related changes.

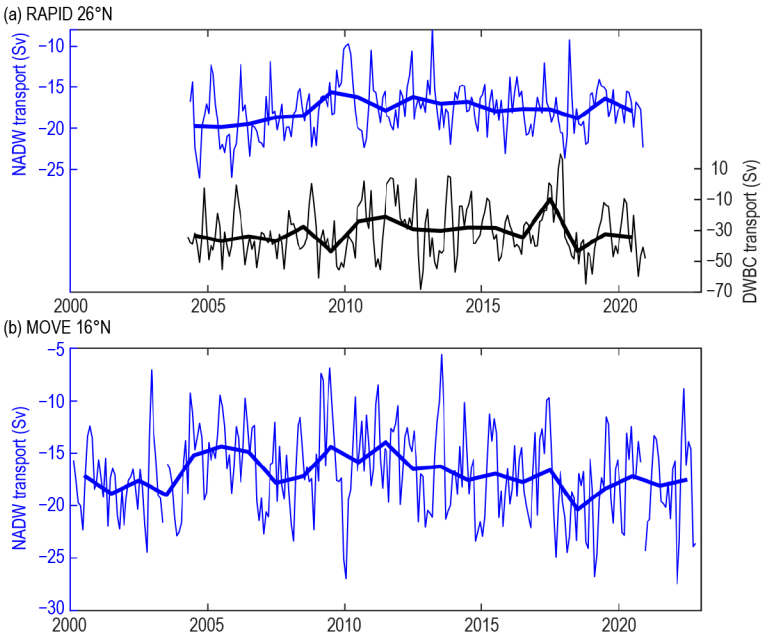

Fig. 3.24. Monthly (thin lines) and yearly (thick lines) transports (Sv) of (a) North Atlantic Deep Water (NADW) between 1100 m and 5000 m (blue) and Deep Western Boundary Current (DWBC) at 26.5°N (black; RAPID array), and (b) NADW at 16°N (MOVE array).

i. Global ocean phytoplankton

—B. A. Franz, I. Cetinić, M. Gao, D. A. Siegel, and T. K. Westberry

Marine phytoplankton contribute ~50% of global net primary production, serving the energy needs of oceanic ecosystems and providing a critical pathway for carbon sequestration to the deep oceans (Field et al. 1998; Siegel et al. 2023). The diversity, abundance, and spatio-temporal distribution of phytoplankton are controlled by biotic factors such as zooplankton grazing and viruses, as well as abiotic factors such as nutrient and light availability that are highly dependent on physical properties and processes, including ocean temperature, stratification, and circulation (e.g., Behrenfeld et al. 2006). Spaceborne ocean color radiometers such as the Sea-Viewing Wide Field-of-View Sensor (SeaWiFS; McClain 2009) and Moderate Resolution Imaging Spectroradiometer (MODIS; Esaias et al. 1998) provide a synoptic view of spatial and temporal changes in phytoplankton through measurements of near-surface concentrations of phytoplankton pigment chlorophyll-*a* (Chl*a*; mg m^{-3}) and phytoplankton carbon (C_{phy}; mg m^{-3}).

Measurements of Chl*a* contain information pertaining to both biomass and phytoplankton physiology, while C_{phy} measures phytoplankton carbon biomass. C_{phy} and Chl*a* often covary, but discrepancies in their distributions are indicative of changes in the physiological or compositional characteristics of phytoplankton communities (Dierssen 2010; Geider et al. 1997; Siegel et al. 2013; Westberry et al. 2016).

In this report, we evaluate the global distribution of phytoplankton over the period October 2021–September 2022 (the analysis year) using remotely sensed Chl*a* and C_{phy} measurements from the continuous 25-year record that combine observations of SeaWiFS (1997–2010) and MODIS on *Aqua* (MODIS-A, 2002–present). The MODIS-A daytime sea-surface temperature (SST; °C) is also assessed over a consistent time period to provide context on the physical state of the oceans. A key difference in the data sources between this report and previous reports (e.g., Franz et al. 2022) is that the ocean color data from MODIS-A and SeaWiFS were reprocessed by NASA from version R2018.0 to version R2022.0. This reprocessing had only minor impact to the observed trends in the two missions, as temporal calibration updates were minimal, but it did introduce small bias changes in the derived phytoplankton indices. As in R2018.0, the Chl*a* product was derived using the Ocean Color Index algorithm of Hu et al. (2012) but with updated algorithm coefficients applied in R2022.0 (Hu et al. 2019; O'Reilly and Werdell 2019). C_{phy} was derived from the particle backscattering coefficient, b_{bp}, at 443 nm (Generalized Inherent Optical Properties [GIOP] algorithm; Werdell et al. 2013) and a linear relationship between b_{bp} and C_{phy} (Graff et al. 2015). The GIOP algorithm was also updated for the R2022.0 reprocessing to include correction for Raman scattering (McKinna et al. 2016). In merging the time series of SeaWiFS and MODIS-A, differences between the sensors were assessed over the overlapping period from 2003 through 2008, and a bias correction (−0.0021 mg m^{-3} in Chl*a* and −6.7e-5 m^{-1} in b_{bp} or −0.78 mg m^{-3} of C_{phy}) was derived and applied to the SeaWiFS time series.

A major event likely influencing the quality of Chl*a* and C_{phy} measurements in 2022 was the eruption of Hunga Tonga–Hunga Ha'apai in January 2022 (see Sidebar 2.2). This eruption injected water vapor and sulfur dioxide into the stratosphere and resulted in a substantial increase in stratospheric sulfate aerosols that remained aloft through 2022 (Taha et al. 2022; Schoeberl et al. 2022; Zhu et al. 2022; Sellitto et al. 2022). The atmospheric correction algorithm as applied in NASA's R2022.0 reprocessing does not properly correct for the effect of light scattering and absorption by these high-altitude aerosols, and thus increased error can be expected in the retrieved spectral water-leaving reflectances from which C_{phy} and Chl*a* are derived. The Chl*a* measurements, however, are less sensitive to atmospheric correction errors due to the nature of the algorithm (Hu et al. 2012), and thus we have higher confidence in the distribution of changes observed in Chl*a*. While further research is underway to fully assess the impact and mitigation of this eruption on satellite ocean-color retrievals, the quality of phytoplankton measurements is likely impacted by this eruption, and thus our ability to interpret the results is compromised.

Given that caveat, changes in the two phytoplankton distribution metrics were evaluated by subtracting monthly climatological means for MODIS-A Chl*a* and C_{phy} (October 2002–September 2021) from their monthly mean values for the 2022 analysis year. These monthly anomalies were then averaged to produce the global Chl*a* and C_{phy} annual mean anomaly maps (Figs. 3.25a,b). Similar calculations were performed on MODIS-A SST data to produce an equivalent SST annual mean anomaly for the same time period (Fig. 3.25c). The permanently stratified ocean (PSO), used for the analysis depicted in Figs. 3.26 and 3.27, is defined as the region, spanning the tropical and subtropical oceans, where annual average SST is greater than 15°C and surface mixed layers are typically low in nutrients and shallower than the nutricline (black lines near 40°N and 40°S in Fig. 3.25; Behrenfeld et al. 2006).

For the 2022 analysis year, the distribution of SST anomalies (Fig. 3.25c) replicated patterns observed in 2021, including a pronounced tongue of anomalously cold waters across the equatorial Pacific. This feature is indicative of the prevailing La Niña conditions during 2022 (see Sidebar 3.1 and section 4b for details), as is the highly elevated (+50%) Chl*a* concentrations that follow the edges of the cold-water tongue and extend into the equatorial Pacific (Fig. 3.25a).

Patches of higher-than-usual Chl*a* were also observed along equatorial regions of the Indian Ocean (up to +50%) and throughout the North and South Atlantic. Regions with elevated Chl*a* are typically associated with negative SST anomalies. Within the PSO away from strong upwelling regions, these cooler regions generally correspond to deeper-surface mixed layers (Deser et al. 2010), resulting in reduced phytoplankton light exposure rates and thus increased cellular Chl*a* and a decoupling between Chl*a* and C_{phy} variability (Behrenfeld et al. 2015). A key feature in the C_{phy} anomalies for this year (Fig. 3.25b) is a general reduction (5%–10%) over much of the PSO in the Southern Hemisphere that is largely anticorrelated with the changes in Chl*a*, but this is likely associated in part with error in the C_{phy} measurements due to the Hunga Tonga eruption. Patches of elevated Chl*a* are visible throughout the subpolar and polar regions poleward of the PSO (Fig. 3.25a) and largely covary with C_{phy} anomalies in these well-mixed regions (Fig. 3.25b). Observed heterogeneity in biomass indicators outside of the PSO is consistent with previous reports (e.g., Franz et al. 2022) and is a result of the ephemeral nature of blooms in these regions, as well as poor spatial and temporal sampling at higher latitudes due to clouds and low-light conditions.

To provide greater insight into interannual temporal variability in phytoplankton distributions, Figs. 3.26a,b show the climatological mean seasonal cycle for Chl*a* and C_{phy} in the PSO. Superimposed on this climatology is the corresponding mean for each month of the 2022 analysis year (red circles in Fig. 3.26). Annual variability of Chl*a* and C_{phy} in the PSO typically displays two distinct peaks (Figs. 3.26a,b), reflecting the springtime increases of biomass in Northern (Figs. 3.26c,d) and Southern Hemispheres (Figs. 3.26g,h). Peaks in C_{phy} lag 2–3 months behind those of Chl*a*, reflecting a reduction in phytoplankton chlorophyll-to-carbon ratios as the seasonal bloom progresses (e.g., Westberry et al. 2016). While patterns observed this year are similar to previous years (e.g., Franz et al. 2022), observed changes over the PSO region are dominated by changes in the equatorial and Southern Hemisphere regions (Figs. 3.26e–h). The Chl*a* was elevated over nearly the entire analysis year, with the February peak exceeding all previous observations, before returning to climatological norms in September 2022. In contrast, C_{phy} showed elevated values in the last quarter of 2021 relative to climatology, but transitioned to depressed values by March of 2022 and remained below all previous measurements

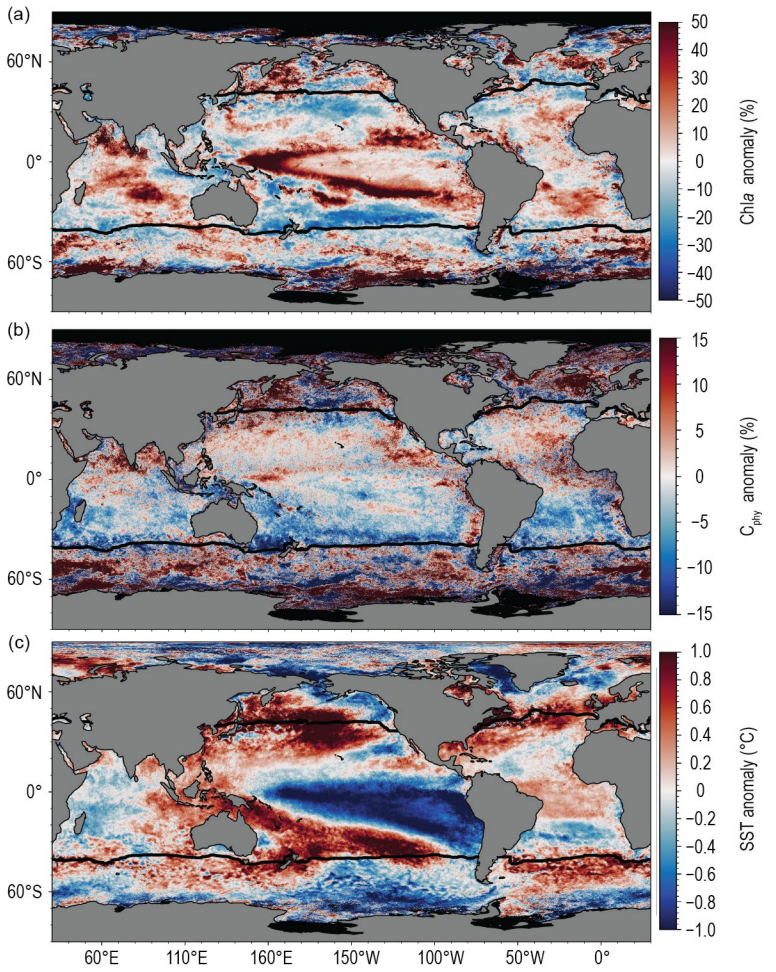

Fig. 3.25. Spatial distribution of average monthly (a) MODIS-A chlorophyll-*a* (Chl*a*) anomalies (%), (b) MODIS-A phytoplankton carbon (C_{phy}) anomalies (%), and (c) MODIS-A sea-surface temperature (SST) anomalies (°C) for Oct 2021–Sep 2022, where monthly differences were derived relative to the MODIS-A 19-year climatological record (Oct 2002–Sep 2021). Chl*a* and C_{phy} are stated as % difference from climatology, while SST is shown as an absolute difference. Also shown in each panel is the location of the mean 15°C SST isotherm (black lines) delineating the permanently stratified ocean. Differences in the SST anomalies here versus in Fig. 3.1 are owing to differences in climatological periods, smoothing, and data sources.

through September. The geographic distribution and timing of this progression in C_{phy} from elevated to depressed is consistent with the progression of stratospheric aerosols over the tropics and Southern Hemisphere from the Hunga Tonga eruption (Taha et al. 2022).

Over the 25-year time series of spatially-averaged monthly-mean Chl*a* within the PSO (Fig. 3.27a), concentrations vary by 5.8% (0.008 mg m^{-3}, standard deviation) around a long-term average of 0.136 mg m^{-3} (Fig. 3.27a). C_{phy} over the same 25-year period varies by 3.4% (0.75 mg m^{-3}) around an average of 21.8 mg m^{-3} (Fig. 3.27c). Chl*a* monthly anomalies within the PSO (Fig. 3.27b) vary by 4.7% (0.006 mg m^{-3}) over the multi-mission time series, with the largest deviations generally associated with the El Niño–Southern Oscillation (ENSO) events (r = −0.38), as demonstrated by the correspondence of Chl*a* anomaly variations with the Multivariate ENSO Index (MEI; Wolter and Timlin 1998; presented in the inverse to illustrate the covariation). C_{phy} anomalies (Fig. 3.27d), which vary by 2.2% (0.47 mg m^{-3}), are less correlated with the MEI (r = −0.16) due to the inherent lag between environmental change and growth. A major observation for

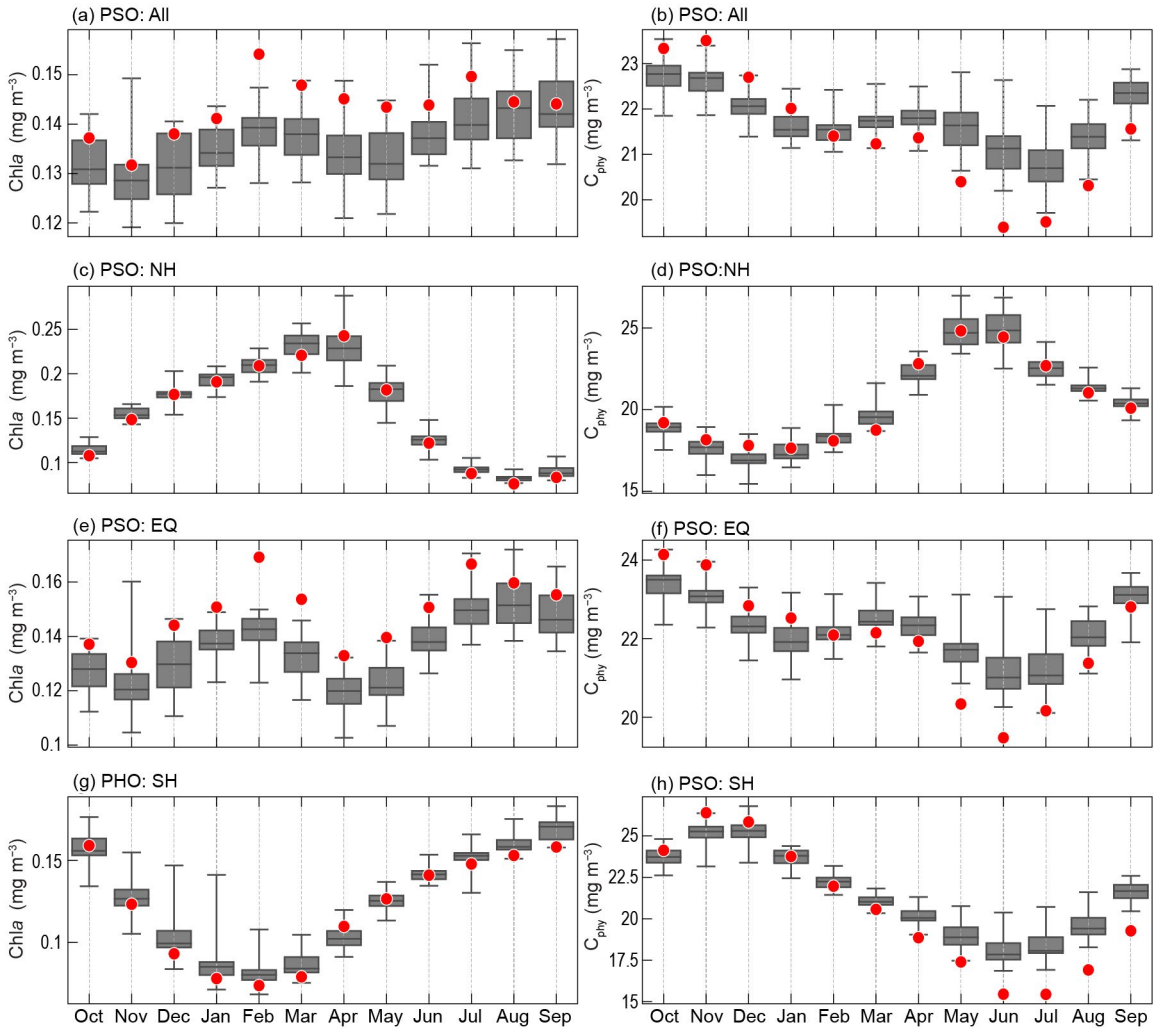

Fig. 3.26. Distribution of Oct 2021–Sep 2022 monthly means (red circles) for (a) MODIS-A chlorophyll-*a* (Chl*a*) and (b) MODIS-A phytoplankton carbon (C_{phy}) for the permanently stratified ocean (PSO) region (see Fig. 3.25), superimposed on the climatological values as derived from the combined time series of SeaWiFS and MODIS-A over the 24-year period of Oct 1998–Sep 2021. Gray boxes show the interquartile range of the climatology, with a black line for the median value and whiskers extending to minimum and maximum values. Subsequent panels show latitudinally segregated subsets of the (c),(d) PSO for the Northern Hemisphere (NH, north of tropics), (e),(f) tropical ±23.5°-latitude subregion (EQ), and (g),(h) Southern Hemisphere (SH, south of tropics). Units for (a), (c), (e), and (g) are Chl*a* (mg m^{-3}) and (b), (d), (f), and (h) are C_{phy} (mg m^{-3}).

2022 is that, while the Chl*a* anomaly remains elevated and consistent with expectation under prevailing La Niña conditions, the C_{phy} anomaly is depressed, with values nearly 1 mg m^{-3} below the lowest value previously observed. While this suggests a significant shift in chlorophyll-to-carbon ratios and thus a notable change in phytoplankton physiology or community composition, we cannot yet rule out the likely possibility that the changes we see in C_{phy} (and Chl*a* to a lesser extent) reflect error in the time series due to the Hunga Tonga eruption. Hence, we emphasize caution in interpretation of these observed trends until a more detailed assessment can be completed.

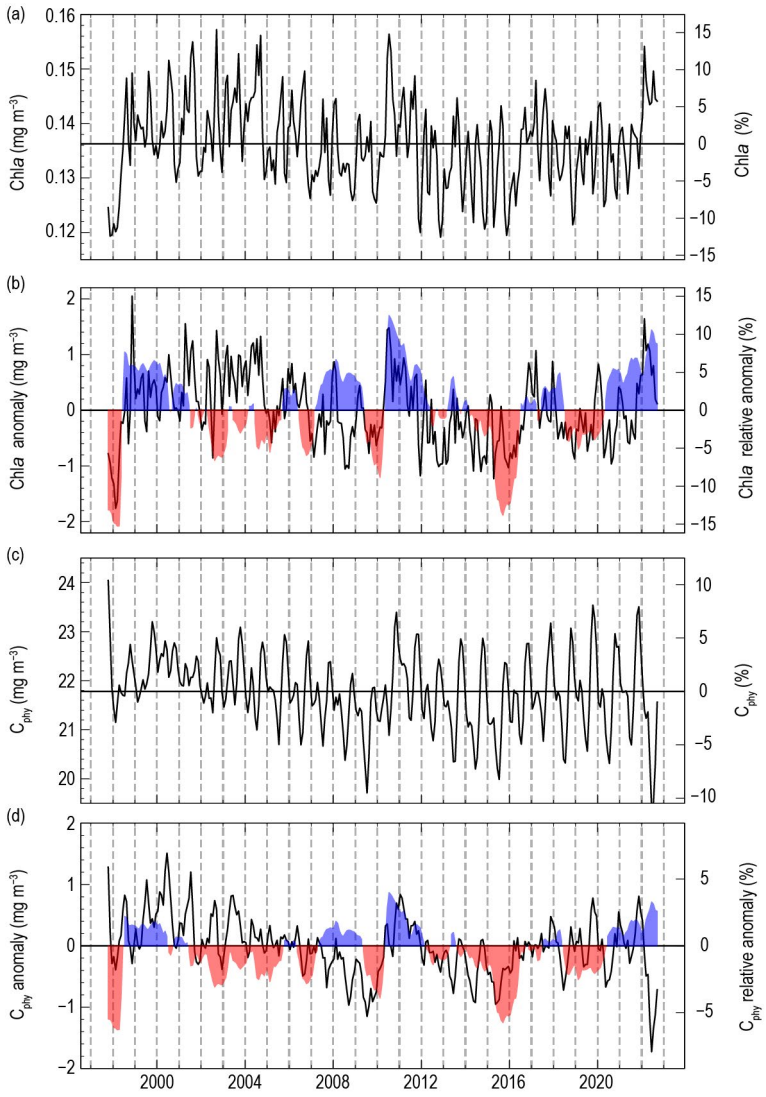

Fig. 3.27. Twenty-five-year, multi-mission record of chlorophyll-*a* (Chl*a*; mg m^{-3}) and phytoplankton carbon (C_{phy}; mg m^{-3}) averaged over the permanently stratified ocean (PSO) region. (a) Monthly Chl*a*, with the horizontal line indicating the multi-mission mean Chl*a* concentration for the entire PSO region. (b) Monthly Chl*a* anomalies after subtraction of the 24-year multi-mission monthly climatological mean (Fig. 3.26a). (c) Monthly C_{phy}, with the horizontal line indicating the multi-mission mean C_{phy} concentration for the entire PSO region. (d) Monthly C_{phy} anomalies after subtraction of the 24-year multi-mission monthly climatological mean (Fig. 3.26b). Shaded blue and red colors (b) and (d) show the Multivariate El Niño–Southern Oscillation Index, inverted and scaled to match the range of the Chl*a* and C_{phy} anomalies, where blue indicates La Niña conditions and red indicates El Niño conditions.

Sidebar 3.2: **Tracking global ocean oxygen content**
—J. SHARP

Dissolved oxygen is fundamental for meeting the physiological demands of marine organisms and for controlling elemental cycles in seawater. Multicellular aerobic marine organisms use oxygen to extract energy from organic material (Koch and Britton 2008). Consequently, the geographic distributions of suitable habitats for aerobic marine taxa are set by temperature-dependent oxygen availability (Pörtner and Knust 2007; Deutsch et al. 2015). Whereas lethal thresholds of dissolved oxygen vary between species, many marine taxa cannot tolerate an oxygen content ($[O_2]$) below about 60 µmol kg^{-1} (an approximate threshold for hypoxia) for an extended period of time (Vaquer-Sunyer and Duarte 2008; Levin et al. 2009). On an ecosystem scale, oxygen availability influences the rates and prevalence of biologically mediated processes that transform dissolved elements in seawater. For example, below dissolved $[O_2]$ concentrations of about 5 µmol kg^{-1}, denitrification becomes favored over aerobic respiration, meaning a critically important nutrient (nitrate) is removed from seawater (Gruber 2008). Further, nitrous oxide produced by incomplete denitrification in low-oxygen conditions (Babbin et al. 2015; Bourbonnais et al. 2017) can escape to the atmosphere where it acts as a potent greenhouse gas (Forster et al. 2021).

Oxygen enters the ocean via dissolution at the air–sea interface, is generated near the ocean surface by photosynthesis, is transported throughout the ocean interior by advection and diffusion, and is depleted by respiration at depth as water masses age. This interplay between physics and biology sets the general distribution of dissolved oxygen throughout the global ocean (Keeling et al. 2010; Fig. SB3.3). Since at least the middle of the twentieth century, however, the oceans have been losing oxygen on a global scale (Oschlies et al. 2017; Breitburg et al. 2018; Bindoff et al. 2019; Canadell et al. 2021). This deoxygenation is primarily caused by: 1) anthropogenic ocean warming that directly decreases the capacity of seawater for dissolved oxygen (Garcia and Gordon 1992) and 2) ocean stratification, which is caused by ocean warming and decreases the degree to which subsurface waters exchange with the atmosphere (Levin 2018; Oschlies et al. 2018). Other potential contributions to deoxygenation include changes in subsurface respiration (e.g., Oschlies et al. 2008), large-scale overturning (e.g., Talley et al. 2016), and ocean circulation (e.g., Brandt et al. 2015).

Oxygen content has historically been measured on discrete seawater samples by a chemical titration (Carpenter 1965;

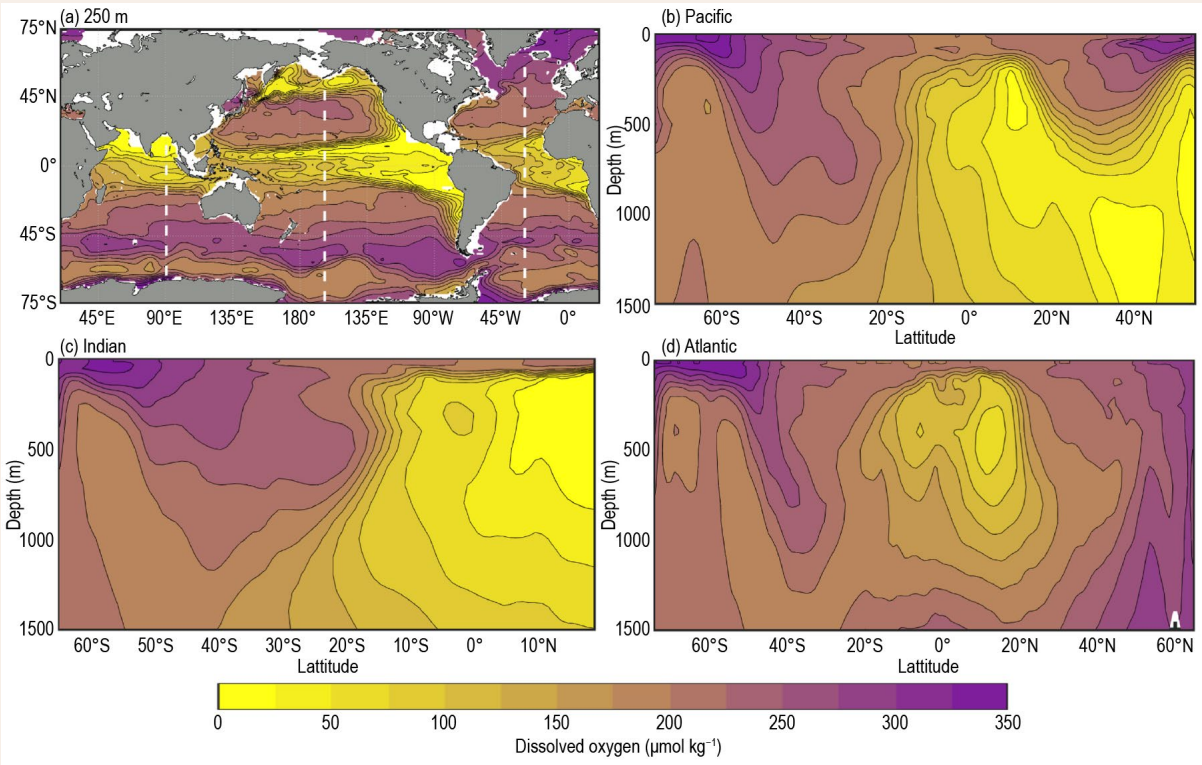

Fig. SB3.3. (a) Global distribution of dissolved oxygen content (µmol kg^{-1}) at 250-m depth, along with meridional sections in the (b) Pacific, (c) Indian, and (d) Atlantic Oceans from the surface to 1500 m. Dissolved oxygen content is from the GLODAPv2 mapped product (Lauvset et al. 2016).

Langdon 2010) first introduced by Winkler (1888). The collection of Winkler titrations performed on repeat hydrography cruises over multiple decades (Talley et al. 2016) have built up a large dataset of [O_2] measured via a consistent method, which has been quality controlled and curated into databases and visual atlases. A significant portion of the global observational [O_2] dataset is also composed of measurements from sensors on Conductivity-Temperature-Depth profilers, although some of these are less rigorously quality controlled than Winkler titration data (Boyer et al. 2018).

Over the past two decades, autonomous platforms carrying oxygen sensors have been distributed throughout the global ocean, primarily associated with the scaling up of the biogeochemical Argo program (BGC Argo; Claustre et al. 2020). BGC Argo floats carry chemical and bio-optical sensors, in addition to the temperature and salinity sensors that are implemented on all Argo floats (Roemmich et al. 2009). One of those chemical sensors is for dissolved oxygen (Gruber et al. 2010); most common are optodes that measure [O_2] by quantification of luminescence quenching by oxygen (Bittig et al. 2018). Extensive research over the past two decades has been directed toward ensuring high-quality optode-based [O_2] measurements on BGC Argo floats, including the implementation of drift corrections, establishment of calibration procedures, and recommendation of delayed-mode quality control practices (e.g., D'Asaro and McNeil 2013; Bittig and Körtzinger 2015; Bushinsky et al. 2016; Maurer et al. 2021).

Compilations of [O_2] measured by Winkler titrations have indicated that oxygen content in the upper 1000 m of the global ocean has decreased by about 2% from 1970 to 2010 (Fig. SB3.4; Helm et al. 2011; Ito et al. 2017; Schmidtko et al. 2017), with a very likely (90% confidence) range of 0.5% to 3.3% (Bindoff et al. 2019). These studies have sought to interpolate between scattered observations, average measurements across time intervals, and otherwise scale up the available observational coverage to estimate long-term oxygen trends at the global scale. Earth system models (ESMs) have also been used to evaluate global ocean deoxygenation, with estimated decreases of closer to 1% in the upper 1000 m of the ocean from 1970 to 2010 (Fig. SB3.4; Bopp et al. 2013; Kwiatkowski et al. 2020). Global and regional discrepancies between observational products and ESMs have been attributed to inadequate simulation of ocean circulation and wind-driven ventilation, poorly constrained biogeochemical processes, and the roles of equatorial jets and mixing processes in oxygen transport (Oschlies et al. 2017, 2018; Buchanan and Tagliabue 2021). Existing discrepancies, however, do appear to be getting smaller as representations of physical and biogeochemical processes in ocean models are improved (Canadell et al. 2021).

Newly emerging observational estimates of global ocean oxygen content are incorporating measurements from BGC Argo floats and other autonomous platforms. One such data product (Gridded Ocean Biogeochemistry from Artificial Intelligence-O_2 [GOBAI-O_2]; Sharp et al. 2022a) uses machine learning to fill gaps in observations, relying on relationships between [O_2] and ocean temperature, salinity, and spatio-temporal coordinates. GOBAI-O_2 shows an oxygen decline of ~0.7% decade^{-1} in the upper 1000 m of the ocean from 2004 to 2022 (–1.12 µmol kg^{-1} decade^{-1}; Sharp et al. 2022b). This is somewhat higher than the other observation-based estimates shown in Fig. SB3.4, albeit for a distinctly different time period, indicating a potential acceleration in global deoxygenation. Emerging data products like GOBAI-O_2 will offer the opportunity for researchers to investigate sub-decadal variability in global and regional oxygen content, which has not previously been feasible outside of dedicated time-series locations.

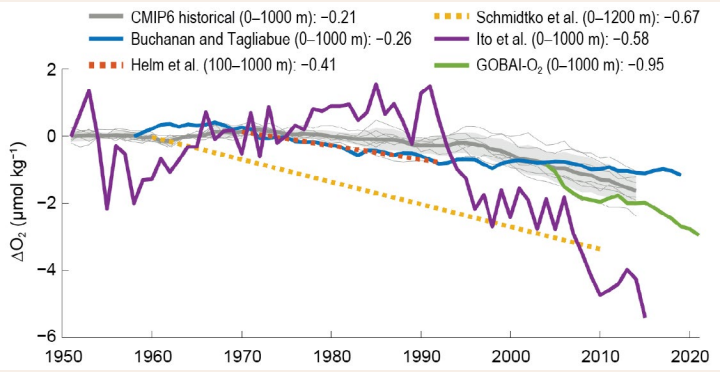

Fig. SB3.4. Estimates of global ocean deoxygenation over recent decades. Initial Δ[O_2] for each line is adjusted to the average CMIP6 value. Trends in the legend are in µmol kg^{-1} decade^{-1} over the period of time each line spans. Data for individual CMIP6 models (thin gray lines with the average given as a thick gray line), Buchanan and Tagliabue (2021), and Ito et al. (2017) are taken from the supplemental material of Buchanan and Tagliabue (2021). Straight dotted lines represent estimates taken only from reported slopes and converted to µmol kg^{-1} decade^{-1}: –0.93 µmol L^{-1} from 1970 to 1992 from Helm et al. (2011) and –257.5 Tmol decade^{-1} in a volume of 376.14 × 10^6 km^3 from Schmidtko et al. (2017). The GOBAI-O_2 estimate was calculated from the gridded product of Sharp et al. (2022a). Gray shading represents the standard deviation among individual CMIP6 models, and green shading represents uncertainty in the GOBAI-O_2 estimate, determined via a model simulation experiment described in Sharp et al. (2022b).

j. Global ocean carbon cycle

—R. Wanninkhof, J. A. Triñanes, P. Landschützer, R. A. Feely, and B. R. Carter

1. INTRODUCTION

The oceans play a major role in the global carbon cycle by taking up a significant fraction of the excess carbon dioxide that humans release into the atmosphere. As a consequence of humankind's collective carbon dioxide (CO_2) emissions into the atmosphere, referred to as anthropogenic CO_2 (C_{ant}) emissions, the atmospheric CO_2 concentration has risen from pre-industrial levels of about 278 ppm (parts per million) to 417 ppm in 2022. Marine C_{ant} is the major cause of anthropogenic ocean acidification. Over the last decade the global ocean has continued to take up C_{ant} emissions and therefore is a major mediator of global climate change. Of the 10.8 (±0.8) Pg C yr^{-1} C_{ant} released during the period 2012–21, 2.9 (±0.4) Pg C yr^{-1} (26%) accumulated in the ocean, 3.1 (±0.6) Pg C yr^{-1} (28%) accumulated on land, and 5.2 (±0.02) Pg C yr^{-1} (46%) remained in the atmosphere with an imbalance of –0.3 Pg C yr^{-1} (–3%; Table 6 in Friedlingstein et al. 2022). This decadal ocean carbon uptake estimate is a consensus view from a combination of measured decadal CO_2 inventory changes, models, and global air–sea CO_2 flux estimates based on surface ocean fugacity of CO_2 (fCO_{2w})[1] measurements from ships, uncrewed surface vehicles (USV), and moorings.

Independent decadal estimates of uptake based on interior measurements by Müller et al. (2023) show that the global ocean storage of anthropogenic carbon grew by 29±3 and 27±3 Pg C $decade^{-1}$ from 1994 to 2004 and 2004 to 2014, respectively. The fraction of anthropogenic emissions taken up by the ocean decreased from 36±4 to 27±3 % from the first to the second decade. This reduction is attributed to a decrease of the ocean buffer capacity (i.e., the consumption of carbonate and other basic chemical species with continued ocean uptake of CO_2) and changes in ocean circulation. From models and observations, Friedlingstein et al. (2022) showed that the oceanic anthropogenic carbon sink has grown from 1.1 (±0.4) Pg C yr^{-1} in the decade of the 1960s to 2.9 (±0.4) Pg C yr^{-1} in 2022.

2. AIR–SEA CARBON DIOXIDE FLUXES

Ocean uptake of CO_2 is estimated from the net air–sea CO_2 flux derived from the bulk flux formula with differences in air (a) and surface-seawater (w) CO_2 fugacity ($\Delta fCO_2 = fCO_{2w} - fCO_{2a}$) and gas transfer coefficients as input. Gas transfer is parameterized with wind as described in Wanninkhof (2014). This provides a net flux estimate. A steady contribution of carbon from riverine runoff, with estimates ranging from 0.45 to 0.78 Pg C yr^{-1} (Resplandy et al. 2018) needs to be included to obtain the C_{ant} estimate. Here, 0.65 Pg C yr^{-1} is used as the river adjustment as recommended in the Global Carbon Budget 2022 (Friedlingstein et al. 2022). The data sources for fCO_{2w} are annual updates of observations from the Surface Ocean CO_2 Atlas (SOCAT) composed of moorings, USV, and ship-based observations (Bakker et al. 2016), with SOCAT version 2022 containing 33.7 million datapoints through 2021 (https://www.socat.info/wp-content/uploads/2022/06/2022_Poster_SOCATv2022_release.pdf). The increased observations and improved mapping techniques, including machine learning methods summarized in Rödenbeck et al. (2015), now provide annual global fCO_{2w} fields on a 1° latitude × 1° longitude grid at monthly time scales. This allows investigation of variability on sub-annual to decadal time scales.

The monthly 2022 ΔfCO_2 maps are based on a self-organizing maps feed-forward neural network (SOM-FNN) approach of Landschützer et al. (2013, 2014). The 2022 maps use sea-surface temperature (SST), Chlorophyll-*a*, atmospheric CO_2, mixed-layer depth, and salinity (NOAA IOSSTv2 [Huang et al. 2021a]; Globcolour Chlorophyll-*a* [Maritorena et al. 2010]; NOAA MBL atmospheric CO_2 [Dlugokencky et al. 2021]; DeBoyer Mixed layer depth climatology [de Boyer Montégut et al. 2004] and Hadley center EN4 salinity [Good et al, 2013]) as predictor variables. The fluxes are determined using European Centre for Medium-Range Weather Forecasts

[1] The fugacity is the partial pressure of CO2 (pCO2) corrected for non-ideality. They are numerically similar for surface waters with fCO2≈0.994 pCO2.

Reanalysis version 5 (ERA5) winds (Hersbach et al. 2018). For 2022 flux calculations, the final ERA5 winds from January through August and their early release (ERA5T) winds from September through December are used.

The SOM FNN results (Fig. 3.28) show a slightly increasing ocean sink from 1982 to 1994, followed by a period of rapidly decreasing uptake from 1995 to 2002. There is a strong increase in the ocean sink from 2002 onward that continues through 2016. The amplitude of seasonal variability is ≈1.2 Pg C with a minimum uptake in the June–September timeframe. Variability in seasonal amplitudes does not correlate with annual uptake or its variability. The C_{ant} flux of 3.3 Pg C yr^{-1} for 2022 (green line in Fig. 3.28) was 23% above the 1990–2020 average of 2.68 (±0.52) Pg C yr^{-1}.

The annual average flux map for 2022 (Fig. 3.29a) shows the characteristic pattern of effluxes (ocean-to-air CO_2 fluxes) in tropical, coastal upwelling, and open-ocean upwelling regions. Coastal upwelling regions include those in the Arabian Sea and off the west coasts of North and South America. The western Bering Sea in the northwest Pacific was a strong CO_2 source as well in 2022; a clear juxtaposition to the strong sink in the surrounding regions. The region with the largest efflux was the upwelling region of the eastern and central equatorial Pacific. Cumulatively, the regions of effluxes are significant CO_2 sources to the atmosphere (≈ 1 Pg C). The primary CO_2 uptake regions are in the subtropical and subpolar regions. The largest sinks are poleward of the sub-tropical fronts. In the Southern Ocean, the area near the polar front (~60°S) is nearly neutral with the polar frontal region in the eastern South Pacific being a source in 2022.

In the Northern Hemisphere, the entire North Atlantic is a large sink while in the North Pacific the sink region is punctuated by a significant source of CO_2 in the western to central Bering Sea. This pattern is, in part, due to the position of the western boundary currents whose cooling waters contribute to CO_2 sinks at high latitudes. In particular, the Gulf Stream/North Atlantic Drift in the Atlantic extends farther north than the Kuroshio in the Pacific.

The ocean carbon uptake anomalies (Fig. 3.29c) in 2022 relative to the 1990–2020 average are attributed to the increasing ocean CO_2 uptake with time due to atmospheric CO_2 increases yielding a 0.6 Pg C greater annual uptake than the 30-year average (Fig. 3.28). Therefore, the anomalies are largely negative. However, large regions show positive anomalies due to variations in large-scale climate modes, particularly the El Niño–Southern Oscillation. Large positive anomalies are seen in the central equatorial Pacific, particularly in large areas in the sub-tropical regions from 20°N to 40°N in the eastern North Pacific and North Atlantic, and 20°S to 40°S in the western Pacific. The increased effluxes in the central equatorial Pacific are related to La Niña conditions that have persisted almost uninterrupted since August 2020 (see Sidebar 3.1 and section 4b for details). The negative sea-surface temperature anomaly (SSTA) there (see Fig. 3.1a) indicates that increased upwelling of cold waters with high CO_2 content in the central Pacific returned after a period of lower-than-normal upwelling prior

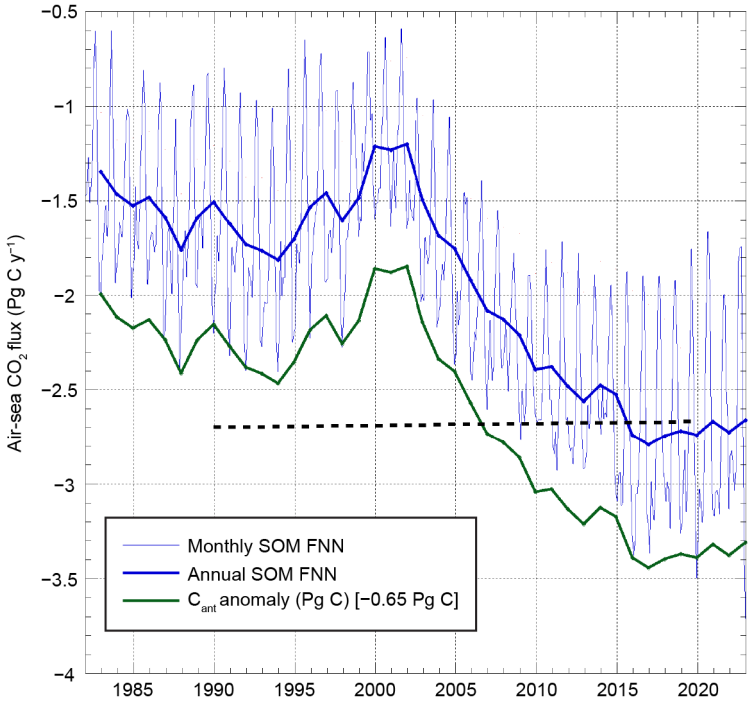

Fig. 3.28. Global annual (thick blue line) and monthly (thin blue line) net carbon dioxide (CO_2) fluxes (Pg C yr^{-1}) for 1982–2022 using a self-organizing maps feed-forward neural network (SOM-FNN) approach. The annual anthropogenic CO_2 (C_{ant}) flux (thick green line) includes a riverine adjustment of –0.65 Pg C. The black dashed line is the 1990–2020 mean C_{ant} flux. Negative values indicate CO_2 uptake by the ocean.

to 2020. However, the eastern equatorial Pacific, southeast of the Galapagos, shows a negative CO_2 flux anomaly. The positive anomalies in fluxes (more efflux/less influx in 2022 compared to the long-term mean) in the subtropics closely correspond to positive temperature anomalies (see Fig. 3.1a), suggesting that the flux anomalies in these regions are temperature driven.

The difference in fluxes between 2022 and 2021 (Fig. 3.29b) are quite muted, with broad regions in the northern Pacific subtropics showing positive anomalies (less strong sinks) closely corresponding with the SSTA changes observed between 2022 and 2021 (see Fig. 3.1b). The South Atlantic sector of the Southern Ocean (~60°S) shows a significant decrease in sink strength between 2022 and 2021 that does not correspond to a SST change but appears to be associated with a sea-surface salinity increase from 2021 to 2022 (see Fig. 3.7b). Most prevalent in Fig. 3.29b are the large regions of slight negative anomalies (greater uptake in 2022 compared to 2021), which in the South Pacific corresponds to negative SSTA.

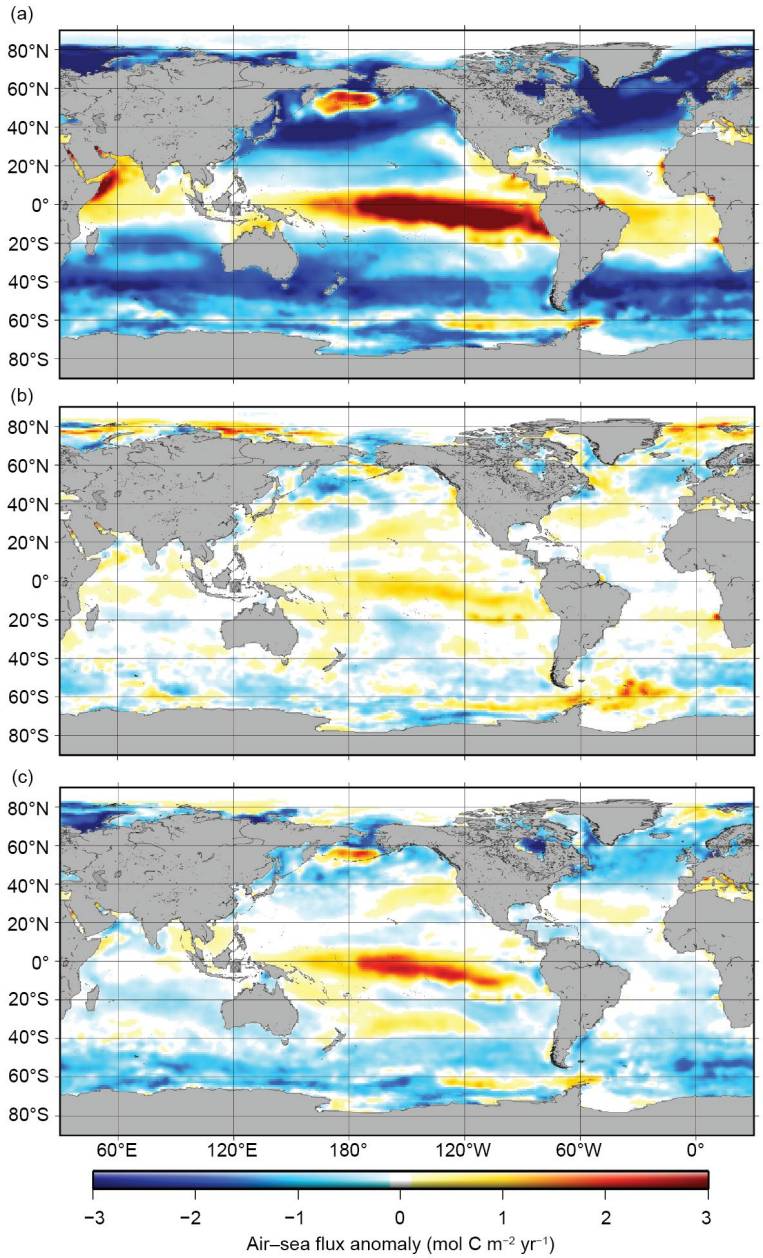

Fig. 3.29. Global map of (a) net air–sea carbon dioxide (CO_2) fluxes for 2022, (b) net air–sea CO_2 flux anomalies for 2022 minus 2021, and (c) net air–sea CO_2 flux anomalies for 2022 relative to 1990–2020 average values using the SOM-FNN approach of Landschützer et al. (2013). Units are all mol C m^{-2} yr^{-1}. Ocean CO_2 uptake regions shown in the blue colors.

3. OCEAN INTERIOR DEVELOPMENTS: UTILIZATION OF ARGO

Global-scale CO_2 emissions from human activities and associated CO_2 uptake are causing ocean interior C_{ant} increases and acidification. Delineating how the biogeochemical processes in the ocean interior will be affected by the changing heat content and C_{ant} uptake is essential for developing future mitigation and adaptation responses to climate change. Interior ocean carbon distributions have historically been quantified from observations from ship-based chemical surveys, many of which are currently being repeated decadally under the auspices of the international Global Ocean Ship-based Hydrographic Investigations Program. The measured distributions are analyzed to characterize both the natural and anthropogenic carbon components of the variability observed between reoccupations, and there are several such synthesis efforts underway including a decadal update to the first Regional Carbon Cycle Assessment and Processes (Khatiwala et al. 2013) study, and an update to decadal anthropogenic carbon accumulation estimates appropriate to the period 1994–2007 (Gruber et al. 2019) by Müller et al. (2023).

In recent years, oceanographers have developed algorithms that enable predictions of total dissolved inorganic carbon (DIC) and other carbonate chemistry parameters in the interior ocean from a variety of predictors (Alin et al. 2012; Williams et al. 2016; Carter et al. 2016, 2018, 2021; Bittig et al. 2018; Sauzède et al. 2017). Notably, there now exist algorithms (e.g., Carter et al. 2021; Keppler et al. 2022) that allow estimation of DIC from combinations of predictors (e.g., temperature and salinity) that are available at high resolution from Argo measurements throughout the top 2000 m of the ocean (Roemmich and Gilson 2009, and updates thereof). These algorithms can be used with the predictor data products to generate gap-filled monthly DIC distributions, e.g., for December 2022 (Fig. 3.30). However, seasonally resolved training data are needed for the algorithms to resolve seasonality with high fidelity (Carter et al. 2021; Gloege et al. 2021), and, while there are regions such as the northwest Pacific where this temporal coverage already exists from ship-based measurements thanks to regular cruises led by researchers based in Japan, these regions are few. Thus, the utility of these fully resolved carbon budgets remains limited at present.

The nascent and growing biogeochemical Argo program is poised to change this status quo by providing total scale seawater pH (pH_T) measurements over the top 2000 m at 10-day resolution throughout the various ocean basins, co-located with temperature, salinity, oxygen, and nitrate measurements. This information can be combined with estimates of seawater total alkalinity (TA), which has strong predictability from salinity due to the large role played by freshwater cycling in controlling the TA distribution, and macronutrients to allow calculations of DIC in the top 2000 m of the ocean at significantly greater temporal resolution than is achievable from discrete shipboard TA measurements. This information can then be used as additional training data to produce much more skillful DIC algorithms, similar to recent work using Argo O_2 sensor data (Sharp et al. 2022b; also see Sidebar 3.2), with a goal of annual updates of interior global ocean biogeochemistry.

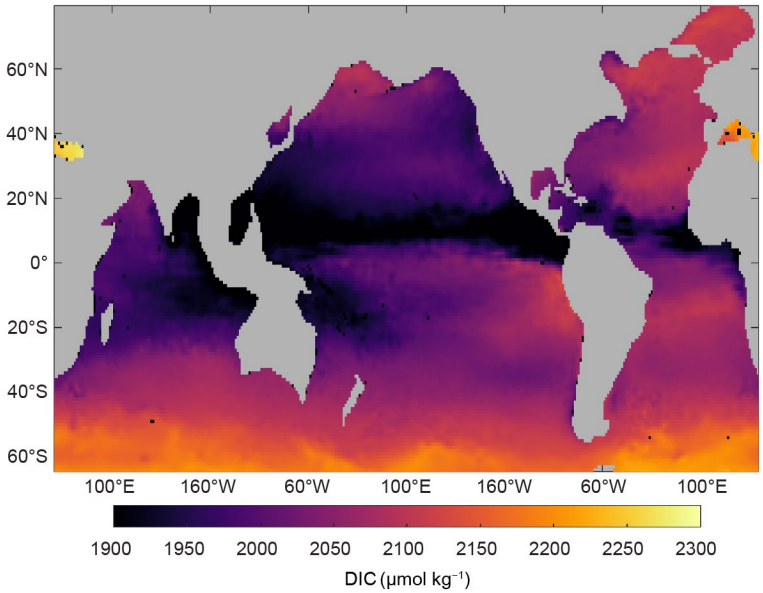

Fig. 3.30. Map of monthly average surface dissolved inorganic carbon (DIC; μmol kg^{-1}) for December 2022 estimated using the empirical seawater DIC estimation routine of Carter et al. (2021) and the monthly temperature and salinity record from Roemmich and Gilson (2009, updated).

A global surface ocean (top 2000 m) DIC inventory serves as an example of the information that can be obtained from this approach, albeit with large and yet-unconstrained uncertainties (Fig. 3.31a). These estimates were produced using the algorithms from Carter et al. (2021), which combine a large number of regionally specific linear regressions with machine learning approaches and the temperature and salinity climatology from Roemmich and Gilson (2009, with updates). There is an adjustment to the predictions to account for anthropogenic contributions to DIC, and this adjustment can be set to be appropriate for a fixed reference year (e.g., 2002 in Fig. 3.31) to isolate the variability in the DIC inventory estimates that is not attributable to estimated long-term secular change in the inventory. These estimates imply a strong anti-correlation between monthly (R^2=0.94) and annual (R^2=0.97) upper-ocean DIC inventory and temperature, which is not surprising given that the temperature is the main predictor used to generate the DIC estimates. Also, DIC and temperature tend to be anti-correlated due to the tendency for seawater to lose DIC to gas exchange when temperature increases. These early results point to a new frontier for interior ocean carbon cycle science that will likely see significant advances in the coming years with the advent of new data streams and continued iteration on machine learning mapping strategies.

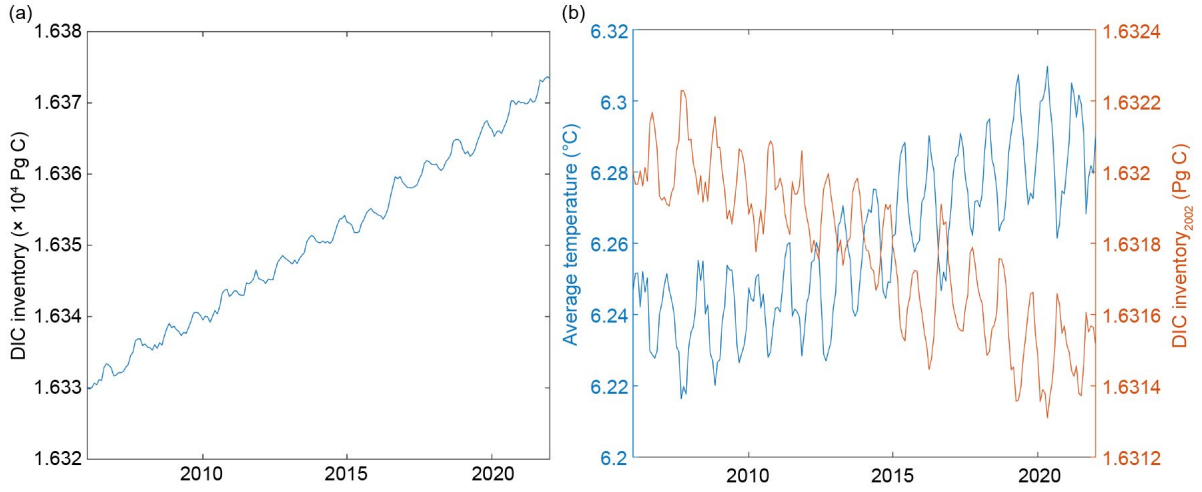

Fig. 3.31. (a) Estimated total dissolved inorganic carbon (DIC) inventory (Pg C) across the top 2000 m of the region covered by the Roemmich and Gilson (2009) product (see Fig. 3.30) and (b) estimated total DIC inventory (Pg C) over this same region that would be expected if anthropogenic carbon distributions were held at levels found in a reference year (2002) to reveal how patterns of estimated inventory change covary with the mass-weighted mean temperature product values used to produce the DIC estimates.

Acknowledgments

- Sidebar 3.1. This is NOAA's Pacific Marine Environmental Laboratory contribution no. 5470.
- Atlantic meridional overturning circulation. This work was carried out in part under the auspices of the Cooperative Institute for Marine and Atmospheric Studies, a Cooperative Institute of the University of Miami and the National Oceanic and Atmospheric Administration (NOAA), cooperative agreement #NA20OAR4320472. The MOC observations at 26.5°N have been jointly funded by the U.K. Natural Environment Research Council, the National Science Foundation, and NOAA's Global Ocean Monitoring and Observing (GOMO) program. The MOC estimates at 41°N were obtained at the Jet Propulsion Laboratory under a contract with NASA.
- D. L. Volkov was supported by NOAA's Climate Variability and Predictability program (Grant NA20OAR4310407) and Atlantic Oceanographic and Meteorological Laboratory (AOML).
- Shenfu Dong was supported via NOAA's GOMO program with additional support from NOAA's Atlantic Oceanographic & Meteorological Laboratory.
- W. Hobbs received grant funding from the Australian Government as part of the Antarctic Science Collaboration Initiative program.

Appendix 1: Chapter 3 – Acronyms

ACC	Antarctic Circumpolar Current
AMOC	Atlantic meridional overturning circulation
AMV	Atlantic Multidecadal Variability
AOML	Atlantic Oceanographic and Meteorological Laboratory
BASS	Blended Analysis of Surface Salinity
b_{bp}	particle backscattering coefficient
BGC	biogeochemical
C_{ant}	anthropogenic CO_2
CERES	Clouds and the Earth's Radiant Energy Systems
Chl*a*	chlorophyll-*a*
C_{phy}	phytoplankton carbon
CMIP	Coupled Model Intercomparison Project
CO_2	carbon dioxide
CSR	Center for Space Research
CTD	Conductivity-Temperature-Depth
DIC	dissolved inorganic carbon
DJF	December–February
DOISST	Daily Optimum Interpolation SST
DWBC	Deep Western Boundary Current
E	evaporation
EBAF	Energy Balanced and Filled
ECMWF	European Centre for Medium-Range Weather Forecasts
EKE	eddy kinetic energy
ENSO	El Niño–Southern Oscillation
ERA5	European Centre for Medium-Range Weather Forecasts Reanalysis version 5
ERSSTv5	Extended Reconstruction SST version 5
ESM	Earth system models
FC	Florida Current
fCO_{2w}	surface ocean fugacity of CO_2
FLASHFlux	Fast Longwave And Shortwave Radiative Fluxes
GIOP	Generalized Inherent Optical Properties
GMSL	global mean sea level
GMST	global mean surface air temperature
GO-SHIP	Global Ocean Ship-based Hydrographic Investigations Program
GOBAI-O2	Gridded Ocean Biogeochemistry from Artificial Intelligence-O_2
GOMO	Global Ocean Monitoring and Observing
GPCP	Global Precipitation Climatology Project
GRACE	Gravity Recovery and Climate Experiment
GRACE-FO	GRACE Follow-On
HadSST	U.K. Met Office Hadley Centre SST
IOD	Indian Ocean dipole
ITCZ	Intertropical Convergence Zone
JJA	June–August
JPL	Jet Propulsion Laboratory
LH	latent heat flux
LSW	Labrador Sea Water
LW	longwave radiation
MAM	March–May
MEI	Multivariate ENSO Index

MHT	meridional heat transport
MOC	meridional overturning circulation
MODIS	Moderate Resolution Imaging Spectroradiometer
MODIS-A	MODIS on *Aqua*
MOVE	Meridional Overturning Variability Experiment
NADW	North Atlantic Deep Water
NASA	National Aeronautics and Space Administration
NBC	North Brazil Current
NCEI	National Centers for Environmental Information
NECC	North Equatorial Countercurrent
NH	Northern Hemisphere
NOAA	National Oceanic and Atmospheric Administration
O_2	oxygen
OHCA	ocean heat content anomaly
P	Precipitation
pH_T	total scale seawater pH
PSO	permanently stratified ocean
PSS-78	Practical Salinity Scale-78
Q_{net}	net surface heat flux
RAPID/MOCHA/WBTS	Rapid Climate Change/MOC and Heatflux Array/Western Boundary Time Series
SD	standard deviation
SEC	South Equatorial Current
SH	Southern Hemisphere
SIO	Scripps Institution of Oceanography
SL	sea level
SLA	sea-level anomaly
SMAP	Soil Moisture Active Passive
SMOS	Soil Moisture and Ocean Salinity
SOCAT	Surface Ocean CO_2 Atlas
SOM-FNN	self-organizing maps feed-forward neural network
SON	September–November
SPCZ	South Pacific Convergence Zone
SSM/I	Special Sensor Microwave/Imager
SSS	sea-surface salinity
SST	sea-surface temperature
SSTA	sea-surface temperature anomaly
SW	shortwave radiation
TA	total alkalinity
U	maximum zonal currents
USV	uncrewed surface vehicles
W_{EK}	Ekman velocity
XBT	Expendable Bathythermographs
YC	Yucatan Current

References

Abraham, J. P., and Coauthors, 2013: A review of global ocean temperature observations: Implications for ocean heat content estimates and climate change. *Rev. Geophys.*, **51**, 450–483, https://doi.org/10.1002/rog.20022.

Adler, R. F., and Coauthors, 2018: The Global Precipitation Climatology Project (GPCP) Monthly analysis (new version 2.3) and a review of 2017 global precipitation. *Atmosphere*, **9**, 138, https://doi.org/10.3390/atmos9040138.

Alin, S. R., R. A. Feely, A. G. Dickson, J. M. Hernández-Ayón, L. W. Juranek, M. D. Ohman, and R. Goericke, 2012: Robust empirical relationships for estimating the carbonate system in the southern California Current System and application to CalCOFI hydrographic cruise data (2005–2011). *J. Geophys. Res.*, **117**, C05033, https://doi.org/10.1029/2011JC007511.

Babbin, A. R., D. Bianchi, A. Jayakumar, and B. B. Ward, 2015: Rapid nitrous oxide cycling in the suboxic ocean. *Science*, **348**, 1127–1129, https://doi.org/10.1126/science.aaa8380.

Babcock, R. C., and Coauthors, 2019: Severe continental-scale impacts of climate change are happening now: Extreme climate events impact marine habitat forming communities along 45% of Australia's coast. *Front. Mar. Sci.*, **6**, 411, https://doi.org/10.3389/fmars.2019.00411.

Bakker, D. C. E., and Coauthors, 2016: A multi-decade record of high-quality fCO_2 data in version 3 of the Surface Ocean CO_2 Atlas (SOCAT). *Earth Syst. Sci. Data*, **8**, 383–413, https://doi.org/10.5194/essd-8-383-2016.

Balaguru, K., P. Chang, R. Saravanan, L. R. Leung, Z. Xu, M. Li, and J. S. Hsieh, 2012: Ocean barrier layers' effect on tropical cyclone intensification. *Proc. Natl. Acad. Sci. USA*, **109**, 14 343–14 347, https://doi.org/10.1073/pnas.1201364109.

Barnoud, A., and Coauthors, 2021: Contributions of altimetry and Argo to non-closure of the global mean sea level budget since 2016. *Geophys. Res. Lett.*, **48**, e2021GL092824, https://doi.org/10.1029/2021GL092824.

Beal, L. M., V. Hormann, R. Lumpkin, and G. R. Foltz, 2013: The response of the surface circulation of the Arabian Sea to monsoonal forcing. *J. Phys. Oceanogr.*, **43**, 2008–2022, https://doi.org/10.1175/JPO-D-13-033.1.

Behrenfeld, M. J., and Coauthors, 2006: Climate-driven trends in contemporary ocean productivity. *Nature*, **444**, 752–755, https://doi.org/10.1038/nature05317.

—— , and Coauthors, 2015: Revaluating ocean warming impacts on global phytoplankton. *Nat. Climate Change*, **6**, 323–330, https://doi.org/10.1038/nclimate2838.

Berx, B., and Coauthors, 2021: Climate-relevant ocean transport measurements in the Atlantic and Arctic Oceans. *Oceanography*, **34**, 10–11, https://doi.org/10.5670/oceanog.2021.supplement.02-04.

Biló, T. C., and W. E. Johns, 2019: Interior pathways of Labrador Sea Water in the North Atlantic from the Argo perspective. *Geophys. Res. Lett.*, **46**, 3340–3348, https://doi.org/10.1029/2018GL081439.

—— , and —— , 2020: The deep western boundary current and adjacent interior circulation at 24°–30°N: Mean structure and mesoscale variability. *J. Phys. Oceanogr.*, **50**, 2735–2758, https://doi.org/10.1175/JPO-D-20-0094.1.

Bindoff, N. L., and Coauthors, 2019: Changing ocean, marine ecosystems, and dependent communities. *The Ocean and Cryosphere in a Changing Climate*, H.-O. Pörtner et al., Eds., Cambridge University Press, 447–588, https://doi.org/10.1017/9781009157964.

Bittig, H. C., and A. Körtzinger, 2015: Tackling oxygen optode drift: Near-surface and in-air oxygen optode measurements on a float provide an accurate in situ reference. *J. Atmos. Oceanic Technol.*, **32**, 1536–1543, https://doi.org/10.1175/JTECH-D-14-00162.1.

—— , and Coauthors, 2018: Oxygen optode sensors: Principle, characterization, calibration, and application in the ocean. *Front. Mar. Sci.*, **4**, 429, https://doi.org/10.3389/fmars.2017.00429.

Bopp, L., and Coauthors, 2013: Multiple stressors of ocean ecosystems in the 21st century: Projections with CMIP5 models. *Biogeosciences*, **10**, 6225–6245, https://doi.org/10.5194/bg-10-6225-2013.

Bourbonnais, A., R. T. Letscher, H. W. Bange, V. Echevin, J. Larkum, J. Mohn, N. Yoshida, and M. A. Altabet, 2017: N2O production and consumption from stable isotopic and concentration data in the Peruvian coastal upwelling system. *Global Biogeochem. Cycles*, **31**, 678–698, https://doi.org/10.1002/2016GB005567.

Bower, A., and Coauthors, 2019: Lagrangian views of the pathways of the Atlantic meridional overturning circulation. *J. Geophys. Res. Oceans*, **124**, 5313–5335, https://doi.org/10.1029/2019JC015014.

Boyer, T. P., and Coauthors, 2018: World Ocean Database 2018. A.V. Mishonov, Ed., NOAA Atlas NESDIS 87, 207 pp., www.ncei.noaa.gov/sites/default/files/2020-04/wod_intro_0.pdf.

Brandt, P., and Coauthors, 2015: On the role of circulation and mixing in the ventilation of oxygen minimum zones with a focus on the eastern tropical North Atlantic. *Biogeosciences*, **12**, 489–512, https://doi.org/10.5194/bg-12-489-2015.

Breitburg, D., and Coauthors, 2018: Declining oxygen in the global ocean and coastal waters. *Science*, **359**, eaam7240, https://doi.org/10.1126/science.aam7240.

Brown, J. R., and Coauthors, 2020: South Pacific Convergence Zone dynamics, variability and impacts in a changing climate. *Nat. Rev. Earth Environ.*, **1**, 530–543, https://doi.org/10.1038/s43017-020-0078-2.

Buchanan, P. J., and A. Tagliabue, 2021: The regional importance of oxygen demand and supply for historical ocean oxygen trends. *Geophys. Res. Lett.*, **48**, e2021GL094797, https://doi.org/10.1029/2021GL094797.

Bushinsky, S. M., S. R. Emerson, S. C. Riser, and D. D. Swift, 2016: Accurate oxygen measurements on modified Argo floats using in situ air calibrations. *Limnol. Oceanogr.: Methods*, **14**, 491–505, https://doi.org/10.1002/lom3.10107.

Canadell, J. G., and Coauthors, 2021: Global carbon and other biogeochemical cycles and feedbacks. *Climate Change 2021: The Physical Science Basis*, V. Masson-Delmotte et al., Eds., Cambridge University Press, 673–816, https://doi.org/10.1017/9781009157896.007.

Carpenter, J. H., 1965: The Chesapeake Bay Institute technique for the Winkler dissolved oxygen method. *Limnol. Oceanogr.*, **10**, 141–143, https://doi.org/10.4319/lo.1965.10.1.0141.

Carter, B. R., N. L. Williams, A. R. Gray, and R. A. Feely, 2016: Locally interpolated alkalinity regression for global alkalinity estimation. *Limnol. Oceanogr.: Methods*, **14**, 268–277, https://doi.org/10.1002/lom3.10087.

—— , R. A. Feely, N. L. Williams, A. G. Dickson, M. B. Fong, and Y. Takeshita, 2018: Updated methods for global locally interpolated estimation of alkalinity, pH, and nitrate. *Limnol. Oceanogr.: Methods*, **16**, 119–131, https://doi.org/10.1002/lom3.10232.

—— , and Coauthors, 2021: New and updated global empirical seawater property estimation routines. *Limnol. Oceanogr.: Methods*, **19**, 785–809, https://doi.org/10.1002/lom3.10461.

Chambers, D. P., A. Cazenave, N. Champollion, H. Dieng, W. Llovel, R. Forsberg, K. von Schuckmann, and Y. Wada, 2017: Evaluation of the global mean sea level budget between 1993 and 2014. *Surv. Geophys.*, **38**, 309–327, https://doi.org/10.1007/s10712-016-9381-3.

Chen, J., B. Tapley, C. Wilson, A. Cazenave, K. W. Seo, and J. S. Kim, 2020: Global ocean mass change from GRACE and GRACE Follow-On and altimeter and Argo measurements. *Geophys. Res. Lett.*, **47**, e2020GL090656, https://doi.org/10.1029/2020GL090656.

Cheng, L., J. Zhu, R. Cowley, T. Boyer, and S. Wijffels, 2014: Time, probe type, and temperature variable bias corrections to historical expendable bathythermograph observations. *J. Atmos. Oceanic Technol.*, **31**, 1793–1825, https://doi.org/10.1175/JTECH-D-13-00197.1.

—— , and Coauthors, 2023: Another year of record heat for the oceans. *Adv. Atmos. Sci.*, **40**, 963–974, https://doi.org/10.1007/s00376-023-2385-2.

Cheng, W., J. C. Chiang, and D. Zhang, 2013: Atlantic meridional overturning circulation (AMOC) in CMIP5 models: RCP and historical simulations. *J. Climate*, **26**, 7187–7197, https://doi.org/10.1175/JCLI-D-12-00496.1.

Chomiak, L. N., I. Yashayaev, D. L. Volkov, C. Schmid, and J. A. Hooper, 2022: Inferring advective timescales and overturning pathways of the Deep Western Boundary Current in the North Atlantic through Labrador Sea Water advection. *J. Geophys. Res. Oceans*, **127**, e2022JC018892, https://doi.org/10.1029/2022JC018892.

Claustre, H., K. S. Johnson, and Y. Takeshita, 2020: Observing the global ocean with biogeochemical-Argo. *Annu. Rev. Mar. Sci.*, **12**, 23–48, https://doi.org/10.1146/annurev-marine-010419-010956.

Crespo, L. R., A. Prigent, N. Keenlyside, S. Koseki, L. Svendsen, I. Richter, and E. Sánchez-Gómez, 2022: Weakening of the Atlantic Niño variability under global warming. *Nat. Climate Change*, **12**, 822–827, https://doi.org/10.1038/s41558-022-01453-y.

Danabasoglu, G., F. S. Castruccio, R. J. Small, R. Tomas, E. Frajka-Williams, and M. Lankhorst, 2021: Revisiting AMOC transport estimates from observations and models. *Geophys. Res. Lett.*, **48**, e2021GL093045, https://doi.org/10.1029/2021GL093045.

D'Asaro, E. A., and C. McNeil, 2013: Calibration and stability of oxygen sensors on autonomous floats. *J. Atmos. Oceanic Technol.*, **30**, 1896–1906, https://doi.org/10.1175/JTECH-D-12-00222.1.

de Boyer Montégut, C., G. Madec, A. S. Fischer, A. Lazar, and D. Iudicone, 2004: Mixed layer depth over the global ocean: An examination of profile data and a profile-based climatology. *J. Geophys. Res.*, **109**, C12003, https://doi.org/10.1029/2004JC002378.

Deser, C., M. A. Alexander, S. P. Xie, and A. S. Phillips, 2010: Sea surface temperature variability: Patterns and mechanisms. *Annu. Rev. Mar. Sci.*, **2**, 115–143, https://doi.org/10.1146/annurev-marine-120408-151453.

Deutsch, C., A. Ferrel, B. Seibel, H. O. Pörtner, and R. B. Huey, 2015: Climate change tightens a metabolic constraint on marine habitats. *Science*, **348**, 1132–1135, https://doi.org/10.1126/science.aaa1605.

Dierssen, H. M., 2010: Perspectives on empirical approaches for ocean color remote sensing of chlorophyll in a changing climate. *Proc. Natl. Acad. Sci. USA*, **107**, 17 073–17 078, https://doi.org/10.1073/pnas.0913800107.

DiNezio, P. N., C. Deser, Y. M. Okumura, and A. Karspeck, 2017: Predictability of 2-year La Niña events in a coupled general circulation model. *Climate Dyn.*, **49**, 4237–4261, https://doi.org/10.1007/s00382-017-3575-3.

Dlugokencky, E. J., K. W. Thoning, X. Lan, and P. P. Tans, 2021: NOAA greenhouse gas reference from atmospheric carbon dioxide dry air mole fractions from the NOAA GML Carbon Cycle Cooperative Global Air Sampling Network. NOAA, ftp://aftp.cmdl.noaa.gov/data/trace_gases/co2/flask/surface/.

Domingues, R., and Coauthors, 2015: Upper ocean response to Hurricane Gonzalo (2014): Salinity effects revealed by targeted and sustained underwater glider observations. *Geophys. Res. Lett.*, **42**, 7131–7138, https://doi.org/10.1002/2015GL065378.

—— , M. Baringer, and G. Goni, 2016: Remote sources for year-to-year changes in the seasonality of the Florida Current transport. *J. Geophys. Res. Oceans*, **121**, 7547–7559, https://doi.org/10.1002/2016JC012070.

Dong, S., G. Goni, R. Domingues, F. Bringas, M. Goes, J. Christophersen, and M. Baringer, 2021: Synergy of in-situ and satellite ocean observations in determining meridional heat transport in the Atlantic Ocean. *J. Geophys. Res. Oceans*, **126**, e2020JC017073, https://doi.org/10.1029/2020JC017073.

—— , D. L. Volkov, G. Goni, K. Pujiana, F. Tagklis, and M. Baringer, 2022: Remote impact of the equatorial Pacific on Florida Current transport. *Geophys. Res. Lett.*, **49**, e2021GL096944, https://doi.org/10.1029/2021GL096944.

Durack, P. J., and S. E. Wijffels, 2010: Fifty-year trends in global ocean salinities and their relationship to broad-scale warming. *J. Climate*, **23**, 4342–4362, https://doi.org/10.1175/2010JCLI3377.1.

—— , —— , and R. J. Matear, 2012: Ocean salinities reveal strong global water cycle intensification during 1950 to 2000. *Science*, **336**, 455–458, https://doi.org/10.1126/science.1212222.

Esaias, W. E., and Coauthors, 1998: An overview of MODIS capabilities for ocean science observations. *IEEE Trans. Geosci. Remote Sens.*, **36**, 1250–1265, https://doi.org/10.1109/36.701076.

Espinoza, J.-C., J. A. Marengo, J. Schongart, and J. C. Jiminez, 2022: The new historical flood of 2021 in the Amazon River compared to major floods of the 21st century: Atmospheric features in the context of the intensification of floods. *Wea. Climate Extremes*, **35**, 100406, https://doi.org/10.1016/j.wace.2021.100406.

Ezer, T., and L. P. Atkinson, 2014: Accelerated flooding along the U.S. East Coast: On the impact of sea-level rise, tides, storms, the Gulf Stream, and the North Atlantic Oscillations. *Earth's Future*, **2**, 362–382, https://doi.org/10.1002/2014EF000252.

Fasullo, J. T., and R. S. Nerem, 2018: Altimeter-era emergence of the patterns of forced sea-level rise in climate models and implications for the future. *Proc. Natl. Acad. Sci. USA*, **115**, 12 944–12 949, https://doi.org/10.1073/pnas.1813233115.

—— , —— , and B. Hamlington, 2016: Is the detection of accelerated sea-level rise imminent? *Sci. Rep.*, **6**, 31245, https://doi.org/10.1038/srep31245.

—— , N. Rosenbloom, and R. Buchholz, 2023: A multiyear tropical Pacific cooling response to recent Australian wildfires in CESM2. *Sci. Adv.*, **9**, eadg1213, https://doi.org/10.1126/sciadv.adg1213.

Ffield, A., 2007: Amazon and Orinoco River plumes and NBC rings: Bystanders or participants in hurricane events? *J. Climate*, **20**, 316–333, https://doi.org/10.1175/JCLI3985.1.

Field, C. B., M. J. Behrenfeld, J. T. Randerson, and P. Falkowski, 1998: Primary production of the biosphere: Integrating terrestrial and oceanic components. *Science*, **281**, 237–240, https://doi.org/10.1126/science.281.5374.237.

Fofonoff, N. P., and E. L. Lewis, 1979: A practical salinity scale. *J. Oceanogr. Soc. Japan*, **35**, 63–64, https://doi.org/10.1007/BF02108283.

Font, J., and Coauthors, 2013: SMOS first data analysis for sea surface salinity determination. *Int. J. Remote Sens.*, **34**, 3654–3670, https://doi.org/10.1080/01431161.2012.716541.

Fore, A. G., S. H. Yueh, W. Q. Tang, B. W. Stiles, and A. K. Hayashi, 2016: Combined active/passive retrievals of ocean vector wind and sea surface salinity with SMAP. *IEEE Trans. Geosci. Remote Sens.*, **54**, 7396–7404, https://doi.org/10.1109/TGRS.2016.2601486.

Forster, P., and Coauthors, 2021: The Earth's energy budget, climate feedbacks, and climate sensitivity. *Climate Change 2021: The Physical Science Basis*, V. Masson-Delmotte et al., Eds., Cambridge University Press, 923–1054, https://doi.org/10.1017/9781009157896.009.

Frajka-Williams, E., and Coauthors, 2016: Compensation between meridional flow components of the Atlantic MOC at 26°N. *Ocean Sci.*, **12**, 481–493, https://doi.org/10.5194/os-12-481-2016.

—— , and Coauthors, 2019: Atlantic meridional overturning circulation: Observed transports and variability. *Front. Mar. Sci.*, **6**, 260, https://doi.org/10.3389/fmars.2019.00260.

Franz, B. A., I. Cetinić, M. Gao, A. Siegel, and T. K. Westberry, 2022: Global ocean phytoplankton [in "State of the Climate in 2021"]. *Bull. Amer. Meteor. Soc.*, **103** (8), S180–S183, https://doi.org/10.1175/BAMS-D-22-0072.1.

Friedlingstein, P., and Coauthors, 2022: Global carbon budget 2022. *Earth Syst. Sci. Data*, **14**, 4811–4900, https://doi.org/10.5194/essd-14-4811-2022.

Fyfe, J. C., and Coauthors, 2016: Making sense of the early-2000s warming slowdown. *Nat. Climate Change*, **6**, 224–228, https://doi.org/10.1038/nclimate2938.

Garcia, H. E., and L. I. Gordon, 1992: Oxygen solubility in seawater: Better fitting equations. *Limnol. Oceanogr.*, **37**, 1307–1312, https://doi.org/10.4319/lo.1992.37.6.1307.

Geider, R. J., H. L. MacIntyre, and T. M. Kana, 1997: Dynamic model of phytoplankton growth and acclimation: Responses of the balanced growth rate and the chlorophyll *a*: Carbon ratio to light, nutrient limitation and temperature. *Mar. Ecol.: Prog. Ser.*, **148**, 187–200, https://doi.org/10.3354/meps148187.

Gloege, L., and Coauthors, 2021: Quantifying errors in observationally based estimates of ocean carbon sink variability. *Global Biogeochem. Cycles*, **35**, e2020GB006788, https://doi.org/10.1029/2020GB006788.

Goni, G. J., and W. E. Johns, 2003: Synoptic study of warm rings in the North Brazil Current retroflection region using satellite altimetry. *Interhemispheric Water Exchange in the Atlantic Ocean*, G. J. Goni and P. Malanotte-Rizzoli, Eds., Elsevier Oceanography Series, Vol. 68, Elsevier, 335–356, https://doi.org/10.1016/S0422-9894(03)80153-8.

—— , F. Bringas, and P. N. Di Nezio, 2011: Observed low frequency variability of the Brazil Current front. *J. Geophys. Res.*, **116**, C10037, https://doi.org/10.1029/2011JC007198.

Good, S. A., M. J. Martin, and N. A. Rayner, 2013: EN4: Quality controlled ocean temperature and salinity profiles and monthly objective analyses with uncertainty estimates. *J. Geophys. Res. Oceans*, **118**, 6704–6716, https://doi.org/10.1002/2013JC009067.

Gouretski, V., and L. Cheng, 2020: Correction for systematic errors in the global dataset of temperature profiles from mechanical bathythermographs. *J. Atmos. Oceanic Technol.*, **37**, 841–855, https://doi.org/10.1175/JTECH-D-19-0205.1.

Graff, J. R., and Coauthors, 2015: Analytical phytoplankton carbon measurements spanning diverse ecosystems. *Deep-Sea Res. I*, **102**, 16–25, https://doi.org/10.1016/j.dsr.2015.04.006.

Gruber, N., 2008: The marine nitrogen cycle: Overview and challenges. *Nitrogen in the Marine Environment*, 2nd ed. D. G. Capone et al., Eds., Academic Press, 1–50.

—— , and Coauthors, 2010: Adding oxygen to Argo: Developing a global in-situ observatory for ocean deoxygenation and biogeochemistry. *Proc. OceanObs'09: Sustained Ocean Observations and Information for Society*, Venice, Italy, European Space Agency, 12 pp., https://doi.org/10.5270/OceanObs09.cwp.39.

—— , and Coauthors, 2019: The oceanic sink for anthropogenic CO_2 from 1994 to 2007. *Science*, **363**, 1193–1199, https://doi.org/10.1126/science.aau5153.

Hakuba, M. Z., T. Frederikse, and F. W. Landerer, 2021: Earth's energy imbalance from the ocean perspective (2005–2019). *Geophys. Res. Lett.*, **48**, e2021GL093624, https://doi.org/10.1029/2021GL093624.

Hamlington, B. D., C. G. Piecuch, J. T. Reager, H. Chandanpurkar, T. Frederikse, R. S. Nerem, J. T. Fasullo, and S.-H. Cheon, 2020: Origin of interannual variability in global mean sea level. *Proc. Natl. Acad. Sci. USA*, **117**, 13 983–13 990, https://doi.org/10.1073/pnas.1922190117.

Han, W., G. A. Meehl, D. Stammer, A. Hu, B. Hamlington, J. Kenigson, H. Palanisamy, and P. Thompson, 2017: Spatial patterns of sea level variability associated with natural internal climate modes. *Surv. Geophys.*, **38**, 217–250, https://doi.org/10.1007/s10712-016-9386-y.

Hasan, N. A., Y. Chikamoto, and M. J. McPhaden, 2022: The influence of tropical basin interactions on the 2020–22 double-dip La Niña. *Front. Climate*, **4**, 1001174, https://doi.org/10.3389/fclim.2022.1001174.

Held, I. M., and B. J. Soden, 2006: Robust responses of the hydrological cycle to global warming. *J. Climate*, **19**, 5686–5699, https://doi.org/10.1175/JCLI3990.1.

Helm, K. P., N. L. Bindoff, and J. A. Church, 2011: Observed decreases in oxygen content of the global ocean. *Geophys. Res. Lett.*, **38**, L23602, https://doi.org/10.1029/2011GL049513.

Hersbach, H., and Coauthors, 2018: ERA5 hourly data on single levels from 1940 to present. Copernicus Climate Change Service (C3S) Climate Data Store (CDS), accessed 4 January 2023, https://doi.org/10.24381/cds.adbb2d47.

—— , and Coauthors, 2020: The ERA5 global reanalysis. *Quart. J. Roy. Meteor. Soc.*, **146**, 1999–2049, https://doi.org/10.1002/qj.3803.

Hobbs, W. R., and J. K. Willis, 2012: Midlatitude North Atlantic heat transport: A time series based on satellite and drifter data. *J. Geophys. Res.*, **117**, C01008, https://doi.org/10.1029/2011JC007039.

Hu, C., Z. Lee, and B. A. Franz, 2012: Chlorophyll a algorithms for oligotrophic oceans: A novel approach based on three-band reflectance difference. *J. Geophys. Res.*, **117**, C01011, https://doi.org/10.1029/2011JC007395.

—— , L. Feng, Z. Lee, B. A. Franz, S. W. Bailey, P. J. Werdell, and C. W. Proctor, 2019: Improving satellite global chlorophyll a data products through algorithm refinement and data recovery. *J. Geophys. Res. Oceans*, **124**, 1524–1543, https://doi.org/10.1029/2019JC014941.

Hu, S., and A. V. Fedorov, 2017: The extreme El Niño of 2015–2016 and the end of global warming hiatus. *Geophys. Res. Lett.*, **44**, 3816–3824, https://doi.org/10.1002/2017GL072908.

Huang, B., and Coauthors, 2015: Extended Reconstructed Sea Surface Temperature version 4 (ERSST.v4). Part I: Upgrades and intercomparisons. *J. Climate*, **28**, 911–930, https://doi.org/10.1175/JCLI-D-14-00006.1.

——, and Coauthors, 2017: Extended Reconstructed Sea Surface Temperature version 5 (ERSSTv5): Upgrades, validations, and intercomparisons. *J. Climate*, **30**, 8179–8205, https://doi.org/10.1175/JCLI-D-16-0836.1.

——, and Coauthors, 2020: Uncertainty estimates for sea surface temperature and land surface air temperature in NOAAGlobalTemp version 5. *J. Climate*, **33**, 1351–1379, https://doi.org/10.1175/JCLI-D-19-0395.1.

——, C. Liu, V. Banzon, E. Freeman, G. Graham, B. Hankins, T. Smith, and H.-M. Zhang, 2021a: Improvements of the Daily Optimum Interpolation Sea Surface Temperature (DOISST) version 2.1. *J. Climate*, **34**, 2923–2939, https://doi.org/10.1175/JCLI-D-20-0166.1.

——, Z. Wang, X. Yin, A. Arguez, G. Graham, C. Liu, T. Smith, H.-M. Zhang, 2021b: Prolonged marine heatwaves in the Arctic: 1982–2020. *Geophys. Res. Lett.*, **48**, e2021GL095590, https://doi.org/10.1029/2021GL095590.

Huffman, G. J., R. F. Adler, D. T. Bolvin, and G. Gu, 2009: Improving the global precipitation record. GPCP version 2.1. *Geophys. Res. Lett.*, **36**, L17808, https://doi.org/10.1029/2009GL040000.

Hummels, R., B. Johns, S. Speich, R. Perez, P. Brandt, M. Lankhorst, and U. Send, 2022: Theme 3: The AMOC in the Tropical Atlantic. *CLIVAR Exchanges*, No. 82, International CLIVAR Project Office, Southampton, United Kingdom, 22–28, http://doi.org/10.36071/clivar.82.2022.

IPCC, 2021: *Climate Change 2021: The Physical Science Basis*, V. Masson-Delmotte et al., Eds., Cambridge University Press, 2391 pp.

Ishii, M., Y. Fukuda, S. Hirahara, S. Yasui, T. Suzuki, and K. Sato, 2017: Accuracy of global upper ocean heat content estimation expected from present observational datasets. *SOLA*, **13**, 163–167, https://doi.org/10.2151/sola.2017-030.

Ito, T., S. Minobe, M. C. Long, and C. Deutsch, 2017: Upper ocean O_2 trends: 1958–2015. *Geophys. Res. Lett.*, **44**, 4214–4223, https://doi.org/10.1002/2017GL073613.

Jin, F.-F., 1997: An equatorial ocean recharge paradigm for ENSO. Part I: Conceptual model. *J. Atmos. Sci.*, **54**, 811–829, https://doi.org/10.1175/1520-0469(1997)0542.0.CO;2.

Johns, W. E., and Coauthors, 2011: Continuous, array-based estimates of Atlantic Ocean heat transport at 26.5°N. *J. Climate*, **24**, 2429–2449, https://doi.org/10.1175/2010JCLI3997.1.

Johnson, G. C., and J. M. Lyman, 2012: Sea surface salinity [in "State of the Climate in 2011"]. *Bull. Amer. Meteor. Soc.*, **93** (7), S68–S69, https://doi.org/10.1175/2012BAMSStateoftheClimate.1.

——, and ——, 2020: Warming trends increasingly dominate Global Ocean. *Nat. Climate Change*, **10**, 757–761, https://doi.org/10.1038/s41558-020-0822-0.

——, ——, J. K. Willis, T. Boyer, J. Antonov, S. A. Good, C. M. Domingues, and N. Bindoff, 2014: Ocean heat content [in "State of the Climate in 2013"]. *Bull. Amer. Meteor. Soc.*, **95** (7), S54–S57, https://doi.org/10.1175/2014BAMSStateoftheClimate.1.

——, ——, J. Antonov, N. Bindoff, T. Boyer, C. M. Domingues, S. A. Good, M. Ishii, and J. K. Willis, 2015: Ocean heat content [in "State of the Climate in 2014"]. *Bull. Amer. Meteor. Soc.*, **96** (7), S64–S66, https://doi.org/10.1175/2015BAMSStateoftheClimate.1.

——, J. Reagan, J. M. Lyman, T. Boyer, C. Schmid, and R. Locarnini, 2020: Salinity [in "State of the Climate in 2019"]. *Bull. Amer. Meteor. Soc.*, **101** (8), S129–S183, https://doi.org/10.1175/BAMS-D-20-0105.1.

——, and Coauthors, 2022: Ocean heat content [in "State of the Climate in 2021"]. *Bull. Amer. Meteor. Soc.*, **103** (8), S153–S157, https://doi.org/10.1175/.

Kanamitsu, M., W. Ebisuzaki, J. Woollen, S.-K. Yang, J. J. Hnilo, M. Fiorino, and G. L. Potter, 2002: NCEP–DOE AMIP-II Reanalysis (R-2). *Bull. Amer. Meteor. Soc.*, **83**, 1631–1644, https://doi.org/10.1175/BAMS-83-11-1631.

Kanzow, T., U. Send, W. Zenk, A. D. Chave, and M. Rhein, 2006: Monitoring the integrated deep meridional flow in the tropical North Atlantic: Long-term performance of a geostrophic array. *Deep-Sea Res. I*, **53**, 528–546, https://doi.org/10.1016/j.dsr.2005.12.007.

Kato, S., and Coauthors, 2018: Surface irradiances of Edition 4.0 Clouds and the Earth's Radiant Energy System (CERES) Energy Balanced and Filled (EBAF) data product. *J. Climate*, **31**, 4501–4527, https://doi.org/10.1175/JCLI-D-17-0523.1.

Keeling, R. F., A. Körtzinger, and N. Gruber, 2010: Ocean deoxygenation in a warming world. *Annu. Rev. Mar. Sci.*, **2**, 199–229, https://doi.org/10.1146/annurev.marine.010908.163855.

Kennedy, J. J., N. A. Rayner, C. P. Atkinson, and R. E. Killick, 2019: An ensemble data set of sea surface temperature change from 1850: The Met Office Hadley Centre HadSST.4.0.0.0 data set. *J. Geophys. Res. Atmos.*, **124**, 7719–7763, https://doi.org/10.1029/2018JD029867.

Keppler, L., P. Landschützer, S. K. Lauvset, and N. Gruber, 2023: Recent trends and variability in the oceanic storage of dissolved inorganic carbon. *Global Biogeochem. Cycles*, **37**, e2022GB007677, https://doi.org/10.1029/2022GB007677.

Kersalé, M., and Coauthors, 2021: Multi-year estimates of daily heat transport by the Atlantic meridional overturning circulation at 34.5°S. *J. Geophys. Res. Oceans*, **126**, e2020JC016947, https://doi.org/10.1029/2020JC016947.

Khatiwala, S., and Coauthors, 2013: Global ocean storage of anthropogenic carbon. *Biogeosciences*, **10**, 2169–2191, https://doi.org/10.5194/bg-10-2169-2013.

Koch, L. G., and S. L. Britton, 2008: Aerobic metabolism underlies complexity and capacity. *J. Physiol.*, **586**, 83–95, https://doi.org/10.1113/jphysiol.2007.144709.

Koelling, J., U. Send, and M. Lankhorst, 2020: Decadal strengthening of interior flow of North Atlantic Deep Water observed by GRACE satellites. *J. Geophys. Res. Oceans*, **125**, e2020JC016217, https://doi.org/10.1029/2020JC016217.

Kwiatkowski, L., and Coauthors, 2020: Twenty-first century ocean warming, acidification, deoxygenation, and upper-ocean nutrient and primary production decline from CMIP6 model projections. *Biogeosciences*, **17**, 3439–3470, https://doi.org/10.5194/bg-17-3439-2020.

Landschützer, P., N. Gruber, D. C. E. Bakker, U. Schuster, S. Nakaoka, M. R. Payne, T. P. Sasse, and J. Zeng, 2013: A neural network-based estimate of the seasonal to inter-annual variability of the Atlantic Ocean carbon sink. *Biogeosciences*, **10**, 7793–7815, https://doi.org/10.5194/bg-10-7793-2013.

——, ——, ——, and ——, 2014: Recent variability of the global ocean carbon sink. *Global Biogeochem. Cycles*, **28**, 927–949, https://doi.org/10.1002/2014GB004853.

Langdon, C., 2010: Determination of dissolved oxygen in seawater by Winkler titration using Amperometric Technique. The GO-SHIP Repeat Hydrography Manual: A Collection of Expert Reports and Guidelines, Version 1, E. M. Hood, C. L. Sabine, and B. M. Sloyan, Eds., IOCCP Rep. 14, ICPO Publ. Series 134, 18 pp., https://doi.org/10.25607/OBP-1350.

Lauvset, S. K., and Coauthors, 2016: A new global interior ocean mapped climatology: The 1 ´ 1 GLODAP version 2. *Earth Syst. Sci. Data*, **8**, 325–340, https://doi.org/10.5194/essd-8-325-2016.

Le Bras, I. A., I. Yashayaev, and J. M. Toole, 2017: Tracking Labrador Sea Water property signals along the Deep Western Boundary Current. *J. Geophys. Res. Oceans*, **122**, 5348–5366, https://doi.org/10.1002/2017JC012921.

Leuliette, E. W., and J. K. Willis, 2011: Balancing the sea level budget. *Oceanography*, **24**, 122–129, https://doi.org/10.5670/oceanog.2011.32.

Levin, L. A., 2018: Manifestation, drivers, and emergence of open ocean deoxygenation. *Annu. Rev. Mar. Sci.*, **10**, 229–260, https://doi.org/10.1146/annurev-marine-121916-063359.

—— , and Coauthors, 2009: Effects of natural and human-induced hypoxia on coastal benthos. *Biogeosciences*, **6**, 2063–2098, https://doi.org/10.5194/bg-6-2063-2009.

Le Vine, D. M., E. P. Dinnat, G. S. E. Lagerloef, P. de Matthaeis, S. Abraham, C. Utku, and H. Kao, 2014: Aquarius: Status and recent results. *Radio Sci.*, **49**, 709–720, https://doi.org/10.1002/2014RS005505.

Levitus, S., and Coauthors, 2012: World ocean heat content and thermosteric sea level change (0–2000 m), 1955–2010. *Geophys. Res. Lett.*, **39**, L10603, https://doi.org/10.1029/2012GL051106.

Li, L., R. W. Schmitt, C. C. Ummenhofer, and K. B. Karnauskas, 2016: North Atlantic salinity as a predictor of Sahel rainfall. *Sci. Adv.*, **2**, e1501588, https://doi.org/10.1126/sciadv.1501588.

Li, X., Z.-Z. Hu, and B. Huang, 2020: Subannual to interannual variabilities of SST in the North Atlantic Ocean. *J. Climate*, **33**, 5547–5564, https://doi.org/10.1175/JCLI-D-19-0556.1.

Llovel, W., and L. Terray, 2016: Observed southern upper-ocean warming over 2005–2014 and associated mechanisms. *Environ. Res. Lett.*, **11**, 124023, https://doi.org/10.1088/1748-9326/11/12/124023.

Loeb, N. G., G. C. Johnson, T. J. Thorsen, J. M. Lyman, F. G. Rose, and S. Kato, 2021: Satellite and ocean data reveal marked increase in Earth's heating rate. *Geophys. Res. Lett.*, **48**, e2021GL093047, https://doi.org/10.1029/2021GL093047.

Lozier, M. S., A. S. Bower, H. H. Furey, K. L. Drouin, X. Xu, and S. Zou, 2022: Overflow water pathways in the North Atlantic. *Prog. Oceanogr.*, **208**, 102874, https://doi.org/10.1016/j.pocean.2022.102874.

Lumpkin, R., and S. L. Garzoli, 2005: Near-surface circulation in the tropical Atlantic Ocean. *Deep-Sea Res. I*, **52**, 495–518, https://doi.org/10.1016/j.dsr.2004.09.001.

—— , and —— : Interannual to decadal changes in the western South Atlantic's surface circulation. *J. Geophys. Res.*, **116**, C01014, https://doi.org/10.1029/2010JC006285.

—— , and G. Johnson, 2013: Global ocean surface velocities from drifters: Mean, variance, El Niño–Southern Oscillation response, and seasonal cycle. *J. Geophys. Res. Oceans*, **118**, 2992–3006, https://doi.org/10.1002/jgrc.20210.

—— , G. Goni, and K. Dohan, 2012: Surface currents [in "State of the Climate in 2011"]. *Bull. Amer. Meteor. Soc.*, **93** (7), S75–S78, https://doi.org/10.1175/2012BAMSStateoftheClimate.1.

Lyman, J. M., and G. C. Johnson, 2014: Estimating global ocean heat content changes in the upper 1800 m since 1950 and the influence of climatology choice. *J. Climate*, **27**, 1945–1957, https://doi.org/10.1175/JCLI-D-12-00752.1.

Mantua, N. J., and S. R. Hare, 2002: The Pacific decadal oscillation. *J. Oceanogr.*, **58**, 35–44, https://doi.org/10.1023/A:1015820616384.

Maritorena, S., O. Hembise Fanton d'Andon, A. Mangin, and D. A. Siegel, 2010: Merged satellite ocean color data products using a bio-optical model: Characteristics, benefits and issues. *Remote Sens. Environ.*, **114**, 1791–1804, https://doi.org/10.1016/j.rse.2010.04.002.

Marti, F., and Coauthors, 2022: Monitoring the ocean heat content change and the Earth energy imbalance from space altimetry and space gravimetry. *Earth Syst. Sci. Data*, **14**, 229–249, https://doi.org/10.5194/essd-14-229-2022.

Maurer, T. L., J. N. Plant, and K. S. Johnson, 2021: Delayed-mode quality control of oxygen, nitrate, and pH data on SOCCOM biogeochemical profiling floats. *Front. Mar. Sci.*, **8**, 683207, https://doi.org/10.3389/fmars.2021.683207.

McCarthy, G. D., and Coauthors, 2015: Measuring the Atlantic Meridional Overturning Circulation at 26°N. *Prog. Oceanogr.*, **130**, 91–111, https://doi.org/10.1016/j.pocean.2014.10.006.

McClain, C. R., 2009: A decade of satellite ocean color observations. *Annu. Rev. Mar. Sci.*, **1**, 19–42, https://doi.org/10.1146/annurev.marine.010908.163650.

McKinna, L. I. W., P. J. Werdell, and C. W. Proctor, 2016: Implementation of an analytical Raman scattering correction for satellite ocean-color processing. *Opt. Express*, **24**, A1123–A1137, https://doi.org/10.1364/OE.24.0A1123.

McPhaden, M. J., T. Lee, S. Fournier, and M. A. Balmaseda, 2021: ENSO observations. *El Niño Southern Oscillation in a Changing Climate*, *Geophys. Monogr.*, Vol. 253, Amer. Geophys. Union, 39–63, https://doi.org/10.1002/9781119548164.ch3.

Merrifield, M., 2011: A shift in western tropical Pacific sea level trends during the 1990s. *J. Climate*, **24**, 4126–4138, https://doi.org/10.1175/2011JCLI3932.1.

Moana Project, 2022: It's been a hot year – Moana Project marine heatwave research. 2 pp., www.moanaproject.org/s/Marine-heatwaves.pdf.

Moat, B. I., and Coauthors, 2020: Pending recovery in the strength of the meridional overturning circulation at 26°N. *Ocean Sci.*, **16**, 863–874, https://doi.org/10.5194/os-16-863-2020.

—— , E. Frajka-Williams, D. A. Smeed, D. Rayner, W. E. Johns, M. O. Baringer, D. Volkov, and J. Collins, 2022: Atlantic meridional overturning circulation observed by the RAPID-MOCHA-WBTS (RAPID-Meridional Overturning Circulation and Heatflux Array-Western Boundary Time Series) array at 26N from 2004 to 2020 (v2020.2). NERC EDS British Oceanographic Data Centre NOC, accessed 24 January 2023, https://doi.org/10.5285/e91b10af-6f0a-7fa7-e053-6c86abc05a09.

Mulet, S., and Coauthors, 2021: The new CNES-CLS18 global mean dynamic topography. *Ocean Sci.*, **17**, 789–808, https://doi.org/10.5194/os-17-789-2021.

Müller, J. D., and Coauthors, 2023: Decadal trends in the oceanic storage of anthropogenic carbon from 1994 to 2014. ESS Open Archive, accessed 1 February 2023, https://doi.org/10.22541/essoar.167525217.76035050/v1.

Nerem, R. S., B. D. Beckley, J. T. Fasullo, B. D. Hamlington, D. Masters, and G. T. Mitchum, 2018: Climate-change-driven accelerated sea-level rise detected in the altimeter era. *Proc. Natl. Acad. Sci. USA*, **115**, 2022–2025, https://doi.org/10.1073/pnas.1717312115.

Oliver, E. C., J. A. Benthuysen, N. L. Bindoff, A. J. Hobday, N. J. Holbrook, C. N. Mundy, and S. E. Perkins-Kirkpatrick, 2017: The unprecedented 2015/16 Tasman Sea marine heatwave. *Nat. Commun.*, **8**, 16101, https://doi.org/10.1038/ncomms16101.

—— , —— , S. Darmaraki, M. G. Donat, A. J. Hobday, N. J. Holbrook, R. W. Schlegel, and A. Sen Gupta, 2021: Marine heatwaves. *Annu. Rev. Mar. Sci.*, **13**, 313–342, https://doi.org/10.1146/annurev-marine-032720-095144.

O'Reilly, J. E., and P. J. Werdell, 2019: Chlorophyll algorithms for ocean color sensors – OC4, OC5 & OC6. *Remote Sens. Environ.*, **229**, 32–47, https://doi.org/10.1016/j.rse.2019.04.021.

Oschlies, A., K. G. Schulz, U. Riebesell, and A. Schmittner, 2008: Simulated 21st century's increase in oceanic suboxia by CO_2-enhanced biotic carbon export. *Global Biogeochem. Cycles*, **22**, GB4008, https://doi.org/10.1029/2007GB003147.

—— , O. Duteil, J. Getzlaff, W. Koeve, A. Landolfi, and S. Schmidtko, 2017: Patterns of deoxygenation: Sensitivity to natural and anthropogenic drivers. *Philos. Trans. Roy. Soc.*, **A375**, 20160325, https://doi.org/10.1098/rsta.2016.0325.

—— , P. Brandt, L. Stramma, and S. Schmidtko, 2018: Drivers and mechanisms of ocean deoxygenation. *Nat. Geosci.*, **11**, 467–473, https://doi.org/10.1038/s41561-018-0152-2.

Palmer, M. D., K. Haines, S. F. B. Tett, and T. J. Ansell, 2007: Isolating the signal of ocean global warming. *Geophys. Res. Lett.*, **34**, L23610, https://doi.org/10.1029/2007GL031712.

Park, J.-H., J.-S. Kug, Y.-M. Yang, T. Li, and H.-S. Jo, 2021: Mid-latitude leading double-dip La Niña. *Int. J. Climatol.*, **41**, E1353–E1370, https://doi.org/10.1002/joc.6772.

Payne, A. E., and Coauthors, 2020: Responses and impacts of atmospheric rivers to climate change. *Nat. Rev. Earth Environ.*, **1**, 143–157, https://doi.org/10.1038/s43017-020-0030-5.

Perkins-Kirkpatrick, S. E., A. D. King, E. A. Cougnon, N. J. Holbrook, M. R. Grose, E. C. J. Oliver, S. C. Lewis, and F. Pourasghar, 2019: The role of natural variability and anthropogenic climate change in the 2017/18 Tasman Sea marine heatwave [in "Explaining Extremes of 2017 from a Climate Perspective"]. *Bull. Amer. Meteor. Soc.*, **100** (1), S105–S110, https://doi.org/10.1175/BAMS-D-18-0116.1.

Pörtner, H. O., and R. Knust, 2007: Climate change affects marine fishes through the oxygen limitation of thermal tolerance. *Science*, **315**, 95–97, https://doi.org/10.1126/science.1135471.

Purkey, S. G., and G. C. Johnson, 2010: Warming of global abyssal and deep Southern Ocean waters between the 1990s and 2000s: Contributions to global heat and sea-level rise budgets. *J. Climate*, **23**, 6336–6351, https://doi.org/10.1175/2010JCLI3682.1.

Qiu, B., and S. Chen, 2021: Revisit of the occurrence of the Kuroshio large meander south of Japan. *J. Phys. Oceanogr.*, **51**, 3679–3694, https://doi.org/10.1175/JPO-D-21-0167.1.

—— , —— , N. Schneider, E. Oka, and S. Sugimoto, 2020: On the reset of the wind-forced decadal Kuroshio Extension variability in late 2017. *J. Climate*, **33**, 10 813–10 828, https://doi.org/10.1175/JCLI-D-20-0237.1.

Rayner, N. A., D. E. Parker, E. B. Horton, C. K. Folland, L. V. Alexander, D. P. Rowell, E. C. Kent, and A. Kaplan, 2003: Global analyses of sea surface temperature, sea ice, and night marine air temperature since the late nineteenth century. *J. Geophys. Res.*, **108**, 4407, https://doi.org/10.1029/2002JD002670.

Reagan, J., T. Boyer, C. Schmid, and R. Locarnini, 2020: Subsurface salinity [in "State of the Climate in 2019"]. *Bull. Amer. Meteor. Soc.*, **101** (8), S144–S148, https://doi.org/10.1175/BAMS-D-20-0105.1.

—— , —— , —— , and —— , 2021: Subsurface salinity [in "State of the Climate in 2020"]. *Bull. Amer. Meteor. Soc.*, **102** (8), S162–S164, https://doi.org/10.1175/BAMS-D-21-0083.1.

—— , —— , —— , and —— , 2022: Subsurface salinity [in "State of the Climate in 2021"]. *Bull. Amer. Meteor. Soc.*, **103** (8), S160–S162, https://doi.org/10.1175/BAMS-D-22-0072.1.

Ren, L., K. Speer, and E. P. Chassignet, 2011: The mixed layer salinity budget and sea ice in the Southern Ocean. *J. Geophys. Res.*, **116**, C08031, https://doi.org/10.1029/2010JC006634.

Resplandy, L., and Coauthors, 2018: Revision of global carbon fluxes based on a reassessment of oceanic and riverine carbon transport. *Nat. Geosci.*, **11**, 504–509, https://doi.org/10.1038/s41561-018-0151-3.

Riser, S. C., and Coauthors, 2016: Fifteen years of ocean observations with the global Argo array. *Nat. Climate Change*, **6**, 145–153, https://doi.org/10.1038/nclimate2872.

Rödenbeck, C., and Coauthors, 2015: Data-based estimates of the ocean carbon sink variability – First results of the Surface Ocean pCO_2 Mapping intercomparison (SOCOM). *Biogeosciences*, **12**, 7251–7278, https://doi.org/10.5194/bg-12-7251-2015.

Roemmich, D., and J. Gilson, 2009: The 2004–2008 mean and annual cycle of temperature, salinity, and steric height in the global ocean from the Argo Program. *Prog. Oceanogr.*, **82**, 81–100, https://doi.org/10.1016/j.pocean.2009.03.004.

—— , and Coauthors, 2009: The Argo Program: Observing the global ocean with profiling floats. *Oceanography*, **22**, 34–43, https://doi.org/10.5670/oceanog.2009.36.

—— , and Coauthors, 2019: On the future of Argo: A global, full-depth, multi-disciplinary array. *Front. Mar. Sci.*, **6**, 439, https://doi.org/10.3389/fmars.2019.00439.

Saji, N. H., B. N. Goswami, P. N. Vinayachandran, and T. Yamagata, 1999: A dipole mode in the tropical Indian Ocean. *Nature*, **401**, 360–363, https://doi.org/10.1038/43854.

Sanchez-Franks, A., E. Frajka-Williams, B. I. Moat, and D. A. Smeed, 2021: A dynamically based method for estimating the Atlantic meridional overturning circulation at 26°N from satellite altimetry. *Ocean Sci.*, **17**, 1321–1340, https://doi.org/10.5194/os-17-1321-2021.

Sauzède, R., H. C. Bittig, H. Claustre, O. Pasqueron de Fommervault, J.-P. Gattuso, L. Legendre, and K. S. Johnson, 2017: Estimates of water-column nutrient concentrations and carbonate system parameters in the global ocean: A novel approach based on neural networks. *Front. Mar. Sci.*, **4**, 128, https://doi.org/10.3389/fmars.2017.00128.

Schlesinger, M. E., and N. Ramankutty, 1994: An oscillation in the global climate system of period 65–70 years. *Nature*, **367**, 723–726, https://doi.org/10.1038/367723a0.

Schleussner, C. F., A. Levermann, and M. Meinshausen, 2014: Probabilistic projections of the Atlantic overturning. *Climatic Change*, **127**, 579–586, https://doi.org/10.1007/s10584-014-1265-2.

Schmidtko, S., K. J. Heywood, A. F. Thompson, and S. Aoki, 2014: Multidecadal warming of Antarctic waters. *Science*, **346**, 1227–1231, https://doi.org/10.1126/science.1256117.

—— , L. Stramma, and M. Visbeck, 2017: Decline in global oceanic oxygen content during the past five decades. *Nature*, **542**, 335–339, https://doi.org/10.1038/nature21399.

Schmitt, R. W., 1995: The ocean component of the global water cycle. *Rev. Geophys.*, **33**, 1395–1409, https://doi.org/10.1029/95RG00184.

Schoeberl, M. R., Y. Wang, R. Ueyama, G. Taha, E. Jensen, and W. Yu, 2022: Analysis and impact of the Hunga Tonga-Hunga Ha'apai stratospheric water vapor plume. *Geophys. Res. Lett.*, **49**, e2022GL100248, https://doi.org/10.1029/2022GL100248.

Sellitto, P., and Coauthors, 2022: The unexpected radiative impact of the Hunga Tonga eruption of 15th January 2022. *Nat. Commun. Earth Environ.*, **3**, 288, https://doi.org/10.1038/s43247-022-00618-z.

Sharp, J. D., A. J. Fassbender, B. R. Carter, G. C. Johnson, C. Schultz, and J. P. Dunne, 2022a. GOBAI-O2: A global gridded monthly dataset of ocean interior dissolved oxygen concentrations based on shipboard and autonomous observations (NCEI Accession 0259304), V2.0. NOAA National Centers for Environmental Information, accessed 23 March 2023, https://doi.org/10.25921/z72m-yz67.

—— , —— , —— , —— , —— , and —— , 2022b: GOBAI-O2: Temporally and spatially resolved fields of ocean interior dissolved oxygen over nearly two decades. *Earth Syst. Sci. Data Discuss.*, https://doi.org/10.5194/essd-2022-308.

Siegel, D. A., and Coauthors, 2013: Regional to global assessments of phytoplankton dynamics from the SeaWiFS mission. *Remote Sens. Environ.*, **135**, 77–91, https://doi.org/10.1016/j.rse.2013.03.025.

—— , T. DeVries, I. Cetinić, and K. M. Bisson, 2023: Quantifying the ocean's biological pump and its carbon cycle impacts on global scales. *Annu. Rev. Mar. Sci.*, **15**, 329–356, https://doi.org/10.1146/annurev-marine-040722-115226.

Skliris, N., R. Marsh, S. A. Josey, S. A. Good, C. Liu, and R. P. Allan, 2014: Salinity changes in the World Ocean since 1950 in relation to changing surface freshwater flux. *Climate Dyn.*, **43**, 709–736, https://doi.org/10.1007/s00382-014-2131-7.

—— , J. D. Zika, G. Nurser, S. A. Josey, and R. Marsh, 2016: Global water cycle amplifying at less than the Clausius-Clapeyron rate. *Sci. Rep.*, **6**, 38752, https://doi.org/10.1038/srep38752.

Stackhouse, P. W., D. P. Kratz, G. R. McGarragh, S. K. Gupta, and E. B. Geier, 2006: Fast Longwave and Shortwave Radiative Flux (FLASHFlux) products from CERES and MODIS measurements. *12th Conf. on Atmospheric Radiation*, Madison, WI, Amer. Meteor. Soc., P1.10, https://ams.confex.com/ams/Madison2006/techprogram/paper_113479.htm.

Sweet, W. V., J. Park, J. J. Marra, C. Zervas, and S. Gill, 2014: Sea-level rise and nuisance flood frequency changes around the United States. NOAA Tech. Rep. NOS CO-OPS 73, 66 pp., https://tidesandcurrents.noaa.gov/publications/NOAA_Technical_Report_NOS_COOPS_073.pdf.

Taha, G., R. Loughman, P. R. Colarco, T. Zhu, L. W. Thomason, and G. Jaross, 2022: Tracking the 2022 Hunga Tonga-Hunga Ha'apai aerosol cloud in the upper and middle stratosphere using space-based observations. *Geophys. Res. Lett.*, **49**, e2022GL100091, https://doi.org/10.1029/2022GL100091.

Talley, L. D., 2002: Salinity patterns in the ocean. *The Earth System: Physical and Chemical Dimensions of Global Environmental Change*, Vol. 1, *Encyclopedia of Global Environmental Change*, M. C. MacCracken and J. S. Perry, Eds., John Wiley and Sons, 629–640.

—— , and Coauthors, 2016: Changes in ocean heat, carbon content, and ventilation: A review of the first decade of GO-SHIP global repeat hydrography. *Annu. Rev. Mar. Sci.*, **8**, 185–215, https://doi.org/10.1146/annurev-marine-052915-100829.

Taschetto, A., C. C. Ummenhofer, M. F. Stuecker, D. Dommenget, K. Ashok, R. R. Rodrigues, and S.-W. Yeh, 2020: ENSO atmospheric teleconnections. *El Niño Southern Oscillation in a Changing Climate*, *Geophys. Monogr.*, Vol. 253, Amer. Geophys. Union, 309–335, https://doi.org/10.1002/9781119548164.ch14.

Trenberth, K. E., J. M. Caron, D. P. Stepaniak, and S. Worley, 2002: Evolution of El Niño Southern Oscillation and global atmospheric surface temperatures. *J. Geophys. Res.*, **107**, 4065, https://doi.org/10.1029/2000JD000298.

Vallès-Casanova, I., S.-K. Lee, G. R. Foltz, and J. L. Pelegri, 2020: On the spatiotemporal diversity of Atlantic Niño and associated rainfall variability over West Africa and South America. *Geophys. Res. Lett.*, **47**, e2020GL087108, https://doi.org/10.1029/2020GL087108.

van Sebille, E., M. O. Baringer, W. E. Johns, C. S. Meinen, L. M. Beal, M. F. de Jong, and H. M. Aken, 2011: Propagation pathways of classical Labrador Sea water from its source region to 26°N. *J. Geophys. Res.*, **116**, C12027, https://doi.org/10.1029/2011JC007171.

Vaquer-Sunyer, R., and C. M. Duarte, 2008: Thresholds of hypoxia for marine biodiversity. *Proc. Natl. Acad. Sci. USA*, **105**, 15 452–15 457, https://doi.org/10.1073/pnas.0803833105.

Volkov, D. L., S.-K. Lee, F. W. Landerer, and R. Lumpkin, 2017: Decade-long deep-ocean warming detected in the subtropical South Pacific. *Geophys. Res. Lett.*, **44**, 927–936, https://doi.org/10.1002/2016GL071661.

—— , R. Domingues, C. S. Meinen, R. Garcia, M. Baringer, G. Goni, and R. H. Smith, 2020: Inferring Florida Current volume transport from satellite altimetry. *J. Geophys. Res. Oceans*, **125**, e2020JC016763, https://doi.org/10.1029/2020JC016763.

—— , and Coauthors, 2022: Meridional overturning circulation and heat transport in the Atlantic Ocean [in "State of the Climate in 2021"]. *Bull. Amer. Meteor. Soc.*, **103** (8), S175–S178, https://doi.org/10.1175/BAMS-D-22-0072.1.

von Schuckmann, K., J.-B. Sallée, D. Chambers, P.-Y. Le Traon, C. Cabanes, F. Gaillard, S. Speich, and M. Hamon, 2014: Consistency of the current global ocean observing systems from an Argo perspective. *Ocean Sci.*, **10**, 547–557, https://doi.org/10.5194/os-10-547-2014.

Von Storch, H., and F. W. Zwiers, 1999: *Statistical Analysis in Climate Research*. Cambridge University Press, 484 pp.

Walsh, K. J. E., and Coauthors, 2016: Tropical cyclones and climate change. *Wiley Interdiscip. Rev.: Climate Change*, **7**, 65–89, https://doi.org/10.1002/wcc.371.

Wang, J., and B. Yang, 2017: Internal and external forcing of multidecadal Atlantic climate variability over the past 1,200 years. *Nat. Geosci.*, **10**, 512–517, https://doi.org/10.1038/ngeo2962.

Wanninkhof, R., 2014: Relationship between wind speed and gas exchange over the ocean revisited. *Limnol. Oceanogr.: Methods*, **12**, 351–362, https://doi.org/10.4319/lom.2014.12.351.

Werdell, P. J., and Coauthors, 2013: Generalized ocean color inversion model for retrieving marine inherent optical properties. *Appl. Opt.*, **52**, 2019–2037, https://doi.org/10.1364/AO.52.002019.

Westberry, T. K., P. Schultz, M. J. Behrenfeld, J. P. Dunne, M. R. Hiscock, S. Maritorena, J. L. Sarmiento, and D. A. Siegel, 2016: Annual cycles of phytoplankton biomass in the subarctic Atlantic and Pacific Ocean. *Global Biogeochem. Cycles*, **30**, 175–190, https://doi.org/10.1002/2015GB005276.

Wijffels, S., D. Roemmich, D. Monselesan, J. Church, and J. Gilson, 2016: Ocean temperatures chronicle the ongoing warming of Earth. *Nat. Climate Change*, **6**, 116–118, https://doi.org/10.1038/nclimate2924.

Williams, N. L., and Coauthors, 2016: Empirical algorithms to estimate water column pH in the Southern Ocean. *Geophys. Res. Lett.*, **43**, 3415–3422, https://doi.org/10.1002/2016GL068539.

Willis, J. K., 2010: Can in situ floats and satellite altimeters detect long-term changes in Atlantic Ocean overturning? *Geophys. Res. Lett.*, **37**, L06602, https://doi.org/10.1029/2010GL042372.

—— , D. Roemmich, and B. Cornuelle, 2004: Interannual variability in upper ocean heat content, temperature, and thermosteric expansion on global scales. *J. Geophys. Res.*, **109**, C12036, https://doi.org/10.1029/2003JC002260.

Winkler, L. W., 1888: Die Bestimmung des im Wasser gelösten Sauerstoffes. *Ber. Dtsch. Chem. Ges.*, **21**, 2843–2854, https://doi.org/10.1002/cber.188802102122.

Wolter, K., and M. S. Timlin, 1998: Measuring the strength of ENSO events: How does 1997/98 rank? *Weather*, **53**, 315–324, https://doi.org/10.1002/j.1477-8696.1998.tb06408.x.

Wood, M., and Coauthors, 2021: Ocean forcing drives glacier retreat in Greenland. *Sci. Adv.*, **7**, eaba7282, https://doi.org/10.1126/sciadv.aba7282.

Wüst, G., 1936: Oberflächensalzgehalt, Verdunstung und Niederschlag auf dem Weltmeere. *Länderkundliche Forschung: Festschrift zur Vollendung des sechzigsten Lebensjahres Norbert Krebs*, J. Engelhorns Nachfahren, 347–359.

Xie, P., and Coauthors, 2014: An in situ-satellite blended analysis of global sea surface salinity. *J. Geophys. Res. Oceans*, **119**, 6140–6160, https://doi.org/10.1002/2014JC010046.

Yang, H., and Coauthors, 2020: Poleward shift of the major ocean gyres detected in a warming climate. *Geophys. Res. Lett.*, **47**, e2019GL085868, https://doi.org/10.1029/2019GL085868.

Yu, L., 2011: A global relationship between the ocean water cycle and near-surface salinity. *J. Geophys. Res.*, **116**, C10025, https://doi.org/10.1029/2010JC006937.

Zebiak, S. E., 1993: Air–sea interaction in the equatorial Atlantic region. *J. Climate*, **6**, 1567–1586, https://doi.org/10.1175/1520-0442(1993)0062.0.CO;2.

Zhang, R., R. Sutton, G. Danabasoglu, Y.-O. Kwon, R. Marsh, S. G. Yeager, D. E. Amrhein, and C. M. Little, 2019: A review of the role of the Atlantic meridional overturning circulation in Atlantic multidecadal variability and associated climate impacts. *Rev. Geophys.*, **57**, 316–375, https://doi.org/10.1029/2019RG000644.

Zhu, Y., and Coauthors, 2022: Perturbations in stratospheric aerosol evolution due to the water-rich plume of the 2022 Hunga-Tonga eruption. *Nat. Commun. Earth Environ.*, **3**, 248, https://doi.org/10.1038/s43247-022-00580-w.

Zweng, M. M., and Coauthors, 2018: *Salinity*. Vol. 2, *World Ocean Atlas 2018*, NOAA Atlas NESDIS 82, 50 pp., https://data.nodc.noaa.gov/woa/WOA18/DOC/woa18_vol2.pdf.